Freely Configurable Holographic Trap Arrays for the Trapping of Single Atoms

Philip Osterholz

SIGILL: UNIVERSITAT: LUDOVIC: MAXIM:

Munich 2020

Frei Konfigurierbare Holographische Fallenmuster für das Fangen Einzelner Atome

Masterarbeit an der Fakultät für Physik
Ludwig-Maximilians-Universität München
Max-Planck-Institut für Quantenoptik

vorgelegt von

Philip Osterholz

München, den 20. Mai 2020

Meinem Opa, der mir die Wissenschaft nahebrachte.

Abstract

In this thesis, a laser system for the generation of many arbitrary positionable, tightly confining optical dipole traps for ^{39}K is implemented. The traps are generated using a liquid crystal spatial light modulator in the Fourier plane of an objective. The loading of single atoms into the generated trap array in a deterministic fashion is investigated. To overcome arising limitations in the apparatus a second setup for generating optical dipole traps using an acousto-optic deflector is planned and characterized. This will complement the first setup in the future.

Contents

CHAPTER 1

Introduction

In the past decades, experiments outperformed the vaguest dreams of the early pioneers of quantum mechanics [1] and answered a variety of fundamental questions. Advances in laser technology and detection techniques lead to the proof of violation of Bell's inequality [2], the demonstration of the quantum statistical nature of light [3], the first implementation of quantum state teleportation [4] and many more astonishing breakthroughs. In 1995, first Eric Cornell and Carl Wieman and later that year Wolfgang Ketterle produced the first Bose-Einstein condensates by applying laser cooling techniques to a cloud of atoms[5, 6]. This milestone triggered an impressive development in the field of cold and ultracold quantum gases. The rapid progress in isolating, controlling and observing these fragile quantum systems soon allowed for studies of quantum phenomena inherent to solid-state systems with unprecedented parameter control, for example, the quantum phase transition from a superfluid to a Mott insulator [7]. The enthusiasm for driving this progression was not limited to atomic systems but spread over a magnitude of fundamentally different systems. Techniques to manipulate and interrogate quantum many-body systems on a single particle level on a whole zoo of platforms [8] are available today and allow to study systems including exotic quantum matter [9], out of equilibrium dynamics [10], gauge field models [11, 12] and many more.

All these groundbreaking works can be taken as examples of quantum simulators. The concept to simulate a real quantum system with the aid of another better-controlled quantum system was brought up by Richard Feynman in 1982 as an answer to the incompatibility of the exponential growth of the Hilbert space with the size of a quantum system and the effort to understand the details of large quantum systems [13]. While a classical computer always suffers from this exponential scaling, a quantum simulator can be designed such that it only exhibits a polynomial resource scaling with the system size [14]. Two types of quantum simulators are to be distinguished. The first uses a universal set of quantum gates which are well-defined, unitary operations applied to a subsystem of the simulator's inherent quantum system. By assembling the execution of multiple of these gates after one another any quantum algorithm can be implemented. Paralleled to the working principle of classical digital computers, this is called a digital quantum simulator. A different approach is pursued by the so-called analog quantum simulation. The dynamics of the quantum system, hosted by the simulator, is governed by an intrinsic time evolution with tunable parameters. By a suitable choice of observables and parameters the quantum simulator can emulate a system of interest. Both approaches require an efficient mapping between a Hilbert space of the system or problem in question and the quantum system of the simulator

$$\mathcal{H}_{real} \supset \mathcal{H} \to \mathcal{H}_{sim}$$

entailing an adequate mapping between the Hamiltonians of both

$$H_{real} \to H_{sim}.$$

In recent years the concept of combining a quantum simulator with a classical computer attracted a lot of attention as this allows leveraging the potential of near term quantum simulators. An example for such an approach are Quantum Approximate Optimization Algorithms (QAOAs) [15, 16].

Rydberg atoms, with there exaggerating and well tunable interaction properties recently emerged as a promising candidate for the realization of digital [17] and analog quantum simulators [18]. However, the lifetime of the Rydberg states being several microseconds limited experiments to either very few atoms or the so-called frozen gas regime where all the relevant dynamics occur on a much longer time scale than the coherence time of the system [19]. Pulsed Rydberg excitation [20] or off-resonant coupling to Rydberg states [21, 22] , the so-called "Rydberg dressing", had proven to be promising approaches to overcome this limitation. The later is grounded on the coupling of the ground state to a Rydberg state to yield a new eigenstate, inheriting the long lifetime of the ground state and the interaction properties of the Rydberg state to an extend adjustable by the coupling parameters [23]. Extending this idea to more complex couplings involving multiple Rydberg states holds the great promise for enriching the toolbox of superexchange interactions and paving the way to understand new exotic forms of matter [24].

The long-range interaction properties of the Rydberg atoms allow for novel approaches to prepare many body systems. Much pioneering and groundbreaking work on Rydberg physics was done by trapping atoms in large optical dipole traps or optical lattices [25] and coupling the atoms to the Rydberg manifold by means of global light fields. It had also been demonstrated that it is possible to excite atoms in a magneto-optical trap to Rydberg states at well-defined and programmable positions [26]. Another approach, which attracted a lot of attention in recent years, is the trapping of individual atoms in a multitude of close, highly confining optical dipole traps, known as optical tweezers, arranged in arbitrary one-, two- and three-dimensional geometries [27–29]. Combined with Rydberg mediated interactions it had been possible for example to realize Greenberger-Horne-Zeilinger states with up to 20 qubits [30] , demonstrate spin-orbit coupling and an emerging Peierls phase [31], implement symmetry protected topological phases [32] and many more.

This thesis is concerned with the experimental and algorithmic implementation and preparation of atoms in arbitrary arranged optical tweezers in two dimensions. This involves the integration of a liquid crystal spatial light modulator in an existing experimental setup and the in-situ characterization of the generated traps. To increase the versatility and usability of the apparatus an extension based on an acousto-optic deflector to generate movable traps is considered.

Outline

Chapter 2 presents all the foundations this thesis project is built upon. It introduces the theoretical background for confining the motion of atoms to a small region in space by using their dipole moments and uses the so found relations to estimate experimental parameters. It also gives an overview of the experimental techniques implemented prior to the described project and essential for its success. Chapter 3 introduces the spatial light modulator based setup for generating the trap arrays. After introducing the working principle of the device the integration in the setup is presented. A detailed picture of the emerging wavefront reconstruction problem for the case of multiple diffraction-limited spots is provided and evolved to its solution used in the context of this thesis. Thereafter, the procedure to trap individual atoms is discussed and experimentally obtained results are presented. Based on this, multiple in-situ measurements to characterize the traps are presented. In Chapter 4 the emerging problem of the limited probability to load an atom in each dipole trap is discussed and a solution to this is experimentally investigated. Chapter 5 introduces the planned extension of the setup with the use of an acousto-optic deflector opening new experimental prospects, which will also be discussed. Finally, Chapter 6 contains a summary of the obtained results and achievements and an outlook on what is soon to come to improve and extend the experiment.

CHAPTER 2

Optical Trapping and Cooling of Potassium

The majority of manipulation of internal and motional degrees of freedom of the Potassium-39 atoms used in this project is done with lasers, which provide coherent light at a single frequency. In this chapter, the theoretical foundation will be laid to understand the subsequent chapters. First, a classical model will be discussed, capturing all the features of atom-light interactions essential for optical dipole traps. Then, a quantum perturbative approach will be used to treat multi-level atoms analogous to the classical model. The discussion of the relevant atom-light interactions will be concluded by a section on heating effects in the traps. After this general treatment, the optical properties of Potassium-39 will be introduced and subsequently, the characteristics of this atomic species at the wavelengths considered for trapping will be listed. The chapter is concluded by a brief listing of the required tools to go from a block of Potassium-39 to single atoms trapped in optical tweezers.

2.1 Optical Dipole Potentials in a Classical Model

The center of mass motion of an atom and its internal level structure can be coupled by an electromagnetic field. How this can be used to confine the motion of an atom to a small region in space will be discussed here. Especially coherent electromagnetic waves at optical wavelengths produced by lasers are appealing to experimentalists, as they allow for precise control over the electromagnetic field in a small spacial region with the emitter being potentially meters away. This opens a large and flexible toolbox for the manipulation of atomic ensembles. The valence electrons of an atom, which are especially weak bound to the core, are sensitive to the environment of the atom. They are the predominant contributor in chemical reactions and they also react to optical fields which leave the rest of the electrons undisturbed. In the following, a closer look will be taken on the coupling of atomic motion to the internal structure induced by the presence of far-detuned monochromatic laser light in a classical model. A variety of phenomena in the weak excitation limit of atom-light interactions are well described by a classical model of the atom interacting with classical light. The model used is known as the Lorentz model [33]. It describes the motion of an electron bound to a core by a classical damped harmonic oscillator. The equation of motion of the electron is

$$m_e\ddot{\vec{x}} + m_e\gamma\dot{\vec{x}} + m_e\omega_0^2\vec{x} = -\hat{\epsilon}eE_0e^{-i\omega t}$$

with the light field $E(t) = \hat{\epsilon}E_0e^{-i\omega t}$ introduced as the driving of the oscillator. Note that the linearity of the differential equation was used to split it into two equivalent equations valid in the complex plane. This allows for the complex laser field description used. The equation of motion is easily solved for example by the use of a Laplace transformation [34]. This yields

$$\vec{x}(t) = \frac{eE(t)/m}{\omega^2 - \omega_0^2 - i\gamma\omega}.$$

The electric dipole moment of the system is given as $\vec{d} = -e\vec{x}(t)$, and from the definition of the polarizability $\vec{d} = \alpha(\omega)E(t)$ one finds that

$$\alpha(\omega) = \frac{e^2/m}{\omega_0^2 - \omega^2 - i\gamma\omega}$$

With this it is easy to derive the adiabatic dipole potential. The interaction energy of a dipole with an electric field is given as [35]

$$V_{dipole} = -\frac{1}{2}\langle \vec{d} \cdot \vec{E} \rangle_t$$

where $\langle \cdot \rangle_t$ denotes a time averaging chosen such that terms oscillating fast compared to the frequency of the damped harmonic oscillator are dropped. Inserting the expression of the polarizability yields

$$V_{dipole} = -\frac{1}{2\epsilon_0 c}\Re(\alpha)I$$

where $I = 2\epsilon_0 c|E_0|^2$ is the intensity of the light and $\Re(\cdot)$ denotes the real part. ϵ_0 is the vacuum permittivity. A similar expression can be found for the scattering rate of photons. The scattered photons can be thought of as quanta of the power absorbed by the damped harmonic oscillator $P_{abs} = \langle \dot{\vec{d}} \cdot \vec{E} \rangle_t$

$$\Gamma_{sc} = \frac{P_{abs}}{\hbar\omega} = \frac{1}{\hbar\epsilon_0 c}\Im(\alpha)I.$$

Here $\Im(\cdot)$ is the imaginary part. Putting all of this together one finds the following explicit expressions for the dipole potential and the scattering rate

$$V_{dipole}(r) = -\frac{3\pi c^2}{2\omega_0^3}\left(\frac{\Gamma}{\omega_0 - \omega} + \frac{\Gamma}{\omega_0 + \omega}\right) I(r) \tag{2.1}$$

$$\Gamma_{sc}(r) = \frac{3\pi c^2}{2\hbar\omega_0^3}\frac{\omega^3}{\omega_0^3}\left(\frac{\Gamma}{\omega_0 - \omega} + \frac{\Gamma}{\omega_0 + \omega}\right)^2 I(r) \tag{2.2}$$

where the light intensity was now made position dependent. Note that here the decay rate was assumed to be dominated by the optical frequency terms. From comparing the results to the weak field limit of the optical Bloch-equations of a two level system one finds that $\gamma = (\omega/\omega_0)^2\Gamma$, with Γ the spontaneous decay rate of the transition.

From the Weisskopf-Wigner theory [36] the spontaneous decay rate can be related to the dipole matrix element $\langle e|\,\hat{d}\,|g\rangle$of the transition by

$$\Gamma = \frac{\omega_0^3}{3\pi\epsilon_0\hbar c^3}|\,\langle e|\,\hat{d}\,|g\rangle\,|^2.$$

The first term in the bracket of Equation 2.1 and Equation 2.2 gives rise to the well known AC-Stark shift and is typically the dominating factor. The second term is a so-called counter-rotating term. While this is typically neglected in the rotating wave approximation it gives rise to the Bloch-Siegert shift in strong fields tuned very far off-resonant. For the wavelength 1064 nm, which is used in all experiments related to this thesis, the ratio of Bloch-Siegert shift to AC-Stark shift is ≈ 0.16. Therefore, all the light shifts and scattering rates specified include both contributions.

2.2 Far Detuned Optical Dipole Potentials

To treat a multi-level atom quantum mechanically in a radiation field far off-resonant to any transition a perturbative analysis is sufficient and captures the relevant effects. To first order the eigenenergies E_i of the unperturbed atomic Hamiltonian are shifted by

$$\Delta E_i = \sum_{j\neq i}\frac{\langle i|\,\mathcal{H}_{int}\,|j\rangle\,\langle j|\,\mathcal{H}_{int}\,|i\rangle}{\hbar\delta_{ij}} + \sum_{j\neq i}\frac{\langle i|\,\mathcal{H}_{int}\,|j\rangle\,\langle j|\,\mathcal{H}_{int}\,|i\rangle}{-\hbar(\omega_{ij}+\omega)} \tag{2.3}$$

where $\omega_{ij} = (E_i - E_j)/\hbar$ is the angular frequency of the transition $i \to j$ and $\delta_{ij} = \omega_{ij} - \omega$ is the detuning of the angular light frequency ω to it. For atom light interactions the interaction Hamiltonian is given as $H_{int} = -\hat{d}\cdot\mathbf{E}$ with $\hat{d}$ the electric dipole operator and $\mathbf{E}(\mathbf{r},\mathbf{t}) = \mathbf{e}\tilde{E}(r)exp(-i\omega t) + c.c.$ the monochromatic electric field. $\tilde{E}(r)$ denotes the amplitude and $\mathbf{e}$ the unit polarization vector of the field. The second term in Equation 2.3 is again often hidden in the rotating wave approximation. However, in this approach it is intuitive to include it. Both terms describe the interference via an energetically off-shell intermediate state.

It is worth noting that this perturbative treatment breaks down when $\mathbf{e}$ does not represent a pure linear or circular polarization and the considered atoms have degenerate ground states. A mixture of polarizations might lead to Raman transitions in the magnetic substructure of the level scheme. This can be accounted for by introducing an effective magnetic field [37] . In the present experimental apparatus this effect can have treacherous consequences, because even if the light of the dipole traps is linear polarized before being focussed, the focussing with objectives of a $NA = 0.6$ is on the edge of overstraining the paraxial approximation and position dependent admixtures of circular polarized light in the diffraction limited spot is expected. This gives raise to an effective magnetic field gradient as discussed in [38, 39].

To apply formula (2.3) the dipole matrix elements $d_{ij} = \langle i|\,\hat{d}\,|j\rangle$ need to be known. For the most transitions between low lying states they can be deduced from very precisely measured spectroscopical quantities using again the result of the Wiegner-Weisskopf theory

$$A_{i\leftarrow j} = \frac{\omega_0^3}{3\pi\epsilon_0\hbar c^3}|d_{ij}|^2. \tag{2.4}$$

Here $A_{i\leftarrow j}$ denotes the "Einstein A-coefficient" of the $i \leftarrow j$ dipole transition. A collection of those coefficients can be found in the NIST data base [40]. They were used for all calculations carried out here. For rather exotic transitions, for example in the Rydberg manifold, no experimental data is available and one has to rely on sophisticated numerical algorithms [41].
By inserting Equation 2.4 in Equation 2.3 and interpreting the light shift as a position dependent adiabatic potential for an atom in state i we find

$$U_i(r) = \frac{3\pi c^2}{2\omega_0^3} I(r) \cdot \left(\sum_{i\neq j} \frac{A_{i\leftarrow j}}{\delta_{ij}} - \sum_{i\neq j} \frac{A_{i\leftarrow j}}{\omega_{ij}+\omega} \right)$$

where $I(r) = 2\epsilon_0 c|\mathbf{E}(r)|^2$ is the position dependent intensity. Usually the trapped alkali atoms can be assumed to rest in the ground state and we can calculate some characteristics of the trapping potential for that case. Assuming a Gaussian beam of the form

$$I(r,z) = I_0 \frac{1}{1+(\frac{z}{z_R})^2} \exp\left(-\frac{2r^2}{w_0^2(1+(\frac{z}{z_R})^2)} \right)$$

with I_0 the peak intensity, w_0 the beam waist and $z_R = \pi w_0^2/\lambda$ the Rayleigh length [42]. The profile is given in polar coordinates. The trap depth can easily be identified to be

$$U_{min} = \frac{3\pi c^2}{2\omega_0^3} I_0 \left(\sum_{i\neq j} \frac{A_{i\leftarrow j}}{\delta_{ij}} - \sum_{i\neq j} \frac{A_{i\leftarrow j}}{\omega_{ij}+\omega} \right).$$

A Taylor expansion around the center of the Gaussian beam to second order yields a harmonic trapping potential with a radial trap frequency of

$$\omega_r = \sqrt{\frac{4U_{min}}{m w_0^2}}$$

and a longitudinal trapping frequency of

$$\omega_z = \omega_r \frac{w_0}{z_R\sqrt{2}}. \tag{2.5}$$

2.3 Off-resonant Heating

The effect of heating due to the trap light is another aspect of vital importance. In alkali atoms only one valence electron is present, which has to perform spontaneous decays in all single atom cooling processes to remove entropy from the system [43].

At the same time, in most schemes considered for exploring quantum many body dynamics the quantum information is stored in the electronic state of the atom using the same electron. Therefore simultaneous cooling and performing a quantum simulation experiment is undesirable as the cooling leads to a rapid loss of coherence in the system. This means any heating process needs to be avoided.

There are two major heating processes to be considered in far-detuned optical traps. The first one is known as parametric heating. When the geometry of the trap is prone to noise the frequency component of the noise resonant with a multiple of the trap frequency can be absorbed and emitted from the spatial wave function of the atom in the trap. Therefore this can lead to heating. This heating does only have a small effect on the quantum state of the atom by slightly wiggling the hyperfine splitting of the ground state [44], but it can lead to significant thermal broadening of lines or, in the worst, case to a loss of the atom from the trap. A rigorous treatment of this can be found in [45, 46].

The second relevant heating effect is the spontaneous scattering of photons from the trapping light. In the far-detuned regime this process reduces to a two photon process with one photon coming from the trapping light and the other one a vacuum photon, which triggers the emission.

This two cases are to be distinguished. In the first case, the atom ends up in the same state as prior to the scattering. This elastic collision between photon and atom is the well-known Rayleigh-scattering. In the second case, the atom changes its hyperfine ground state. This makes the scattering event inelastic. This process, known as Raman-scattering, can lead to decoherence as well but is reduced by a factor $\sim 1/\delta^2$ with the δ the detuning of the trapping light field. Typically this decoherence process is much slower then the one due to noise in the trap geometry.

Due to the anisotropic nature of the photons coming from the light field the heating is also anisotropic but the different axis of the trap are typically coupled with a coupling constant exceeding the usually very small scattering rate. Therefore one can consider the trap to be thermalized along all axis in this treatment. The overall heating power can then be written as

$$P_{heat} = 2E_{rec}\Gamma_{sc} = 2k_B T_{rec}\Gamma_{sc}$$

where Γ_{sc} denotes the off resonant scattering rate and $E_{rec} = k_B T_{rec}$ is the recoil energy and temperature respectively for the absorption of a single photon. The scattering rate is given by

$$\Gamma_{sc} = \frac{3\pi c^2}{2\omega_0^3} I(r) \sum_{j\neq g} \left(\frac{A_{g\leftarrow j}}{\delta_{ij}} \right)^2 .$$

This heating process depends on the positional distribution of the atoms in the trap, as they experience different intensities at different positions. In the following the scattering rates are always calculated using the peak intensity of the trap.

2.4 Optical Properties of Potassium-39

Property	symbol	value
Frequency	ν	389.286058716(62) THz
Wavelength	λ	770.108385049(123) nm
Wavenumber	$k/2\pi$	12985.1851928(21)cm^{-1}
Lifetime	τ	26.72(5) ns
Natural linewidth	$\Gamma/2\pi$	5.956(11) MHz
Recoil velocity	v_{rec}	1.329825973(7) cm/s
Recoil temperature	T_{rec}	0.41436702 μK
Doppler temperature	T_D	145 μK

Table 2.1 – Optical properties of the D1 line [47]

Property	symbol	value
Frequency	ν	391.01617003(12) THz
Wavelength	λ	766.700921822(24) nm
Wavenumber	$k/2\pi$	13042.8954964(4)cm^{-1}
Lifetime	τ	26.37(5) ns
Natural linewidth	$\Gamma/2\pi$	6.035(11) MHz
Recoil velocity	v_{rec}	1.335736144(7) cm/s
Recoil temperature	T_{rec}	0.41805837 μK
Doppler temperature	T_D	145 μK
Saturation intensity	I_s	1.75 mW/cm^2

Table 2.2 – Optical properties of the D2 line [47]

As all alkali atoms, Potassium-39 only has one valence electron, which is the only one participating in atom light interactions in the optical domain. The potential it sees is a coulomb like potential from the nucleus and the core electrons. While for the lower energy levels the valence electrons wave function has a significant overlap with the wave functions of the core electrons and the nucleus, for Rydberg states the overlap becomes more and more negligible with increasing principal quantum number n. In the later case the level structure is well captured by an empirical state dependent quantum defect δ_{nlj} and a modified Rydberg constant Ry^* which are introduced in the well known Rydberg formula for the hydrogen problem [48]

$$E_{nlj} = E_\infty - \frac{Ry^*}{(n - \delta_{nlj})^2}$$

where E_∞ is the ionization energy of Potassium-39. For lower lying states the overlap of the electronic wave functions prohibits such a simple treatment and the level structure is strongly modified compared to that of a hydrogen like atom. The for cooling and trapping most relevant lines in all alkali atoms are the lowest lying optical transitions in the fine structure spectrum, called D lines. The D1 line is the transition from the $4^2S_{1/2}$ to the $4^2P_{1/2}$ state and the D2 line from the $4^2S_{1/2}$ to the $4^2P_{3/2}$ state. The

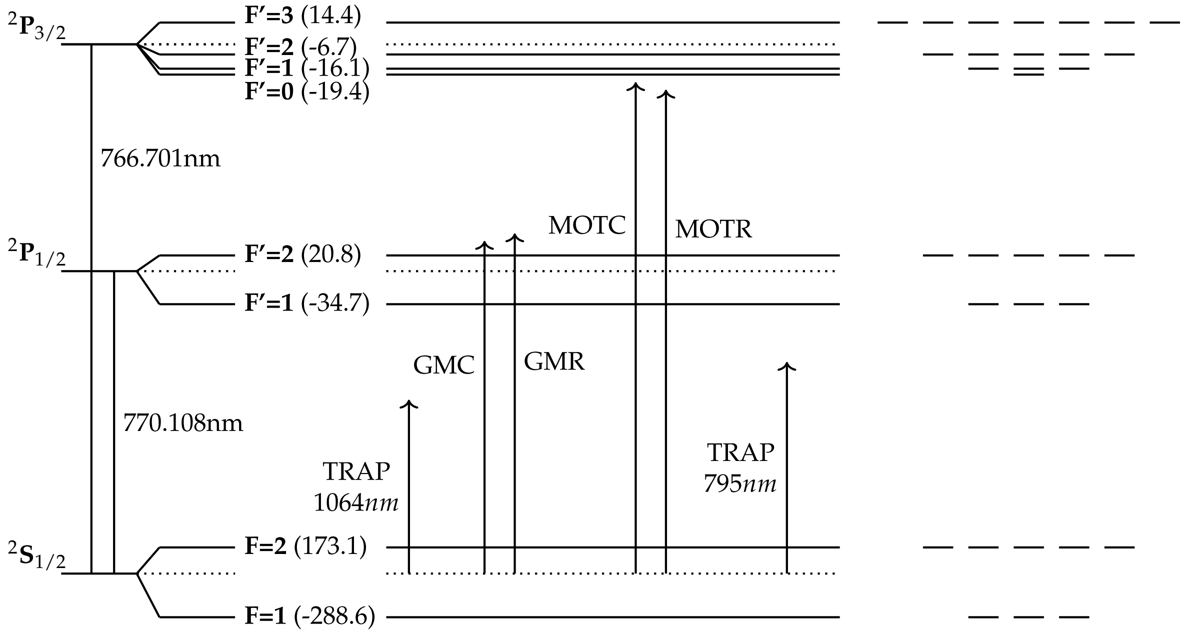

Figure 2.1 – D-line level structure of Potassium-39 Optical transitions from D1 and D2 line. On the left the fine structure and hyper fine structure is shown. The hyper fine structure is given in units of MHz. In the middle of the figure the lasers relevant for the projects related to this thesis are shown. On the right the full magnetic substructure at zero field is shown.

properties of the D1 and D2 line of Potassium-39 are listed in Table 2.1 and Table 2.2 respectively. Figure 2.1 shows the level structure of the D lines together with the lasers used in this project. The ground state is the $4^2S_{1/2}$ state. The fine structure coupling of the spin **S** and angular momentum **L** of the valence electron lifts the degeneracy of the $4^2P_{1/2}$ and $4^2P_{3/2}$. The total electronic angular momentum is given as

$$\mathbf{J} = \mathbf{L} + \mathbf{S}.$$

As in all alkali atoms the nuclear spin **I**, with a magnitude of $I = 3/2$ for Potassium-39, couples to the electonic angular momentum **J**.

$$\mathbf{F} = \mathbf{J} + \mathbf{I}$$

This lifts the degeneracy between levels with different F quantum numbers and results in the hyper fine structure. Especially important in the presented experimental apparatus is the hyper fine splitting in the $4^2S_{1/2}$ ground state. It is split in two hyper fine states individually addressable with lasers and particularly long-lived, which makes it well suited to model a spin–1/2 degree of freedom.

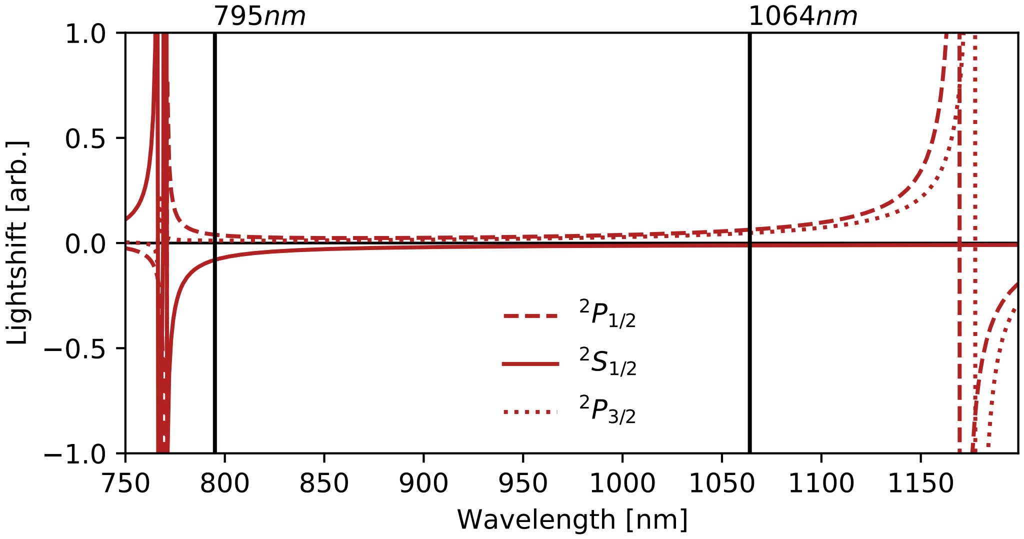

Figure 2.2 – D-line fine structure light shifts. The light shifts for linear polarized light in arbitrary linear units are shown for the three lowest fine structure states for different wavelength. The horizontal line marks the zero lightshift. The vertical lines indicate the wavelengths used or planned to be used in the experiment for creating tightly confining optical dipole traps for single atoms.

2.5 Calculated Trap Properties for the Experimental Setup

In this section a closer look will be taken upon the wavelength used for creating the tightly confining optical dipole traps in the experiment. As argued before most of the optical manipulation is done on the D1 and D2 line. Besides the shift of the fine structure ground state $4^2S_{1/2}$, which determines the trapping potential, the shifts of the $4^2P_{1/2}$ and $4^2P_{3/2}$ are therefore of particular importance. In Figure 2.2 the light shifts for those states for different wavelengths are shown. The black lines indicate the experimentally considered wavelengths.

The main work done in the context of this thesis uses 1064 nm light, which is detuned from the D1-line by $\Delta_{D1}(1064\,\text{nm}) = 107.5\,\text{THz}$ and from the D2-line by $\Delta_{D2}(1064\,\text{nm}) = 109.3\,\text{THz}$. The ground state is shifted by $\delta_{gs}(1064\,\text{nm}) = -17.5\,\text{MHz}\,\mu\text{m}^2\,\text{mW}^{-1}$, while the D1 and D2 lines are shifted by $\delta_{D1}(1064\,\text{nm}) = -5.66 \times \delta_{gs}(1064\,\text{nm})$ and $\delta_{D2}(1064\,\text{nm}) \approx 5 \times \delta_{gs}(1064\,\text{nm})$ respectively for linear light polarization. While different light shifts in the m_F-states are negligible in the ground state they are of the order of $\delta_{gs}(1064\,\text{nm})$ for the excited state. The ground state scattering rate is calculated to be $\Gamma_{gs}(1064\,\text{nm}) = 5 \cdot 10^{-8} \times \delta_{gs}(1064\,\text{nm})$ and typically on the order of 1 Hz .

In a second tweezers setup a wavelength of 795 nm and again linear polarization is considered. The light is red-detuned from the D1-line by $\Delta_{D1}(795\,\text{nm}) = 12.2\,\text{THz}$ and from the D2-line by $\Delta_{D2}(795\,\text{nm}) = 13.9\,\text{THz}$. The ground state is shifted by $\delta_{gs}(795\,\text{nm}) = -125.4\,\text{MHz}\,\mu\text{m}^2\,\text{mW}^{-1}$. The D1 and D2 lines are shifted by $\delta_{D1}(795\,\text{nm}) = -0.5 \times \delta_{gs}(795\,\text{nm})$ and $\delta_{D2}(795\,\text{nm}) \approx -0.5 \times \delta_{gs}(795\,\text{nm})$. The ground state scattering rate is $\Gamma_{gs}(795\,\mathrm{nm}) = 4.5 \cdot 10^{-7} \times \delta_{gs}(795\,\mathrm{nm})$ and therefore by about a factor 10 higher then for the same trap depth at 1064 nm.

2.6 Experimental Apparatus

This section provides an overview of the experimental setup to evaporate atoms from solid chunks of Potassium-39, trap them in ultra high vacuum, and cool them sufficiently such that they can be trapped in the dipole trap arrays, which are the main subject of this thesis. An in-depth discussion on the setup can be found in [49–51].

- **The atomic oven:** To provide the experiment with Potassium-39 atoms an oven is used. It heats a block of Potassium up to about 80 °C to slowly evaporate it. The evaporated atoms are then collimated by a nozzle of 3 mm aperture. A cold-finger is used to decrease the vapor pressure A differential pumping stage helps to decouple the vacuum in the experimental chamber from the one of the oven.
- **Zeeman slower:** The still hot and fast moving atoms need to be slowed down to capture them in the experimental chamber. This is achieved using a spin-flip Zeeman slower, which consists of a tube where the atomic beam travels through. Around this tube a coil with a position dependent winding number is wrapped. The winding number is chosen such that the traversing atoms are always in resonance with a laser beam on the D2-line shown through the tube from the side opposing the oven. With that the atoms see a friction force which slows them down below the capture velocity of the subsequent MOT.
- **Magneto Optical Trap:** To capture and further cool the atoms leaving the Zeeman slower a magneto optical trap (MOT) is used. A magnetic quadrupole field is created by two coils in anti-Helmholtz configuration. This field shifts the $m_f \neq 0$ states of a hyper fine level in the $^2P_{3/2}$ manifold such that they get closer to resonance to red detuned counter propagating circular polarized laser beams on the D2-line. In doing so they experience a conservative restoring force and a friction force towards the zero field region. This confines the atoms and cools them to the Doppler limit of that transition.
- **Gray Molasses:** Potassium-39 suffers from a narrow hyperfine structure in the D2 excited state wich prevents efficient sub-Doppler cooling by using light, far red detuned from a cycling transition, on this line. However, a different scheme called gray molasses can be realized on the D1 line. It exploits the presence of a dark state, which is motionally coupled to bright states. This means an atom which moves transitions to a bright state, while a still standing atom remains in the dark state. With a σ^+-σ^- configuration of blue detuned counter propagating beams a landscape of potential hills for the bright state is created. A moving atom in the dark state will be motionally transferred into a bright state and before it is pumped back into the dark state it looses kinetic energy by climbing a hill. This cools the atomic cloud from the Doppler limited temperature of the MOT to the recoil limit.

- **Red Molasses:** Although not capable of efficiently cooling the atomic sample from the Doppler to the recoil temperature, a red molasses keeps the atoms in place and cools them enough such that they get trapped in the tightly confined optical dipole traps, which are conservative in nature. Another advantage of the red molasses is its brightness. While atoms in the light field of a gray molasses barely scatter photons, the atoms cooled by a red molasses fluoresce much more light. This allows to image the atoms and maintain cooling at the same time.

With these tools the stage is prepared for the optical tweezers arrays, discussed in the next chapter.

CHAPTER 3

Large Arrays of Optical Dipole Traps

In order to study many body physics with individual atoms in optical dipole traps a large number of tightly focused beams needs to be realized. As it is experimentally undesirable to have an individual laser for each trap, schemes had been implemented over the last years which produce tens to hundreds of traps out of a single Gaussian beam. With tools ranging over micro lens arrays [52] and acousto-optic deflectors (AOD)[53] to digital mirror devices [54] and spatial light modulators (SLM)[55] several experiments succeeded in producing arbitrarily arranged optical tweezers for atoms.

In this chapter the use of a liquid crystal spatial light modulator is described to manipulate the wave front of a Gaussian beam. When the right manipulation is applied, the beam produces every desirable periodic and non-periodic geometry of traps when it is focused, only constrained by the number of traps and the minimal trap spacing. This high flexibility in realizable geometries distinguishes the use of a spacial light modulator from other approaches. In the following first the working principle of the used SLM as well as the experimental setup for exposing the atoms to the created optical potentials will be introduced. Then a naive approach to deduce the shape of the wave front leading to a given tweezers configuration will be discussed, followed by the introduction of the implemented Gerchberg-Saxton based phase retrieval algorithm to account for inaccuracies in the naive approach. Subsequently a typical experimental sequence to load atoms in the produced array will be described and the results of an in-situ trap characterisation will be discussed. Thereafter the observation of an effect similar to the well-known Talbot effect will be presented. The chapter will be concluded by a discussion on the current limitations and an outlook on how the setup can be improved.

3.1 Liquid Crystal Spatial Light Modulator

SLMs have seen a wide range of applications in the past. They have been used, for instance, in femtosecond pulse shaping [56], trapping of polarizable particles [57] or generation of angular momentum states of light [58]. Furthermore they led to advances in different microscopic schemes [59] and found applications in astronomy [60]. The possibility to produce taylored intensity patterns also attracted attention in the quantum gas community as a tool to generate exotic trap potentials [61, 62].

In order to produce arbitrary shaped arrays of tightly confining optical dipole potentials to trap single atoms, a liquid crystal SLM (LC-SLM) was used in this project. The high light utilization, the ability to realize any geometry and the possibility to

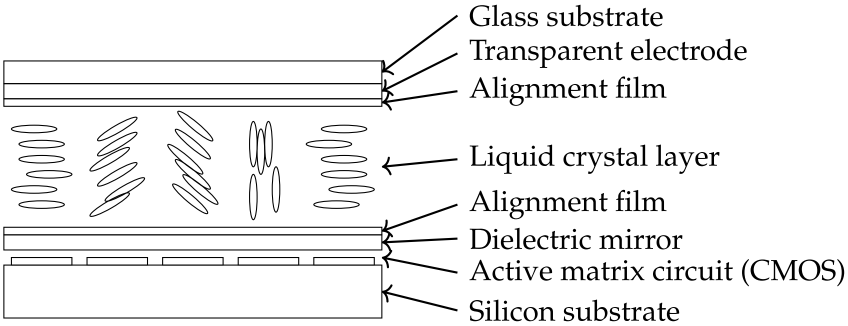

Figure 3.1 – Schematic diagram of the liquid crystal spatial light modulator chip. The orientation of the liquid crystal is controlled by applying a spacial varying electric field across it. This is generated using a matrix of electrodes beneath it, where each can be addressed individually, and a transparent electrode above it. The refractive index for light polarized perpendicular to the liquid crystals axis depends on this orientation. When light passes through the liquid crystal it travels a position dependent optical path length, allowing for arbitrary modifications of the wave front.

compensate for aberrations and optical imperfections makes this device well suited for our application. Here a water cooled Hamamatsu X10468-3 was used, due to its outstanding precision in the applied phase and low noise characteristics [63] and the ability to handle several Watts of light power. The architecture of the chip is illustrated in Figure 3.1. It consists of multiple layers [64]. These allow to locally modify a liquid crystal for taylored changes on the shape of an incident wave front. The first layer is formed by a glass substrate followed by a transparent electrode which serves the purpose of applying electric fields. Below that a liquid crystal is sandwiched between two alignment films, which ensure its proper orientation. In the present device the liquid crystal is oriented such that phase modulation is only possible for linear polarized light oriented in parallel to it. Other polarization components are unaffected. Beneath that the light is reflected by a dielectric mirror. The last layer is formed by a silicon substrate which has an active pixel matrix on its top consisting of 792×600 tiny electrodes each having a size of $20\,\mu\text{m} \times 20\,\mu\text{m}$, referred to as pixels. A CMOS based circuit structure is buried underneath them. With the CMOS structure an individual voltage level can be applied to each pixel. The electric field which builds up between the pixel electrode and the common transparent electrode modifies the orientation of the liquid crystal and therefore the refractive index at that position on the chip. With that the incident light travels an optical path through the liquid crystal with a position dependent length. Consequently the wave front is modified by an position dependent phase shift while the intensity distribution is maintained. Therefore such a SLM type is also referred to as a phase only SLM. The local phase can be modified by the full range of 2π with a 8 bit discretization. The interface to the SLM is done by a controller box from the manufacturer, which in turns accepts a gray scale picture over a DVI interface. The most important characteristics of the used SLM are summarized in table 3.1.

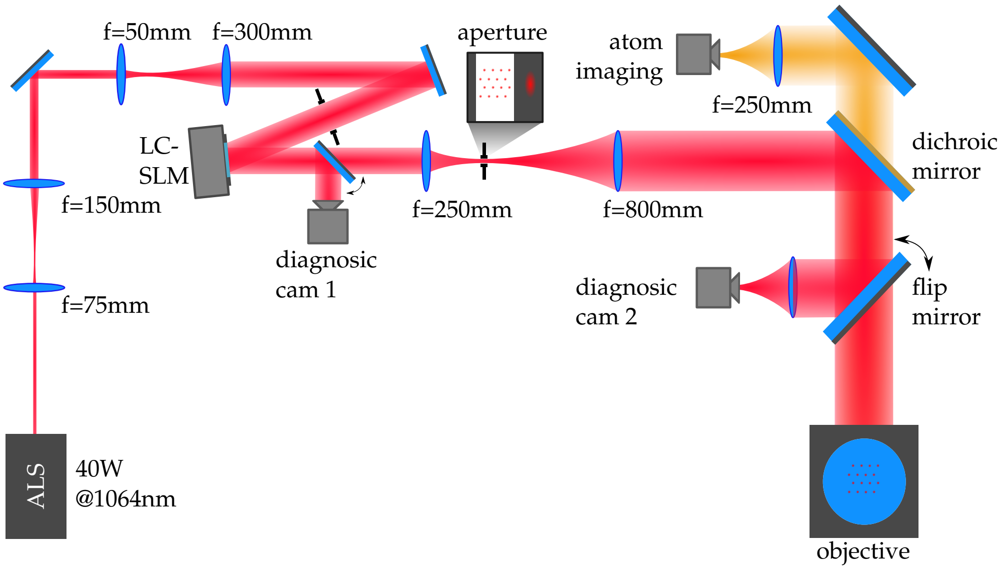

Figure 3.2 – Setup for the creation of trap arrays. For generating arbitrary arranged trap arrays we use a phase only LC-SLM, which is placed in the imaged Fourier plane of the objective. Before this setup the laser is intensity stabilized and switched using an AOM. The beam is magnified, to match the chip size of the SLM, to a $1/e^2$-diameter of $12mm$ and afterwards expanded to fit the aperture of the objective of $40mm$. The diagram is not to scale

Parameter	Value
Resolution	792×600
Pixel pitch	$20\mu m$
Effective area	$16mm \times 12mm$
Phase levels	256 (8 bit)
Fill factor	98%
Light utilization	97%
Refresh rate	$60Hz$

Table 3.1 – Hamamatsu X10468-3 Properties

3.2 The Experimental Setup

The setup used for generating the arrays of tightly confining optical dipole traps is depicted in Figure 3.2. It starts of with an 1064 nm laser from Azur Light Systems which can provide a power of up to 40 W. The power is stabilized and controlled in a PI loop using an acousto-optic modulator (AOM) connected to a home build stabilization circuit which receives an input from a photo diode. Afterwards the beam is passed through two telescopes to magnify its $1/e^2$ diameter to 12 mm, matching the chip size of the SLM. The first one is formed by two 1-inch lenses with focal lengths $f = 75$ mm and $f = 150$ mm respectively. The second telescope is made up by a 1-inch lens with a focal length of $f = 50$ mm and a 2-inch lens with a focal length of $f = 300$ mm. Before the beam is shown onto the LC-SLM it is apertured by a circular iris of 12 mm diameter. The path after the SLM is split using a flip mirror. With this the light can be redirected onto a diagnostic path, where a camera can be placed. On the main path the SLM and the objective, focusing the light onto the atoms, are arranged together with two lenses in a 4-f setup. The two lenses, of which one is a 2-inch lens with a focal length of $f = 250$ mm and the other one a 3-inch lens with a focal length of $f = 800$ mm, form a telescope to magnify the beam in the SLM plane to the size of the objective of 40 mm. In the focus of the first lens the trap pattern is replicated. To block all light except for that used in the tweezers a rectangular aperture is placed in that plane. After the telescope the light is superimposed to the imaging path using an dichroic mirror with a custom coating from Lens Optics, highly reflective at 950 nm to 1100 nm and transmissive at 670 nm to 810 nm. The path is then split again by another flip mirror. It reflects the light either into another diagnostic path or onto a mirror which guides the light into the vertically mounted objective. This images the traps onto the atoms. To detect the atoms, scattered light is collected by the same objective and is split of from the trapping light by the dichroic again. It is then focused onto an scientific CMOS camera using a lens with focal length of $f = 250$ mm to spatially resolved image the atoms.

3.2.1 The in-Vacuum Objective

The objective used is custom made by Special Optics for in vacuum use. It has an effective focal length of 33.1815 mm, an entrance aperture of 40 mm diameter and an NA of 0.6. Furthermore it has a centered hole of 8 mm diameter to gain optical access along this axis. To let the SLM only utilize light which is diffracted by the objective and to avoid scattering of non-diffracted light in the vacuum chamber, the center of the beam on the SLM is guided such that it hits the aperture placed in the last telescope. This is achieved by displaying a blazed grating with 2π amplitude in the center of the SLM, which resembles a tilted mirror at this position.

3.2.2 Alignment

The alignment of beams on lenses with large diameter as used in this project is challenging and very critical at the same time. Small misalignments lead to significant aberrations and spoil the shape of the diffraction limited tweezers. To make the alignment significantly easier a trick with the SLM can be used. By displaying a phase pattern on it, which has strong phase discontinuities along certain lines, one can imprint those lines onto the collimated beam. The phase is not well defined any more at the points of the discontinuity and as consequence the beam shows no intensity at these positions. We used that method to imprint the shape of a target on the beam.

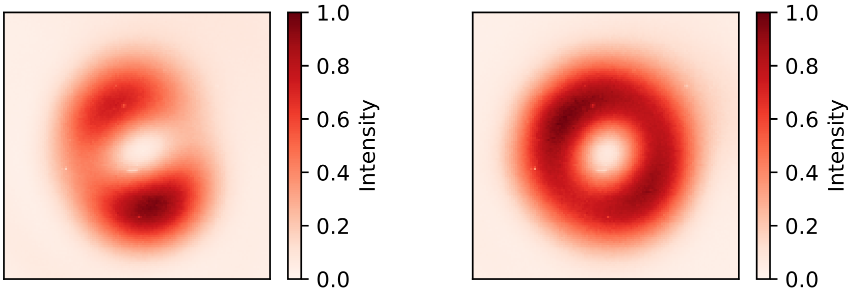

(a) Without correction (b) With corrections

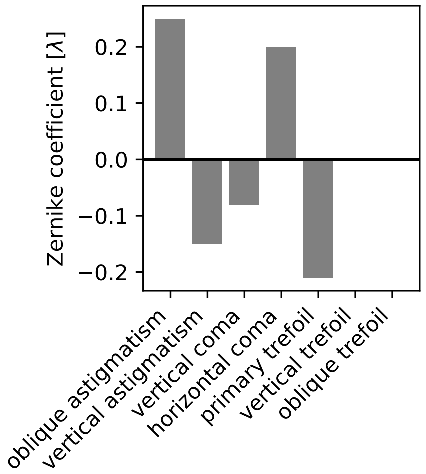

(c) Compensation coefficients

Figure 3.3 – Aberration correction with a doughnut mode. (a) The doughnut mode before adding a compensation pattern to the SLM. (b) The doughnut mode after adding a compensation pattern to the SLM. (c) The Zernike coefficients in wave lengths used in the compensation to go from (a) to (b).

This made it significantly easier to hit all the optical components centered.

3.2.3 Aberration Correction on the SLM

Even with the above described alignment trick, the beam passing the optical setup can acquire undesired distortions of the wave front. This can significantly worsen the point spread function and therefore in our case the shape of the trap. Those errors in the wave front are typically expanded in the basis of Zernike polynomials which is a good choice as the lower order polynomials can directly be related to typical lens errors or misalignment effects. Therefore the coefficients of the first few Zernike polynomials, referred to as Zernike coefficients, already capture the distortions in the wave front very well.

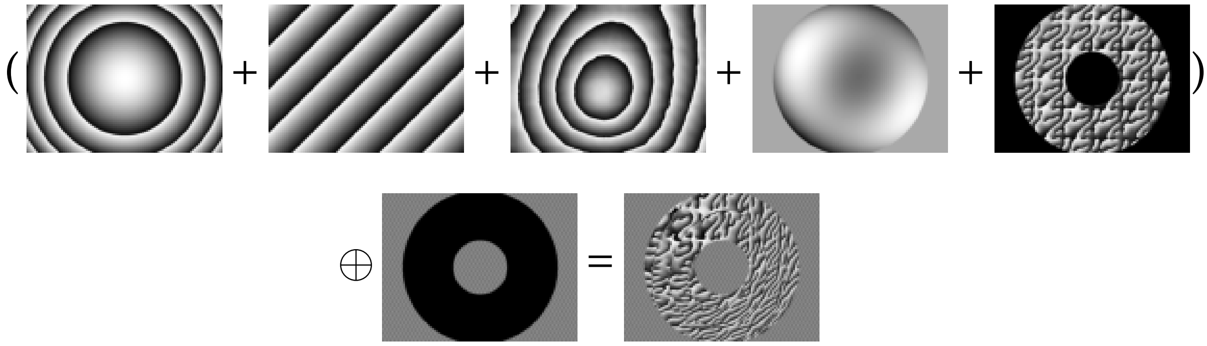

Figure 3.4 – Pattern construction. The parts of a phase image which is to be displayed on the SLM. In the top row from left to right a Fresnel lens pattern, a displacement pattern, a surface correction pattern provided by the manufacturer, an aberration correction pattern and the pattern for the specific trap array are shown. Those patterns are added together. In the bottom row a mask is shown which deflects all parts of the beam which do not hit the objective. Combining all the components properly results in the pattern after the equal sign, which is then displayed on the SLM.

To characterize and counteract the aberrations of the optical elements before the SLM and potentially residual deformations of the SLM itself, a scheme similar to the one described in [65] was used. A phase vortex where the phase is wrapped one time around the center is displayed on the SLM. In the focus of a lens this results in a doughnut shaped mode which is particularly sensitive to aberrations. By superimposing a phase pattern on the SLM which contains the lowest order Zernike polynomials the Zernike coefficients can be tuned such that the doughnut shaped mode is as symmetric as possible. The so found compensation pattern can now be used as a general compensation pattern for the aberrations.

For this characterization the first diagnostic path in the setup was used. Any additional lens in the beam before the camera changes the aberrations. To avoid this a Fresnel lens pattern with a focal length of 3 m was superimposed on the SLM instead to focus the beam onto the camera. The results are shown in Figure 3.3.

Unfortunately this method is infeasible for characterizing the aberrations after the last telescope. Due to the pixelation of the SLM the focal length, which is reliably producible with an Fresnel lens pattern, is very limited. This results in a minimal focal length after the telescope of several meters. In subsection 5.3.2 another method for measuring aberrations directly on the atoms is proposed for this setup.

3.2.4 Experimental Use

In order to use the described setup for imposing a trap array on the atoms a specific pattern needs to be shown on the SLM. Figure 3.4 illustrates how such a pattern is constructed. To modify the position of the whole array in the vertical direction a Fresnel lens pattern is used. A phase gradient is superimposed to position it in the horizontal plane. Due to the fabrication process of the SLM the surface has large scale irregularities. Those were already characterized by the manufacturer and a compensation pattern for this is supplied with the device. To compensate for the aberrations originating in the optical setup as described in the previous section another compensation pattern is added. Finally the actual pattern for a given trap arrangement is superimposed. How this is constructed is the main matter of the next section. To only utilize the light which hits the objective in the appropriate positions, as discussed in subsection 3.2.1, a mask is applied which diffracts undesired light to be blocked by an aperture. The so obtained pattern is then sent to the SLM.

3.3 Generation of Arbitrary 2D Arrays of Optical Dipole Traps

With the above described setup the experimental foundation is laid to show arbitrary arranged optical dipole traps to the atoms. Now we will turn to the question which phase pattern needs to be displayed on the SLM such that a certain arrangement of traps is generated. Before the actually used algorithm is introduced it is instructive to understand why this problem is highly non-trivial even for traps well separated from each other. With the insights gained we can immediately come up with an algorithmic approach to solve this problem. The so derived algorithm will be expanded in the next section to the well-known Gerchberg-Saxton algorithm [66] which is the basis of the actually implemented algorithm in the experiment.

3.3.1 The Phase Retrieval Problem for Separated Spots

When all distances between the tweezers are significantly bigger then their sizes one can approximate all tweezers to be independent, diffraction limited spots in the focal plane. This allows to ignore the particular shape of the traps for now. Each individual trap is then fully characterized by a relative phase of the light field with respect to some reference oscillating at the same frequency and the field amplitude in the center (θ_i, A_i), where i identifies the trap. In typical experiments carried out we want all the traps to have the same depth, but unfortunately even though the traps are non overlapping the amplitudes and the phases of the traps are not independent when a phase only SLM is used.

According to Fourier optics each diffraction limited trap is related to a single plane wave entering the objective. Therefore a whole array of traps is given by to a superposition of plane waves coming from different directions. In the Fourier plane of the objective this superposition is an intensity distribution with a particular shaped wave front, which is given by the Fourier transformation of the array of traps, each approximated by a delta distribution. With the use of a phase only SLM, this wave front can be mimicked and imprinted on a Gaussian beam, but the intensity pattern resulting from the interference of the plane waves can not be imitated. This problem is made more concrete by the following expression, which describes the light field T of the optical traps when only the wave front is adjusted but the intensity is left untouched.

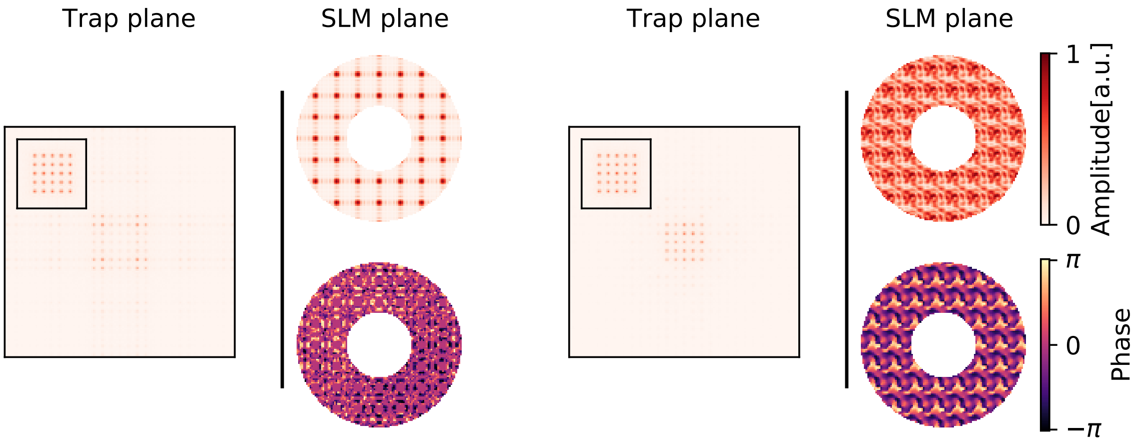

(a) Tweezers with the same phase (b) Tweezers with random phase

Figure 3.5 – Dependence of homogeneity on trap phase. (a) In the trap plane the calculated trap pattern when all traps are required to have the same phase. Very strong amplitude variation among the traps and significant ghost traps can be seen. The inset shows the originally desired pattern. In the SLM plane on the bottom the phase pattern which is to be given to the SLM to produce the trap pattern is shown. Above, the ideal input amplitude pattern which would lead together with the phase distribution below to the ideal tweezers pattern. The overlap with an almost flat Gaussian beam is apparently small. (b) The same as (a) but now the traps are chosen to have random relative phases among each other. The tweezers pattern is way better reassembled with an Gaussian input beam on the SLM. Still ghost traps appear and the non-uniformity among the trap intensities is in the order of 20%. The overlap of the intensity distribution in the SLM plane which would lead to a perfectly homogeneous trap pattern has a seemingly higher overlap with almost flat Gaussian beam.

$$T = \mathcal{FT}\left(\frac{B(x,y)}{|\sum_i P_{(\theta_i,A_i)}(x,y)|}\sum_i P_{(\theta_i,A_i)}(x,y)\right) \tag{3.1}$$

Here $\mathcal{FT}$ denotes the Fourier transformation to which the relation between the light field in the diffraction plane and the real plane of the objective reduces in the Fourier optics limit. $B(x,y)$ is the field amplitude of the incoming beam on which the new wave front is imprinted. $P_{(\theta_i,A_i)}(x,y)$ denotes the plane wave associated with a single tweezers with amplitude A_i and phase θ_i. The term under the Fourier transform keeps the wave front of the super positions of plane waves but replaces the amplitude by the amplitude of the beam incident on the SLM. To see how this deviates from the intensity distribution of uniform traps one can rearrange this expression. By just adding and subtracting a term in Equation 3.1 we arrive at the following expression

$$T = T_{ideal} + \mathcal{FT}\left(\left(\frac{B(x,y)}{|\sum_i P_{(\theta_i,A_i)}(x,y)|} - 1\right)\sum_i P_{(\theta_i,A_i)}(x,y)\right) = T_{ideal} + T_{error}$$

where $T_{ideal} = \mathcal{FT}(\sum_i P_{\theta_i,A_i}(x,y))$ is the originally desired optical field for a specific configuration of tweezers. The T_{error} after the second equal sign represents the second summand after the first equal sign. It contains how the ideal field amplitude T_{ideal} is modified by the change to the beam on the SLM. We assume that $B(x,y)$ represents a large scale beam, meaning it only has spatial frequency components smaller then the inverse objective size, as is the case in most SLM applications. The term in the Fourier transformation of T_{error} has the same short scale periodicity as the term in the Fourier transformation of T_{ideal}. This means when the ideal tweezers pattern has a periodicity, T_{error} will also show spots with the same periodicity. It will therefore create spots which are interfering with the ones created by T_{ideal} and spoil there amplitudes and phases. Furthermore it will create spots outside the pattern following the same periodicity which will be referred to as ghost traps. This can be seen in Figure 3.5 where a 5 by 5 array of homogeneous spots was first Fourier transformed then the field amplitude was replaced by the field amplitude of large scale Gaussian beam incident on the SLM and a Fourier transformation back was performed. This is exactly the expected result when one would just mimic the phase distribution but not the intensity distribution. Notably in both shown cases the originally homogeneous intensity distribution among the tweezers is lost and around the array one can see the appearance of ghost traps

By Parseval's theorem and the triangle inequality the L_2-norm, denoted as $|\cdot|_2$, of T_{error}, which is proportional to its total power, is always smaller then or equal to the L_2-norm of the deviation between $B(x,y)$ and $|\sum_i P_{(\theta_i,A_i)}(x,y)|$

$$|T_{error}|_2 \leq \left| |\sum_i P_{\theta_i,A_i}(x,y)| - B(x,y) \right|_2 . \tag{3.2}$$

Therefore the discrepancy between the intensity distribution of the incident beam and the intensity distribution one finds by Fourier transforming the trap array yields an upper bound for the deviation from having homogeneous tweezers. It turns out that this also provides one with a good heuristic measure on the homogeneity. This is illustrated in Figure 3.5 as well. For the case of all tweezers having the same phase, the overlap between the amplitude pattern coming from the superposition of plane waves and the almost flat Gaussian input amplitude is small. This leads to a large T_{error} and shows up in large corrections of the amplitudes in the pattern and strong ghost traps. In case of the tweezers having random phases one can already tell by eye that the overlap between the incident beam and the amplitude of the Fourier transformation is significantly bigger and one sees a huge reduction of amplitudes in the ghost traps and the tweezers are significantly more homogeneous compared to the other case.

3.3.2 A Toy Algorithm for Homogenous Tweezers Arrays

Even in the case of random phases there are significant deviations on the order of 20% from the desired pattern. This raises the need for a clever way to optimize for the

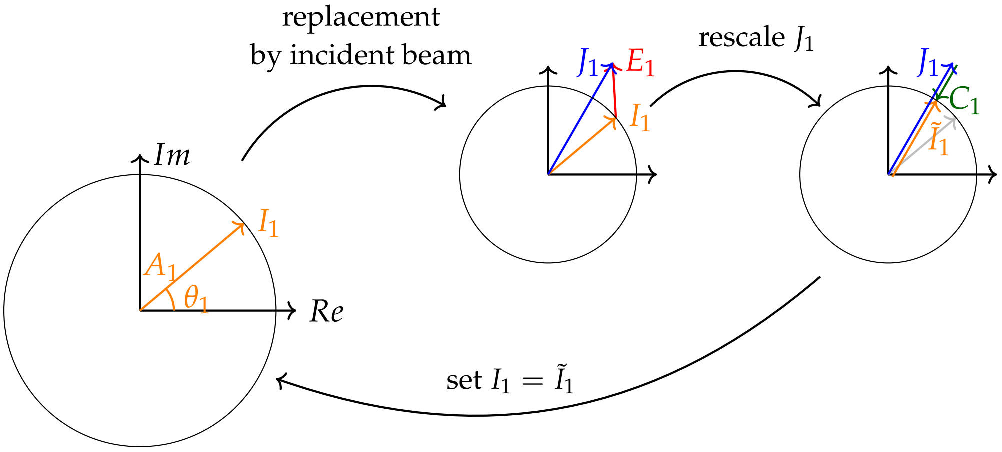

Figure 3.6 – Phasor domain of toy algorithm. The toy algorithm described in the main text. One starts at the left with an initial guess of the phasors with the desired amplitude. Then one goes to the plane wave domain, replaces the amplitude distribution with that of the incident beam and goes back to the phasors domain. This results in a modification of I_1 by a new phasor E_1 yielding J_1. Subsequently J_1 is rescaled to the desired amplitude by adding C_1. This results in the new phasor $\tilde{I}_1$. To start the next iteration I_1 is replaced by $\tilde{I}_1$.

minimal non-uniformity by choosing the relative phases of the traps appropriately. Various different approaches had been realized in the past. Here we take the way of an iterative Fourier transformation algorithm (IFTA) and discuss how such an algorithm indeed can seek for a maximal homogeneity among the traps.

As said right in the beginning of the previous section each spot can be described by the tuple (θ_i, A_i). In the following it is instructive to represent this by a so called phasor, which can be understood as a vector in the complex plane, enclosing the angle θ_i with the real axis and having a magnitude of A_i. To not lose track of the ghost traps, which only appear at initially known positions as argued before, we include traps at those positions with a desired amplitude $A_i = 0$ in our algorithm. This is not required for the algorithm to work, but will make the subsequent argument for its convergence easier to follow. We start from an initial guess of the tweezers phase θ_i and a desired amplitude A_i for each trap, described by the phasor I_i. The index again denotes the chosen trap. To simplify notations we will only look at the phasor I_1. Transforming all traps to the plane wave superposition, replacing the amplitude by the incoming beam amplitude and transforming back adds a correction phasor E_1 to I_1. The sum of both phasors is denoted as J_1. This was already described above stated in terms of phasors. Now we will add another correction phasor C_1 by hand which brings J_1 back to the desired amplitude but keep its orientation. With the so found new phasor $\tilde{I}_1$ the procedure is repeated. The $\tilde{I}_1$ together with all the other $\tilde{I}_i$, found in the same manner, substitute the I_i of the previous step. This procedure is depicted in Figure 3.6.

To see that this converges to a desired solution one notes that $|C_1|^2 \leq |E_1|^2$, with $|\cdot|^2$ denoting the squared length of the phasors. This is obvious from geometrical considerations. Furthermore the relation $|T_{err}|_2 = \sum_i |E_i|^2$, where it was used that all traps are modeled by delta distributions, holds and allows for the application of

Parseval's theorem in the phasor picture. We find that

$$|T_{err}|_2 = \sum_i |E_i|^2 \geq \sum_i |C_i|^2 = |\sum_i P_{C_i}(x,y)|_2$$

where $\sum_i P_{C_i}(x,y)$ denotes the plane wave superposition for all the tweezers characterized by the phasors C_i. Note that this is nothing but a Fourier expansion. In the last equal sign the adopted Parseval's theorem was applied. Using $|\sum_i P_{J_i}(x,y)| = B(x,y)$, which is true by construction, we find

$$|\sum_i P_{C_i}(x,y)|_2 = |\sum_i P_{J_i}(x,y) - \sum_i P_{\tilde{I}_i}(x,y)|_2 \geq \left| B(x,y) - |\sum_i P_{\tilde{I}_i}(x,y)| \right|_2$$

where the triangular inequality was used. All together and by applying Equation 3.2 we find

$$|T_{err}|_2 \geq \left| B(x,y) - |\sum_i P_{\tilde{I}_i}(x,y)| \right|_2 \geq |\tilde{T}_{err}|_2$$

where $\tilde{T}_{err}$ is associated to $\tilde{I}_i$. With that it is shown that the corrections T_{err} reduce or stay the same after each iteration. This makes the algorithm converging.

3.4 The Gerchberg-Saxton Phase Retrieval Algorithm and Modifications

The algorithm described in the previous section only works in the case of well separated tweezers and it can only leverage the potential of the fast Fourier transform algorithm (FFT) introduces by Cooley and Tukey [67] in special cases. Fortunately, it is just a version of the Gerchberg-Saxton algorithm, which will be introduced in the following, boiled down to the specific problem of septerated tweezers.

3.4.1 Phase Retrieval Using the Gerchberg-Saxton Algorithm

The Gerchberg-Saxton algorithm, analog to the algorithm described above, relies on back and forth propagation between the real plane and the diffraction plane using a suitable and cost-efficient propagator. Most commonly the fast Fourier transformation is used for this as for most systems the corresponding approximations hold. The following discussion will focus on this case. To improve the accuracy other propagators have been utilized in the past with the drawback of being significantly more costly in computation time, but achieving improved results especially for large scale potential landscapes [68].
The input to the algorithm are two amplitude distributions of which one corresponds to the incident beam profile in the plane where the SLM sits, referred from now on as SLM plane, and the other one to the desired amplitude distribution in the Fourier plane, wich we will refer to from now on as tweezers or trap plane. Both are evaluated on a two dimensional grid of the same dimension $N_x \times N_y$, which are interlinked in their length scales by the Fourier transformation [69]. The physical dimension of a

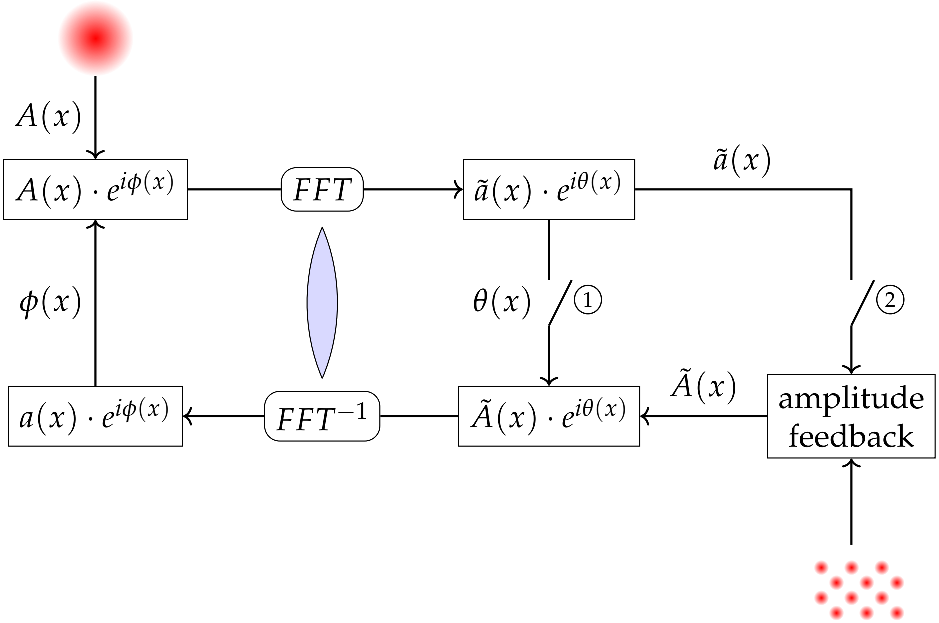

Figure 3.7 – Modified Gerchberg-Saxton algorithm. case ① closed and ② open: The usual Gerchberg-Saxton (GS) algorithm to find a phase pattern for the SLM. The starting point is the upper left box. The initial phase $\phi(x)$ is chosen at random. ① closed and ② closed: The weighted Gerchberg-Saxton (WGS) algorithm. Same as the GS, but now the individual traps are attenuated or amplified depending on the outcome of the FFT. The exact form of this is discussed in the main text. ① open and ② closed: The Gerchberg-Saxton algorithm with fixed phase (FixPhaseGS). The phase is not put forward any more in the trap plane. Instead always the phase profile of the first iteration is used. The only way the SLM phase pattern can evolve is via to the feedback mechanism of the weighted Gerchberg-Saxton algorithm(WGS). All those cases are combined to give a high performing algorithm for finding the SLM pattern.

unit in the tweezers plane $\tilde{\Delta}_x \times \tilde{\Delta}_y$ is related to the dimension of a unit in the SLM plane $\Delta_x \times \Delta_y$ by

$$\tilde{\Delta}_x \times \tilde{\Delta}_y = \frac{\lambda f}{N_x \Delta_x} \times \frac{\lambda f}{N_y \Delta_y}$$

and vice versa. A single iteration of the algorithm looks as follows:

step 0: preparation for first iteration. In case of the iteration step to be the first one, the amplitude distribution of the incident beam is combined with either a random or initially guessed phase distribution. This is considered to be light field in the SLM plane.

step 1: propagate to trap plane. The light field with the incident beam profile as amplitude and the phases from the previous step is propagated to the trap plane using the fast Fourier transformation.

step 2: manipulate in trap plane. In the trap plane we keep the calculated phase distribution but replace the amplitude distribution by the desired amplitude distribution.

step 3: propagate back to the SLM plane. The newly obtained light field is propagated back to the SLM plane using the inverse fast Fourier transformation.

step 4: manipulate in SLM plane. Analogous to the manipulation in the trap plane we keep the phase information of the calculated light field but replace the amplitudes by the amplitude distribution of the incident beam.

step 5: repeat or stop. The algorithm is either continued repeating from step1 again or stopped. We typically stop the algorithm after a view tens of iterations as the convergence rate to the desired tweezers amplitudes gets very small and we recycle the output as the initial guess for a modified version of the Gerchberg-Saxton algorithm.

The algorithm is depicted in Figure 3.7. An argument for the convergence goes along the same lines as for the toy algorithm introduced in the previous section. One just needs to replace the phasor of the traps by the phasor of the individual pixels in the tweezers plane.

3.4.2 Modifications to the Gerchberg-Saxton Algorithm

The Gerchberg-Saxton algorithm as introduced in the preceding section is not guaranteed to converge within a realistic number of iterations and indeed the convergence to the desired amplitudes in the tweezers stops after a view tens of iterations with a rather unsatisfying result. Fortunately, the algorithm can be used as a starting point for more efficient algorithms by making small adjustments to it, of which the MRAF [70] and OMRAF [68] are examples. In the case of generating multiple diffraction limited dipole traps more specific modifications can be made. A first improved version uses the amplitudes of the calculated traps in the above introduced step 1 and feeds them forward to step 2. For this modification it is required that step 1 already produces tweezers at the right position, but with potentially wrong amplitudes. This is sometime called weighted Gerchberg-Saxton algorithm (WGS) [71]. Within this, step 2 is replaced by the following:

step 2′: manipulate in trap plane. The amplitudes A_i^n, with n denoting the tweezers and i indexing the iterations of the algorithm, of the tweezers array in the calculated pattern are extracted. The phases of the calculated pattern are kept and the amplitude is replaced by an amplitude distribution where the individual tweezers are weighted with the factors

$$g_i^n = \frac{A_{goal}^n}{A_i^n} \cdot g_{i-1}^n \tag{3.3}$$

where A_{goal}^n is the desired amplitude for the trap n.

A second modification follows along the line of the first modification and requires that step 1 already produces trap amplitudes close to the desired ones [72] .

step 2″: manipulate in trap plane On the iteration the phase distribution of the calculated light field ϕ_1 in the trap plane is saved. From that iteration step on the calculated intensity distribution is used to calculate the weighting factors as in Equation 3.3. The amplitude of the light field is replaced by the desired amplitude distribution with each trap weighted with the corresponding weighting factor. The phase distribution is replaced by the phase distribution ϕ_1. This implementation will be referred to as fixed phase Gerchberg-Saxton algorithm (FixPhaseGS).

How both modifications influence the convergence of the algorithm will be discussed in the next section.
As optical systems always incorporate imperfections like aberrations, the Fourier transformation might be an insufficient propagator and the trap pattern might still show deviations from the desired trap depth exceeding those of the calculation. Instead of using the calculated amplitude distributions one can use a camera placed in the trap plane or in-situ measurements of the trap depth with the atoms to find the weighting factors g_i^n [73].

3.5 Numerical Results and Stability Analysis

The algorithm used to obtain the phase distribution, which is to be displayed on the SLM, is a combination of the GS, the WGS and the FixPhaseGS. In this section the concrete implementation is explained and the convergence of the algorithm as well as the stability of the result are discussed.

3.5.1 Implementation of the Algorithm

As input to the algorithm the positions and intensities of the desired traps as well as the array dimension $N_x \times N_y$ and dimension of a unit in the SLM plane $\Delta_x \times \Delta_y$, as introduced in subsection 3.4.1, need to be supplied. For the first step 10 iterations with the GS are performed. Therefore the traps are modeled as Gaussians with a waist given by the width of the point spread function of the objective used in the experiment. These are summed together and evaluated on the grid in the trap plane. The resulting matrix will be referred to as $\mathcal{T}_{array}$. The intensity distribution of the beam in the SLM plane is modeled as well as a Gaussian beam which is cut by an outer aperture with the radius of the objective and an inner aperture with the radius of the hole of the objective. This is evaluated on the grid in the SLM plane and the result will be referred to as $\mathcal{S}_{beam}$. $\mathcal{T}_{array}$ and $\mathcal{S}_{beam}$ are then used as the amplitude distributions to run the GS. To incorporate the discrete nature of the phase shifts on the SLM, the propagator from the trap plane to the SLM plane is extended to yield only discretized phase values.
The second step runs 10 iterations with the WGS on the result obtained in the previous

step. To be able to do the weighting the amplitude distributions of the traps are now individually evaluated on the trap plane grid and referred to as $\mathcal{T}^n_{trap}$ where n indicate the trap. Note that $\mathcal{T}_{array} = \sum_n \mathcal{T}^n_{trap}$. The weighting factor g^n_i for each trap is evaluated using

$$a^n_i = \frac{|\tilde{\mathcal{T}}_i \times_{el} \mathcal{T}^n_{trap}|_1}{|\mathcal{T}^n_{trap}|_1}$$

$$g^n_i = \frac{\sum_n a^n_i}{a^n_i} g^n_{i-1}$$

where $\tilde{\mathcal{T}}_i$ denotes the resulting amplitude distribution matrix from the propagation to the trap plane, $\times_{el}$ is the elementwise multiplication of matrices and $|\cdot|_1$ is the matrix 1-norm or respectively the sum over all absolute values of the matrix entries. The new $\mathcal{T}_i$, which is the substitute of $\tilde{\mathcal{T}}_i$, is given as

$$\mathcal{T}_i = \sum_n g^n_i \mathcal{T}^n_{trap}.$$

The propagators are identical to those of the first step.

The third step runs 20 iterations with the FixPhaseGS starting with the result of the previous step. Also the g^n_{10} are handed over to this step and used as a starting point for weighting factors. The implementation is similar to the one of the WGS with the only difference that the phase distribution $\tilde{\theta}_i$ after the propagation to the trap plane is replaced by $\tilde{\theta}_1$. The so obtained phase pattern is then used in the experiment.

In the subsequent two section the algorithm and the results will be characterized.

3.5.2 Numerical Results

To investigate the convergence behavior of the algorithm introduced in the previous section, it was run as described. In each iteration step the field amplitude was extracted using the same method as for the calculation of the weighting factor in the implementation of the WGS and FixPhaseGS. The power distribution among the tweezers is found by squaring this result. To compare the used algorithm to algorithms just using GS or GS together with WGS the evaluation was branched whenever the algorithm changed from one GS derivate to the next and the previously used algorithm was continued in parallel. For a single exemplified run of the algorithm, which generated a 5×5 square array, the results are illustrated in Figure 3.8. While the GS reaches 10% standard deviation in the intensities among the tweezers the modified versions of the GS outperform this by 2 and 4 orders of magnitude after 100 iterations, where all the algorithms have settled. One notes that while the GS algorithm only saturates the other algorithms eventually go up again. The strict convergence derived for the Gerchberg-Saxton algorithm does not hold with the same rigor for the other derivates. The intensity and phase deviations of the individual traps from their final value are also shown in Figure 3.8. While there is a clear kink visible in the behavior of the intensity when the switching from the GS to the WGS happens, the qualitatively behavior of the phase is only weakly effected.

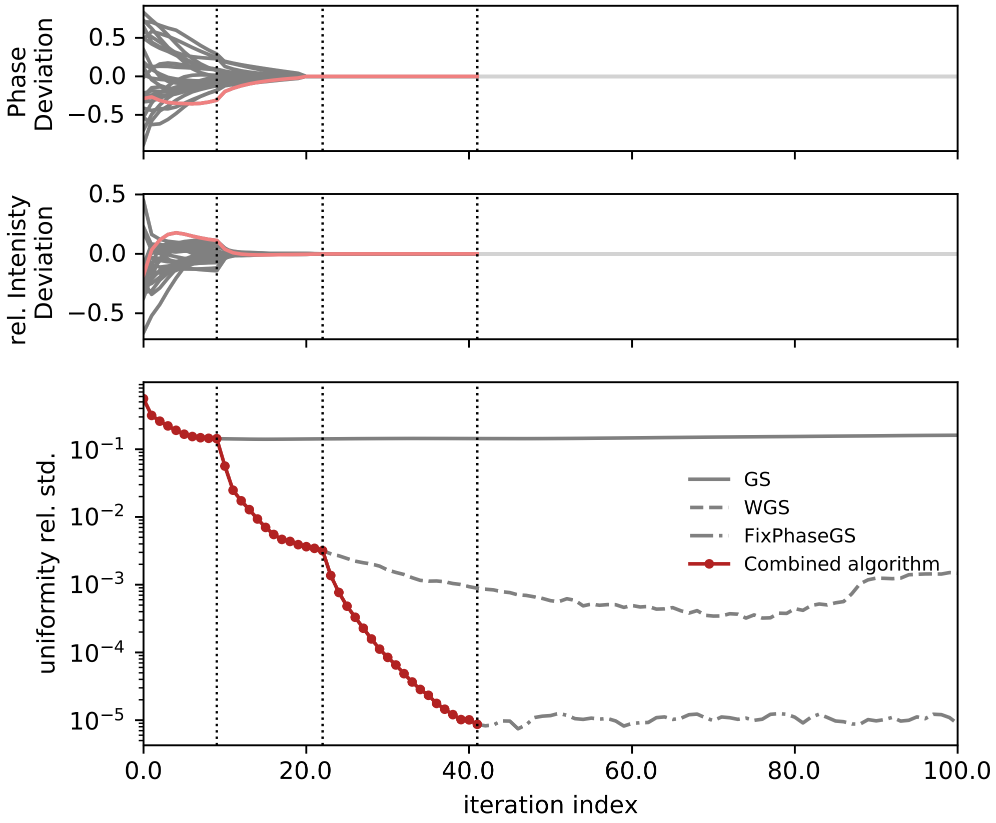

Figure 3.8 – Convergence characteristics of the algorithm. The top panel shows how the relative deviation of the phase from its final value evolves with the iteration number. A randomly chosen trap is highlighted in red for demonstration. The middle panel shows the same as the top panel for the relative deviation of the final intensity. The lower panel shows how the algorithm used in this work (red) compares to other algorithms not involving all the modifications of the GS. The data was generated by a single run of the algorithm. Whenever the algorithm changed, the original algorithm was branched of and continued to 100 iterations. All graphs share their horizontal axis.

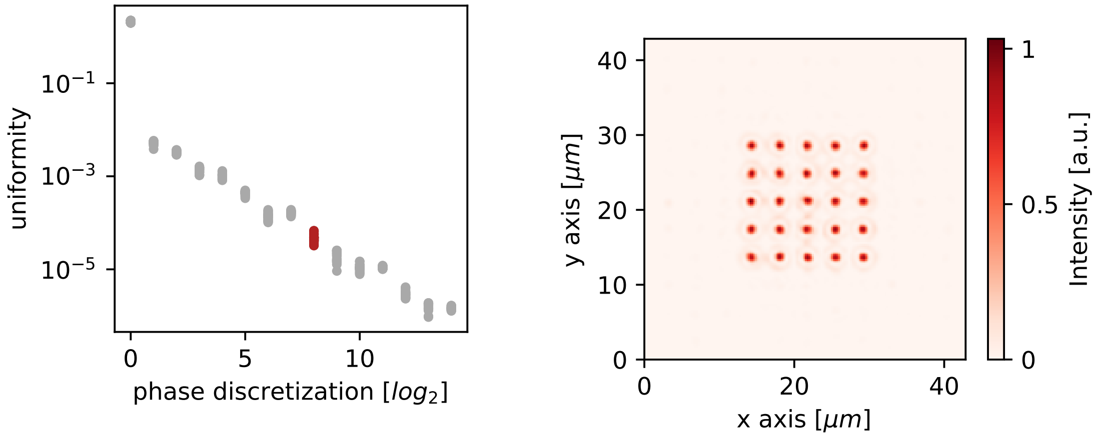

(a) Final homogeneity depending on phase discretization

(b) Generated tweezers pattern

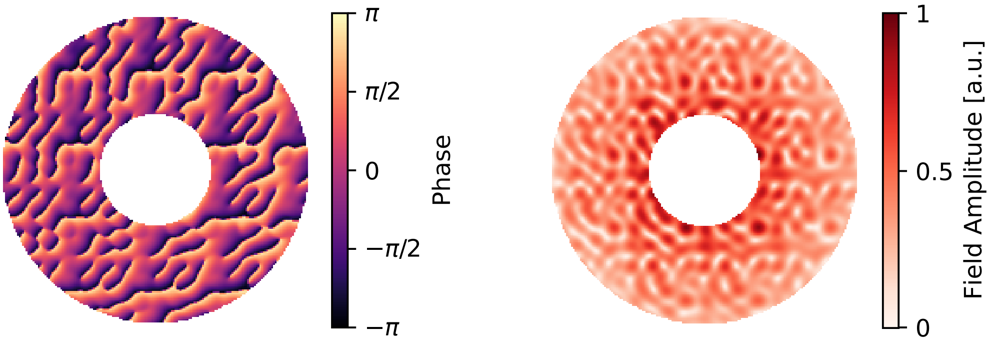

(c) Resulting phase map for the SLM

(d) Ideal input beam

Figure 3.9 – Convergence and result of the algorithm used in our experiments. (a) The resulting trap uniformity of the algorithm for different numbers of discrete phase steps (gray dots). The phase discretization of the Hamamatsu SLM is shown in red. (b) The result of the algorithm in the tweezers plane. (c) The resulting phase pattern of the algorithm which is used on the SLM. (d) The ideal input beam which, together with the phase pattern, would result in the ideal trap array.

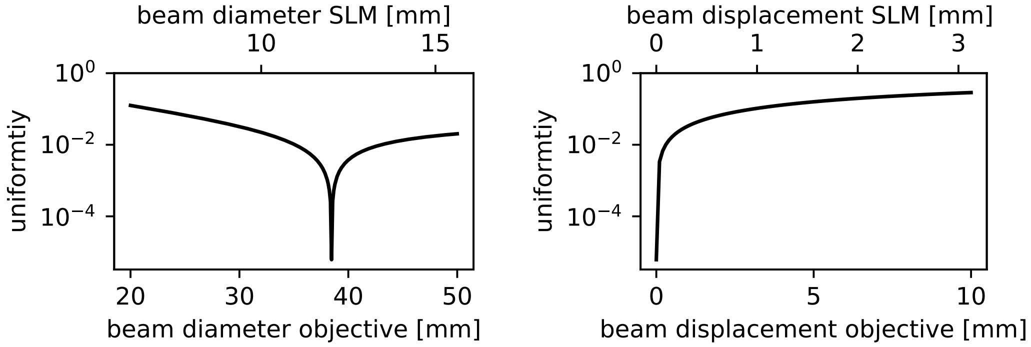

(a) Beam diameter variations

(b) Beam position variations

Figure 3.10 – Stability against variations of beam parameters. A calculated pattern was numerically exposed to different input beams and the homogeneity of the resulting arrays is shown. (a) The resulting uniformities of the pattern for different beam diameters. The pattern was calculated for a $1/e^2$-diameter of 12 mm on the SLM. The upper horizontal axis shows the diameter the considered beam has on the SLM and the lower horizontal axis shows the diameter on the objective. 1 mm deviation in the beam diameter results in an non-uniformity of 1%. A 10% non-uniformity is reached when the beam diameter deviates by 5 mm on the SLM. (b) The same as in (a), but with varying displacement of the beam. At a 1 mm deviation the non-uniformity reaches about 10%.

Figure 3.9 illustrates the final uniformity of the traps depending on the discretization of the phase in the SLM plane as well as the final result of a single run of the algorithm. One can observe a linear increase in the homogeneity with an increasing number of discrete steps to sample the phase. When no phase discretization is applied an exponential decrease in the uniformity with iteration number, which does not saturate, was observed. This can be understood from a linear scaling behavior of the FixPhaseGS with the deviations in the trap depth and the correction for this. This scaling is a result of the linearity of the Fourier transformation, Parseval's theorem and the linearity of the weighting factor with deviations from the desired field amplitude. That hints towards that the algorithm is getting close to a uniformity limit imposed by the discretization of the phase.

The amplitude distribution in the SLM plane which would lead, together with the obtained phase distribution, to a perfectly homogeneous power distribution among the tweezers qualitatively has an envelope resembling that of the incoming Gaussian beam. But one also notes that the amplitude distribution strongly fluctuates on shorter scale. This does not necessarily influence the uniformity in the pattern, but leads to the appearance of ghosts traps. Therefore this limits the efficiency of the conversion from incident power on the SLM to the power add up over all desired traps.

3.5.3 Sensitivity to Beam Misalignment

Another important benchmark is the sensitivity of the generated pattern to typical experimental imperfections. Even the best algorithm with the best result is not usable if a slight deviation from the assumed input beam in the experiment spoils the uniformity. Therefore the sensitivity to displacements and deviations in the waist of beam incident on the SLM of the uniformity where evaluated. The results are shown in Figure 3.10. While a mismatch of the beam waist of 2 mm on the SLM only lead to a non-uniformity of about 1%, a displacement of the beam of 1 mm on the SLM leads to about 10% non-uniformity.

3.6 Experimental Results

In this section a typical sequence to load atoms into the optical tweezers as well as a way of imaging the atoms will be described. Following that, an in-situ characterization of trap frequency, trap depth and a thermometry will be carried out.

3.6.1 Sequence to Load Atoms in the Optical Tweezers

Several conditions need to be fulfilled to be able to load atoms into the optical tweezers. The optical dipole traps are conservative in character, meaning a single atom coming form free space would just pass through the potential without ever being bound to it. To be able to trap the atom it needs to be sufficiently cold and sufficiently coupled to a thermal bath to dissipate enough kinetic energy to not be able to climb out of the trap again. This can either be achieved with a sufficiently dense cloud of atoms which allows for evaporation into the traps [74] or by coupling to a photonic bath in form of laser cooling, as typically done and also done in this thesis [55]. Unfortunately, neither a red molasses on the D2-line nor a gray molasses on the D1-line in Potassium-39 has a working region, in terms of their detuning, large enough to work properly inside and outside the 1064 nm trap at the same time. This is not only due to the ground state light shift but critically worsened by the large light shift of the excited states of the D-lines in the presence of the 1064 nm trapping light. To circumvent this problem the approach taken in the present experiment is to intertwine trapping and cooling in the time domain, meaning that the trapping and cooling light are never on at the same time but interchange their on-times in a rapid succession. In doing so, the light shift from the trap is effectively eliminated [75]. This fast switching of the light will be referred to as chopping. As long as the rate with which the switching happens is sufficiently above the trap frequency and high enough to prevent the atoms in the traps from leaving it while it is off, this approach had proven to work very well with the red molasses. With the gray molasses this approach failed which is most probable due to the fact that the gray molasses relies on the mapping of atoms in dark states to be cold. When the cooling light is switched off and on again the dark state had evolved partially into bright states with a rate of the hyper fine structure splitting of the ground state of 461 MHz. When the switching frequency is not much faster than this, saying that cold atoms are the one in dark state fails and the gray

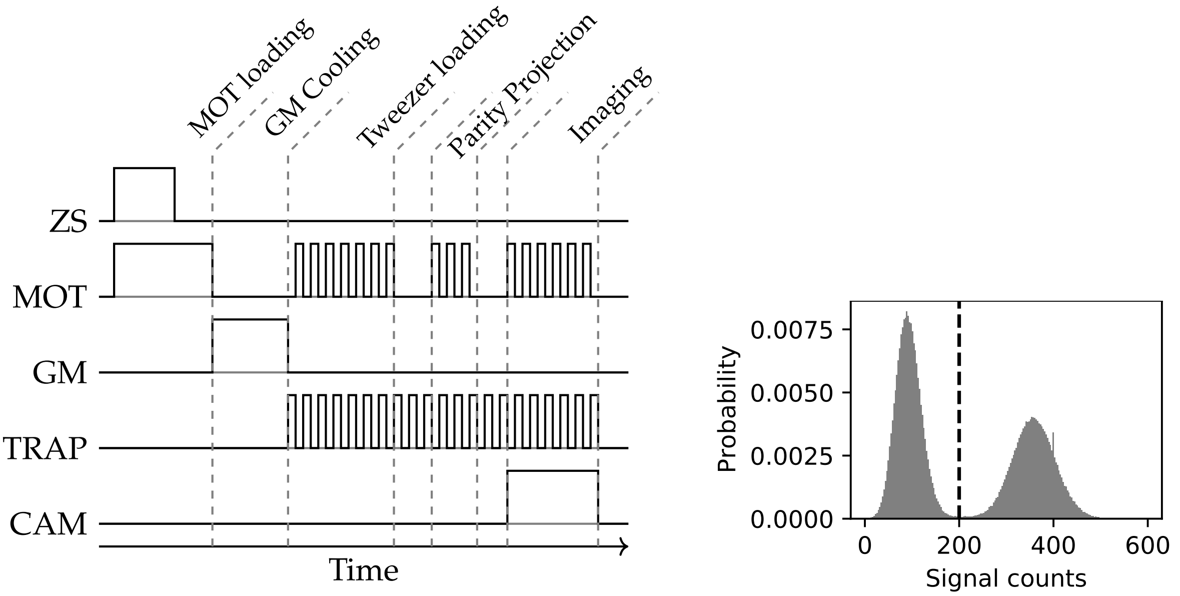

(a) Timing sequence for loading and imaging

(b) Histogam of camera detected photons

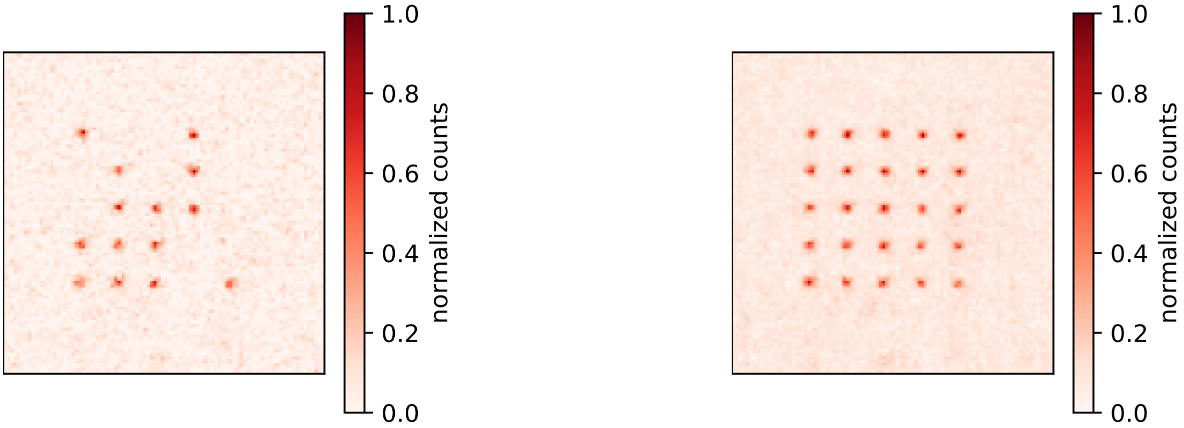

(c) Single shot camera signal

(d) Averaged camera signal

Figure 3.11 – Loading and imaging single atoms in optical tweezers. (a) The on/off timing of lasers for the Zeeman slower (ZS), the magneto optical trap (MOT), the gray molasses (GM) and the dipole trap array (TRAP) as well as the timing of the imaging camera (CAM) are depicted. The time axis is not to scale. The purpose of the sequence is to load atoms in the traps and to image them immediately afterwards. (b) A typical histogram of the signal from the camera, when only regions of interest containing a few pixels are considered. The regions of interest are placed at the positions where a signal from a trapped atom is expected. The black dashed line is placed at a typical threshold. When a region of interest shows a signal above this the trap is considered as occupied. (c) Camera picture after a single run of the sequence depicted in (a). (d) averaged camera signal over many sequence runs.

molasses is subject to heating. This requirement on the switching however exceeds the constraints imposed by the trap with a trapping frequency 3 orders of magnitude lower.

In addition to that, to achieve a sufficient loading rate into the tweezers, one wants as much atoms as possible in the neighborhood of the trap in a velocity class which can be cooled fast enough, when the atoms are passing through the trap, to not eject them again. For that, one wants a sufficiently cold and dense cloud of atoms to load the tweezers from.

An experimental timing sequence which takes all these considerations into account is shown in Figure 3.11. It starts with a MOT which is loaded for 250 ms from a Zeeman slower. When the Zeeman slower is switched off the MOT is held for 20 ms and optically compressed by ramping the beam powers and detunings within 50 ms. Subsequently the MOT is switched of and the atom cloud is further cooled by a gray molasses for 20 ms. To load the atoms in the tweezers the MOT light, which is now tuned to a red molasses configuration, as well as the tweezers light are chopped with 1.4 MHz as described before. After 40 ms of tweezers loading the MOT light is switched off again. A delay of 30 ms allows the residual atoms which are not trapped to escape. As now potentially multiple atoms reside in the individual traps one has to make sure to eject all but one of them in the next step. This is done by again turning on the chopped MOT light. It is close enough red detuned to lead to light assisted collisions which in the majority of cases leads to a loss of both atoms, which had participated in the collision, from the trap. Thus it projects an even number of atoms to no atoms left in the trap and an odd number of atoms to a single atom left. This is known as parity projection. One notes that this procedure achieves the goal in a rather poor fashion since it limits the loading probability of a single trap to roughly 50%. In the sequence this mechanism is exploited for 10 ms. With this the goal of loading single atoms in the trap is achieved and one can take this as the starting point for all kind of experiments. However in most cases it is desirable to at least know which of the traps are loaded and which are not. For this purpose the chopped MOT light is switched on again and the fluorescence signal of the atoms is spatially resolved detected with the imaging path described in section 3.2. The camera is exposed for 10 ms.

Results of this imaging are shown in Figure 3.11. On the shown histogram one can clearly distinguish two peaks, one coming from the background signal of the camera and the other one from a single atom in the trap. The absence of higher peaks proofs that the MOT light indeed only leaves one or zero atoms in the traps. The strongly reduced probability of occurrence for count numbers between the peaks allows the conclusion that losses of atoms during the imaging are small. The picture taken in a single run of the experiment indeed shows that only about 50% of the traps are loaded. An analysis of about 8500 shots yielded the loading probability to be 54% with a standard deviation of 3% between the different tweezers. The average picture shown is taken from the same 8500 shots.

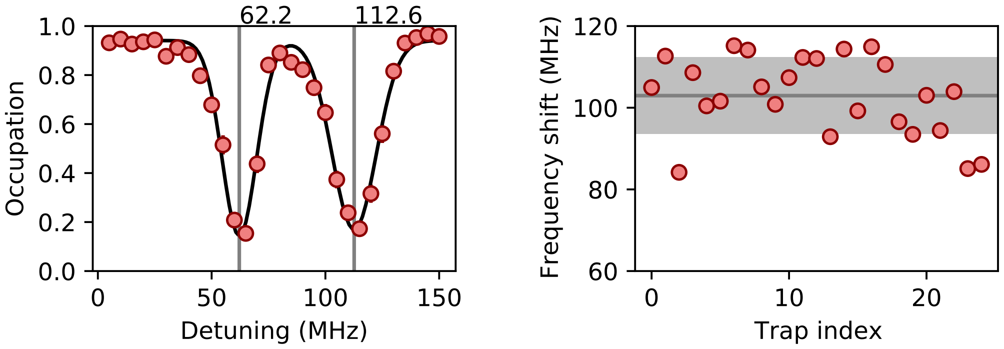

(a) In-situ D1-line spectrum

(b) Frequency shift of individual tweezers

Figure 3.12 – Spectroscopy on the D1-line of trapped atoms. (a) Shown is the loss probability of an atom in a single trap when light on the D1 line with varied detuning is incident on it. The experimental data is represented by the round markers. The statistical error bars are below the marker size. Two well separated peaks can be resolved. The one lower in frequency corresponds to a transition to the $4P\ F = 1$ hyper fine state and the other one to the $4P\ F = 2$ state. The offset frequency is set to resonance on the free space $4P\ F = 2$ resonance. Two Gaussians where fitted to the data represented by the gray curve. The position of the resonances where extracted from the fit and represented by the vertical lines. Above the resonance frequencies in MHz are written. The width of the measured lines is 10 MHz which is 4 MHz above the natural line width. (b) Shown are the line shifts of the $4P\ F = 2$ transition of all traps in a 5 by 5 array with a spacing of 10 µm. The vertical dark gray line indicates the mean shift among all traps and the light gray region the standard deviation from it.

3.6.2 In-situ Characterization of the Traps

To characterize the shape of the traps a direct characterization with the atoms is carried out. Therefore the response of the loading probability to scanable parameters of the experiment is measured. This allows to deduce the trap depth, the trap frequencies and the temperature of the trapped atoms.

Light Shift Measurement

To determine the peak intensity in each trap the different light shifts of the $^2S_{1/2}$ and $^2P_{1/2}$ as found in section 2.5 are exploited. They lead to a shift in the D1-line which can be probed by a near resonant laser on this transition. Therefore the detuning with respect to the free space D1 transition is scanned within several runs of the experiment. When the laser gets resonant to the line shifted by the trap the atom experiences strong recoil heating and gets expelled from the trap. The sequence used for this measurement extends the sequence discussed in the previous section. After taking the image the trap light is switched from the chopping mode to the continuous mode of operation. Subsequently the gray molasses light, which is put at a certain detuning, is switched on for 1 ms. This time was chosen for good contrast but no

saturation. After that, another picture is taken the same way as the first picture.To extract the probability of keeping the atom for a certain detuning multiple runs for each detuning are performed.
The results obtained from a single trap, which is part of a 5 × 5 rectangular pattern with 10 µm spacing, are shown in Figure 3.12. One can clearly see two resolved lines which originate from the hyper fine structure of the $^2P_{1/2}$ level. A function with two Gaussians is fitted to the data to extract the resonance frequency. Using a Gaussian as a model for the line is justified by the Doppler broadening and a Gaussian type of broadening, which comes from different light shifts at different positions inside a single trap. The same type of analysis is carried out for all the traps in the pattern and is shown in Figure A.1. The extracted resonance shifts of the $F' = 2$ transitions for all the traps in the pattern are shown in Figure 3.12. From this we find the mean ground state shift and therefore the trap depth to be $\bar{U}_{trap} = h \times 15.5\,\mathrm{MHz}$ with a relative standard deviation of 9% among the tweezers. The largest shift exceeds the mean by 12% and the smallest shift is 18% below the mean. This error is consistent with possible alignment errors of the trap beam on the SLM and possible aberrations which are not accounted for in the compensation pattern.

Parametric Heating Measurement

To measure the trap frequency a so-called parametric heating measurement was performed [76]. For this the power of the tweezers was periodically modulated with different frequencies. When the modulation frequency hits twice the trap frequency a strong heating effect can be observed. A rigorous derivation is carried out for example in reference [45, 46]. The sequence used to measure this effect again begins with the sequence described in subsection 3.6.1. After that a function generator is triggered to add a sinusoidal modulation onto the trap beam intensity. This is done by exploiting the AOM used for the intensity stabilization. The modulation is kept on for 75 ms. Afterwards the chopping is turned off and to increase the contrast of this measurement the trap light power is rapidly switched to 7.5% of its original value and slowly ramped up again to 25% within 5 ms. This allows atoms, which where subject to parametric heating but did not quite make it to escape during the modulation phase, to also escape their traps. Note that this also allows to decrease the modulation time and to probe predominantly the harmonic region of the trap. After this the chopping of the trap is turned back on and another picture is taken.
The results of this measurement are shown in Figure 3.13. In subfigure (a) the modulation spectrum of a single trap is shown. One can clearly see three separated peaks. The lowest in frequency is attributed to the axial direction while the other ones are to be ascribed to the radial directions. The spectra of all the traps are shown in Figure A.2. The two separated peaks for the radial directions could not always be resolved but the fact that the radial axis are resolvable in some measurements hints towards significant aberrations in our system. In the subfigure (b) the radial trap frequencies, which are the halved resonance frequencies, are shown. From the measurement on the trap depth and the diffraction limit of the objective one would expect a trapping frequency

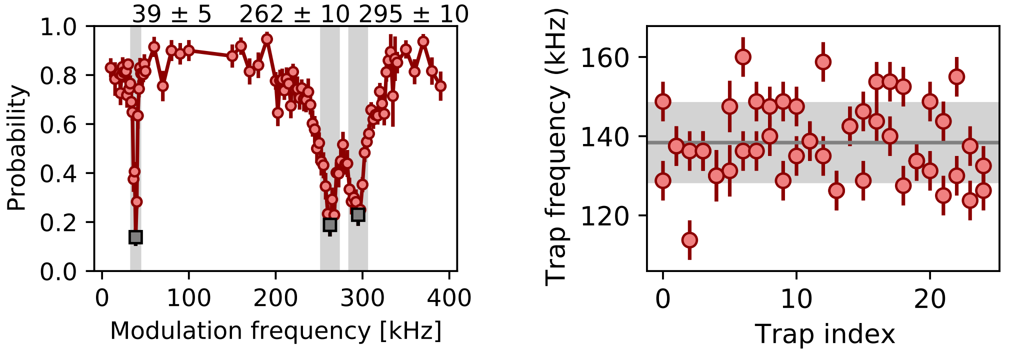

(a) Modulation spectrum (b) Radial trap frequencies

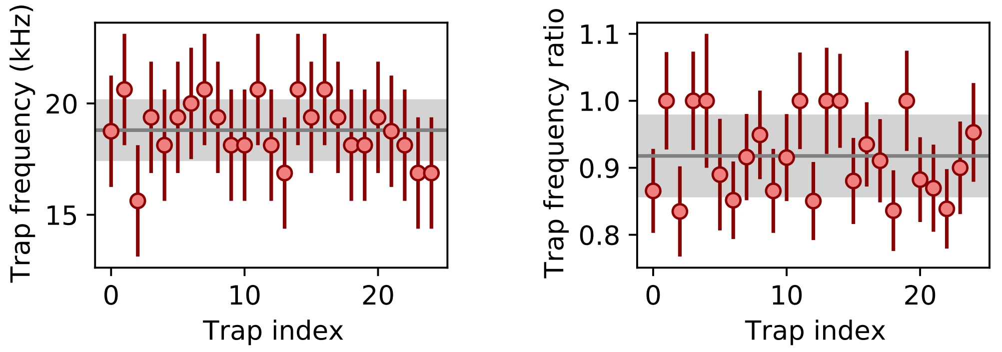

(c) Axial trap frequencies (d) Ratio of the radial trap frequencies

Figure 3.13 – Parametric heating spectroscopy. The results of a modulation spectroscopy for a rectangular 5×5 pattern with 5 µm lattice constant. (a) A typical parametric heating spectrum of a single trap. Shown is the measured probability for a trapped atom to survive the modulation at different frequencies (circles). The red line connecting the points is a guide to the eye. The lowest measured points in the resonance dips are taken to be the resonance frequencies (squares). On this a conservative hand adjusted confidence interval is assumed (light gray regions). On top of the graph the extracted resonance frequencies are shown. (b) The radial trap frequencies are extracted by taking the higher two resonances for each trap halved (circles). The mean of $\bar{\omega}_r = 2\pi \times 138(2)\,\text{kHz}$ is indicated by a gray line. The standard deviation around that mean of $2\pi \times 10(2)\,\text{kHz}$ is indicated as a horizontal light gray bar. (c) Same as (b) but for the axial direction. The mean is found to be $\bar{\omega}_z = 2\pi \times 19(1)\,\text{kHz}$ and the standard deviation among the tweezers is $2\pi \times 1\,\text{kHz}$. (d) The ratio of the two radial trapping frequencies is shown in the same way as the trapping frequencies. The mean of it is calculated to be 0.9 and its standard deviation among the tweezers is 0.1. Note that all values are below one because it is not possible to distinguish the axes of the traps in the measurement. Therefore the smaller value is always divided by the bigger one. Note also that when not two upper resonances where resolved in the measurement the frequencies were taken to be equal.

of

$$\omega_r^{ideal} = 2\pi \times 253\,\text{kHz}.$$

Compared with the mean measured trapping frequency of

$$\bar{\omega}_r = 2\pi \times 138\,\text{kHz}$$

and the maximal measured trap frequency of

$$\omega_r^{max} = 2\pi \times 160\,\text{kHz}$$

there is a significant deviation which can probably also be attributed to aberrations. Note that the comparison to the highest trap frequency is meaningful as the ideal frequency is an upper bound, which can not be exceeded.
From formula 2.5 we find that

$$\frac{\omega_z^{ideal}}{\omega_r^{ideal}} = \frac{\lambda}{\pi w_0 \sqrt{2}} \approx 0.22$$

which also deviates from the experimental value of $\bar{\omega}_z/\bar{\omega}_r = 0.14$, consistent with what one could expect from aberrations resulting in less tight focussing.

In-situ Thermometry

The temperature is rather unrelated to the trap geometry and depends more on the loading and imaging procedure. Nonetheless it can provide important insights into the loading and is important for temperature related effects like the Doppler shift which can lead to a decrease in the coherence time in Rydberg experiments.
In the case of a single atom in a trap the temperature T is related to the statistical distribution of the population $p(E_n)$ of the motional energy levels by the Boltzmann distribution.

$$p(E_n) = \frac{1}{Z} e^{-\frac{E_n}{k_B T}}$$

where Z is chosen to normalize the probability distribution. To measure the temperature of the atoms in the trap one needs to probe this distribution by some means. To this end the following method was applied. Starting with atoms in some thermal state in the trap the potential is then suddenly switched down to a fraction of its initial depth. The switching needs to be faster then the inverse trap frequency to make this process diabatic. After this the populations of levels with energies exceeding the new trap depth are mapped to the unbound continuum. Only atoms which were occupying energy levels below this value remain trapped. With that the loss statistics after such a sudden change is fully determined by the population distribution among the energy levels before it. One can probe the full distribution by switching to different trap depths in subsequent experimental runs.
We can derive a simple model for loss probability p_{loss} depending on the trap depth

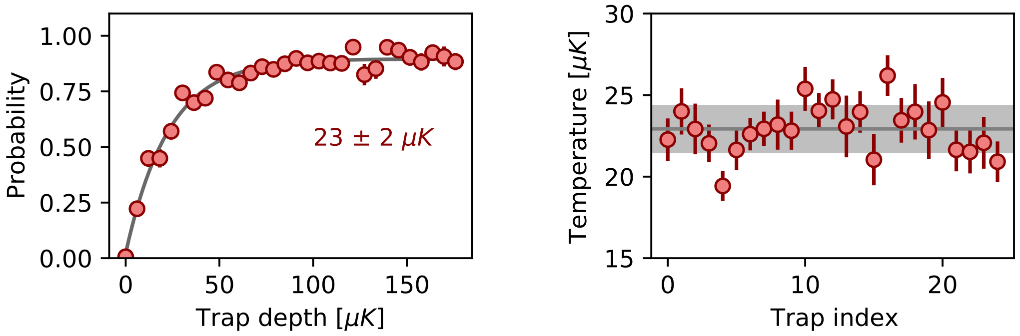

(a) Thermometry on single trap (b) Temperatures of all traps

Figure 3.14 – Thermometric in-situ measurement. The result of the temperature measurement procedure introduced in the main text. (a) The experimental results (circles) obtained on a single trap. The survival probability is plottet against the trap depth after the rapid switch down of the traps. The model developed in the main text is fitted to this data (solid line). The so obtained temperature is written next to the graph. The statistical error bars are mostly smaller then the marker. The error on the temperature is extracted from the fitting error. (b) The temperature of all traps is shown (circles) and the mean is indicated by a gray line and found to be $T_{mean} = 23\,\mu\text{K}$. The light gray region shows the standard deviation of $\Delta T_{mean} = 1\,\mu\text{K}$.

E_{probe} after the sudden switch. By means of a simple integration we find

$$p_{loss}(E_{probe}) = 1 - \frac{1}{Z}\int_{E_0}^{E_{prob}} e^{-\frac{E}{k_B T}} dE = 1 + \frac{k_B T}{Z}\left(e^{-\frac{E_0}{k_B T}} - e^{-\frac{E_{prob}}{k_B T}}\right)$$

where E_0 is the initial trap depth. Here the spectrum was assumed to be continuous, which is justified as deviations from this can be absorbed in Z which is a fitting parameter of the model.

To experimentally probe p_{loss} the following sequence was used. Starting with the loading sequence of subsection 3.6.1 the traps are rapidly switched to a fraction of its initial depth while still maintaining the chopping. After 1 ms holding time at this value the trap depth is ramped up again to its initial value within 5 ms. 45 ms afterwards the second picture is taken. This is done for different fractions of the lowered trap depth.

The results obtained are shown in Figure 3.14 and Figure A.3 . The absolute trap depth is taken from the light shift measurement of section 3.6.2 which was done on the same pattern. The function fitted to the data is given as

$$p_{fit}(E_{prob}) = a_{off} + a_Z e^{-\frac{E_{prob}}{a_T}}$$

where a_{off}, a_Z and a_T are fitting parameters. The temperature is extracted using $T = {}^{a_T}/_{k_B}$. Note that this fitting parameter is largely decoupled from systematic errors. The so found mean temperature is $T_{mean} = 23\,\mu\mathrm{K}$. This is clearly below the Doppler limit on the D-lines and comparable to another state-of-the-art quantum gas experiment with a comparable cooling sequence for Potassium [77].

3.6.3 A Talbot-like Effect

One degree of freedom which is challenging to control in the experiment is the intensity pattern away from the trap plane. It is known that intensity patterns consisting of sports arranged in a rectangular periodic structure replicate themselves after a propagation distance of $z_T = 2a^2/\lambda$, with a being the patterns periode. For fractions of this distance fractional replications of the pattern build up. This effect was first observed by Talbot and later theoretically explained by Rayleigh [78]. It can be generalized to the claim that periodic arrays of spots reproduce themselves after a certain near field distance. Today the Talbot effect still attracts considerable attention and schemes to produce exotic lattice geometries for ultra cold atom experiments based on it have been proposed [79]. In [80] it has been observed and utilized for the realization of large-scale multi layer systems in the context of single atom tweezers. In the here presented experiment we can not expect the Talbot effect to appear in such a clean form, as the random relative phases of the light field in the tweezers break the required periodicity. Nonetheless we will see in the next section by means of a simulation that indeed also in that case considerable intensity maxima build up outside the tweezers plane at a near field distance, which are potentially strong enough to trap atoms. After this analysis we will turn to an experiment carried out to verify if atom trapping outside the tweezers plane can be observed.

Calculation of Light Intensity Distribution in Axial Direction

To check for the other intensity maxima in the axial direction one has to find a method to propagate the light field to an arbitrary plane in the propagation direction of the light, here chosen to be the z axis. This can be achieved by means of the propagation of the angular spectrum of the light field in some plane perpendicular to the propagation direction [81]. The angular spectrum associated to the light field $U_z(x,y)$ in the plane at position z is given as

$$A_z({}^{a}/_{\lambda}, {}^{b}/_{\lambda}) = \mathcal{FT}[U_z(x,y)]({}^{a}/_{\lambda}, {}^{b}/_{\lambda}).$$

From requiring that $U_z(x,y)$ fulfills the Helmholtz equation $\Delta U_z(x,y) + k^2 U_z(x,y) = 0$ one finds that $A_z(a/\lambda, b/\lambda)$ has to satisfy

$$\frac{d^2}{dz^2} A_z({}^{a}/_{\lambda}, {}^{b}/_{\lambda}) + \left(\frac{2\pi}{\lambda}\right)^2 \cdot (1 - a^2 - b^2) \cdot A_z({}^{a}/_{\lambda}, {}^{b}/_{\lambda}) = 0.$$

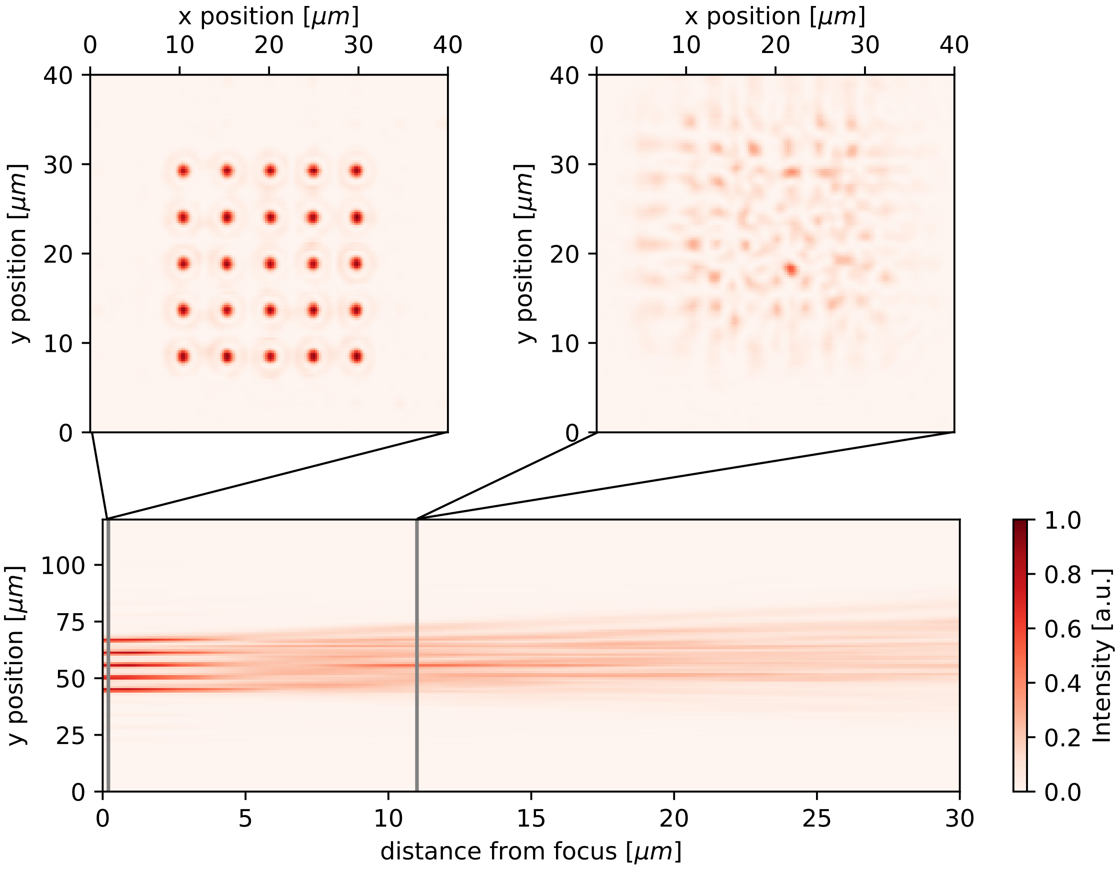

Figure 3.15 – Calculated intensity distribution along the vertical axis. In the lower picture the intensity distribution of a 5 by 5 pattern along a horizontal axis (y-axis) and the axis in light propagation direction (z-axis) is shown. The zero of the z-axis is the tweezers plane. Over the x-axis the maximum is taken. This makes it possible to identify potential intensity maxima away from the tweezers plane which can trap atoms. The first vertical line is placed at the tweezers plane and the horizontal intensity distribution is shown. The trap pattern is nicely visible. The second vertical line is placed where a potentially atom trapping maximum in the main picture is identified. In the associated picture above again the corresponding horizontal plane is shown. One can clearly see that a very localized spot appears here with 50% of the power of a desired tweezers.

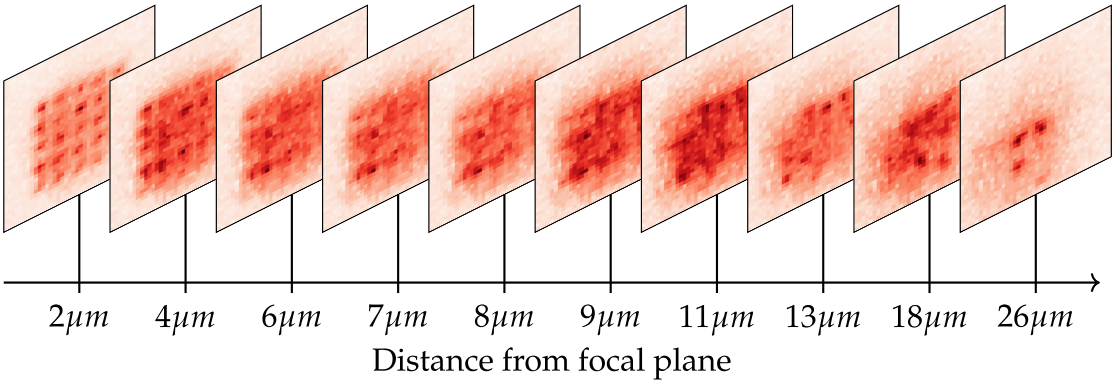

Figure 3.16 – Talbot-like effect in the Experiment. Shown are experimentally obtained averaged pictures of the atoms trapped by the SLM beam. The axial position of the traps was changed using the Fresnel lens pattern on the SLM. Thereby effectively the imaging plane is shifted relative to the trap plane. With that it was possible to scan for planes outside the tweezers plane which trap atoms. Indeed a very localized signal at 26 µm away from the trap plane is a clear indication that atoms are trapped also in this plane.

An elementary solution can be found to be

$$A_z({}^a\!/\!_\lambda, {}^b\!/\!_\lambda) = A_0({}^a\!/\!_\lambda, {}^b\!/\!_\lambda) \cdot \exp\left(i\frac{2\pi}{\lambda}\sqrt{1-a^2-b^2}z \right).$$

With that a way which is easy and cost efficient to implement on a computer is found. Starting from an light field in one plane one takes the Fourier transformation to find the corresponding angular spectrum, multiplies it by $H_z^{freespace}(a,b) = \exp(i2\pi\sqrt{1-a^2-b^2}z/\lambda)$ and takes the inverse Fourier transformation.
Our goal is to calculate the whole intensity distribution around the tweezers plane for a calculated phase pattern on the SLM. Therefore the second ingredient one needs is the lens which focuses the beam down. In the thin lens approximation the propagation of the light through a lens is assumed to just result in a local phase shift in the plane of the lens. This is modeled by multiplying the light field by

$$H_f^{lens}(x,y) = \exp\left(i\frac{2\pi}{\lambda}(x^2+y^2)\frac{1}{2f} \right)$$

where f is the focal length. To calculate the intensity distribution around the focus of the lens both manipulations are subsequently applied. The results for a phase pattern associated to a 5×5 rectangular lattice with a lattice constant of $5\mu m$ are shown in Figure 3.15. From this, one sees that indeed the regular structures expected from the Talbot effect do not show up, but still significant intensity maxima outside the trap plane can appear at distances which do not only disturb the imaging but might also effect the Rydberg mediated interactions in the trap plane.

Experimental Observation of the Talbot-like Effect

The flexibility of the SLM allows to directly observe trapping of atoms out of the plane. For this the usual sequence to load and image atoms described in subsection 3.6.1 was used. To scan different distances from the trap plane a Fresnel lens pattern with varying focal length was superimposed on the SLM. The focal lengths of the Fresnel lens was of several meters and therefore well in the range where the pixelation of the SLM can be neglected. The results of this measurement are shown in Figure 3.16. One can clearly see that the signal from atoms trapped in the trap plane washes out after a view µm. After some more distance localized signals seem to appear again and at a distance of 26 µm three clearly localized signals can be identified. This distance lies in the same order of magnitude as the Talbot distance of $\approx 50\,\mu\text{m}$ for this pattern. The signal can also not be attributed to light scattered by atoms trapped in the shifted trap plane, as the scattered light is incoherent and can not interfere to such well localized spots away from the focus. This leads to the conclusion that this is a signal from atoms which are trapped outside the intended trap plane.

While the measurement provides clear evidence that at 26 µm atoms are trapped with a high probability also some features in the planes in between shown in Figure 3.16 might be due to atoms trapped there with a low probability. This trapping in only a few Rayleigh ranges $z_r \approx 4\,\mu\text{m}$ away from the tweezers plane results in a significant background signal in the imaging. While for 5 µm spacing trapped atoms can still be identified at 3 µm inter-trap spacing the signal from trapped atoms can not be distinguished any more from the background.

3.7 Conclusion and Outlook

In this chapter the implementation of arbitrarily arranged tightly confining optical dipole traps was discussed. The setup as well as the algorithmic implementation of an SLM based setup to generate the traps was presented and experimental results were obtained and analyzed. From this it is evident that the loading of atoms into the array works with the expected fidelity. However, the in-situ measurements carried out to obtain the trap parameters show strong signs of residual inhomogeneities and aberrations in the tweezers arrays. The homogeneity problem can to a large extend be overcome with the implementation of a feedback loop from the experiment or a camera imaging the traps to the Gerchberg-Saxton algorithm. The compensation of aberrations was demonstrated and in subsection 5.3.2 a method for characterizing the aberrations using light shift measurements on trapped atoms will be discussed.

It was furthermore demonstrated, that atoms get trapped out of plane. This leads to a serious imaging problems for small spaced two dimensional tweezers arrays and needs to be overcome in the future. Promising approaches involve the loading from an elliptical dipole trap or light sheet or the use of a resonant push out technique. Another option involves the use of an AOD, which will be presented in subsection 5.3.5.

It is worth mentioning, that during the work on this project also a Raman-sideband cooling scheme for the traps was successfully implemented and the setup is in use to probe interactions between Rydberg atoms.

Deterministic Loading of Dipole Traps

In this chapter we will take a closer look at light assisted collisions in the dipole traps. In the previous experiments we were only concerned with the specific properties of the single traps. They where carried out by loading some number of atoms and using red detuned light assisted collisions to project this distribution of loaded atoms to the subspace of only having none or a single atom loaded. The procedure fundamentally limited the probability to find a single atom in a trap to $\approx 50\%$. As already mentioned in the introduction, a crucial requirement for a quantum simulator is a non-exponential resource scaling when adding more degrees of freedom to the simulated quantum system. For the quantum simulator under consideration here, adding a degree of freedom means adding a trap with an atom loaded. When each new trap only loads in every second run, the time resources scale exponentially in a fashion comparable to the resource scaling of quantum simulations on classical computers. Therefore one would not expect that this approach could significantly outperform classical simulations. Note that any loading probability away from unity leads to an exponential resource scaling making this an achilles' heel of the present approach. It is crucial to find a way to increase the loading probability. One possibility is the use of blue detuned light assisted collisions. While the kinetic energy gain in red detuned light assisted collisions almost always suffices to expel both atoms from the trap the kinetic energy gain in blue detuned light assisted collisions is in principle tunable and can be adjusted such that only one atom leaves while the other one remains in the trap. This has been realized in several systems [82–84].

In the following, first an introduction to light assisted collision of two particles in free space is provided. Then some characteristic numbers are given taking the experimental parameters into account. Finally experimental results are presented.

4.1 Two Colliding Atoms

The profound question on how two atoms interact attracted a lot of attention in the past and led to a very involved theoretical framework. Fortunately, the regime of interest in the present analysis allows for some significant simplifications. First, we assume that the inter-atomic distance R is smaller then the wavelength of any transition involved in the interaction. That justifies to neglect retardation effects. Secondly, we assume R to be larger then the Le Roy radius $R_{LR} = 2(r_1 + r_2)$, with $r_i = \sqrt{\langle n_i J_i F_i | \hat{r}^2 | n_i J_i F_i \rangle}$ the size of the atom i [41]. This allows to treat the atoms as well-separated charge distributions coupled via electrostatic interaction, without electronic exchange interactions. Furthermore, this allows to treat the interaction with a multipole expansion

$$H_{int}(R) = \sum_n \frac{C_n}{R^n}$$

with C_n coefficients to be determined. For two colliding alkali atoms in the ground state the interaction is dominated at large inter atomic distances by the C_6 term in the expansion. This is known as the van-der-Waals interaction. It is connected to the single atom polarizability α by means of the Casimir-Polder integral [85]

$$C_6 = \frac{3}{\pi(4\pi\epsilon_0)^2} \int_0^\infty d\omega[\alpha(i\omega)]^2$$

where $\alpha(i\omega)$ is the polarizability of a state $|v\rangle$ at a complex frequency given by the expression

$$\alpha(i\omega) = \frac{2}{3} \sum_{k \neq v} \frac{E_k - E_v}{(E_k - E_v)^2 + \hbar^2\omega^2} |\langle v| \hat{\mathbf{d}} |k\rangle|^2$$

where E_i is the energy of the atomic state $|i\rangle$ and the sum runs over all states except v. Intuitively the van-der-Waals interaction arises due to the coupling of the induced dipole momenta of both atoms in the form of a second order dipole-dipole process and is in relation to the Casimir effect [86, 87].

A different situation emerges when two atoms a and b are considered, of which one is excited to a P-state. In this case, for large inter atomic distances the van-der-Waals term is dominated by a resonant dipole-dipole interaction captured by the C_3 coefficient. Intuitively the two atoms start to exchange virtual photons along the inter atomic axis which leads to a back and forth swapping of the excitation. Loosely speaking, the new eigenstates of this system can be thought of as each atom being dressed by the virtual exchange light field and this dressing depends on the dipole coupling strength to the virtual light field and the inter-atomic distance.

As the polarizabilities as well as the level structure of atoms are only accurately captured in the framework of quantum mechanics, it is reasonable to treat also the interaction in a quantum mechanical fashion. The electro-static interaction Hamiltonian H_{int} takes the form [88]

$$H_{int} = \frac{1}{4\pi\epsilon_0} \frac{\hat{\mathbf{d}}_a \cdot \hat{\mathbf{d}}_b - 3\hat{d}_{az'}\hat{d}_{bz'}}{R^3}$$

where $\hat{\mathbf{d}}_{a/b}$ is the full vectorial dipole operator acting on atom a or b respectively and $\hat{d}_{az'/bz'}$ the projected dipole operator on the inter-atomic axis z'. By the symmetry of the individual atomic Hamiltonians we are free to choose their angular quantization axis along z'. The electronic wave function of both atoms is then expressed by

$$|l_a\lambda_a, l_b\lambda_b\rangle = |l_a\lambda_a\rangle\, |l_b\lambda_b\rangle$$

where $l_{a/b}$ are the respective angular momenta of the electronic wave function and $\lambda_{a/b}$ the corresponding projections on the z' axis. As the interaction Hamiltonian has a cylindrical symmetry along this axis, the resulting quantum numbers of this quantization axis choice are also good quantum numbers in the coupled problem. On this basis one finds that

$$H_{int}\,|00,1\lambda_b\rangle \propto |1\lambda_b,00\rangle$$

which allows to identify the eigenvectors and therefore the eigenvalues, which are [89]

$$C_3^{\Pi\pm} = \pm\frac{1}{4\pi\epsilon_0}|\,\langle 10|\,d_{bz'}\,|00\rangle\,|^2 = \pm C_3'$$

and

$$C_3^{\Sigma\pm} = \pm\frac{2}{4\pi\epsilon_0}|\,\langle 10|\,d_{bz'}\,|00\rangle\,|^2 = \pm 2C_3'$$

where the superscript symbols of C_3 label the states. The capital greek letters are inspired by the common labeling of the potentials in the Hund's case (a), to which the individual potential curves are connected to. It was used, that both atoms are interchangeable to state this in terms of single atom properties. These eigenvalues of the interaction give the adiabatic potential curves in Born-Oppenheimer approximation. The single atom transition amplitude appearing in the expressions also appears in the decay rate Γ of the P state. Using this we find the useful relation

$$C_3' = \frac{3\hbar c^3}{4\omega^3}\Gamma.$$

Many lifetimesu in alkali atoms are measured using this relation. The C_3 coefficients can be very precisely determined by means of photo association spectroscopy, which is supported by a well developed theory.

For the particular configuration of two colliding Potassium-39 atoms the multipole coefficients are experimentally determined to be $C_3' = \hbar \cdot 51.68(7)\,\text{kHz}\,\mu\text{m}^3$ for P-S-state collisions [90] and $C_6 = \hbar \cdot 0.567\,\mu\text{Hz}\,\mu\text{m}^3$ for S-S-state collisions [91]. This justifies to neglect the ground state van-der-Waals potential for the light assisted collisions treated hereafter.

4.2 Light Assisted Collisions

In the previous section we derived the shape of the potential curves of two atoms at a distance R for the cases of both atoms being in the S-state and for one atom being excited to a P-state. Under the conditions, present in the experiments carried out here, the two atoms colliding can always be considered to be asymptotically, meaning at $R \rightarrow \infty$, in the S-state. However, if two colliding ground state atoms encounter a detuned optical field, the probability to get excited to a state where one atom is asymptotically in a P-state, peaks around the Condon point R_c. At this distance the light field frequency matches the difference in the potential curves. When the two atoms are approaching each other this coupling give raise to a Landau-Zener-transition to the excited state branch. This is reversed when the constituents of the collision move apart again. While the atoms are in the excited branch they experience large attractive or repulsive forces determined by the sign of the C_3/R^3 potentials and acquire kinetic

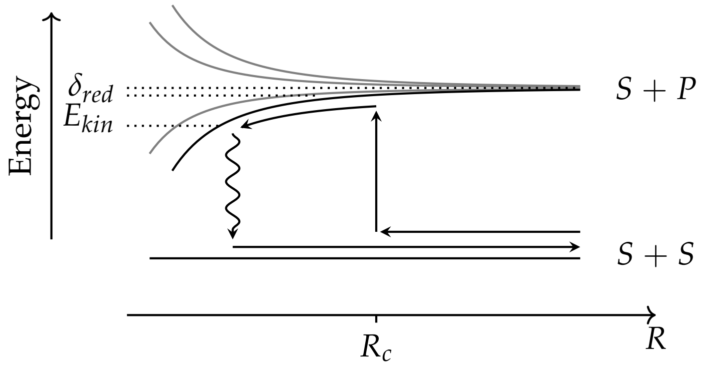

Figure 4.1 – Red-detuned light assisted collision. The schematic model of red-detuned light assisted collisions. In black the involved Born-Oppenheimer potentials are shown while the potential curves not involved are shown in gray. On the right the asymptotic uncoupled states are shown. δ_{red} denotes the detuning of the external laser from the free space line. When two ground state atoms are approaching, the curves are brought to resonance with the light at $R = R_c$ and the two atom system is transferred to the excited potential curve. The attractive molecular potential lets the atoms accelerate towards each other and on a spontaneous decay event to the ground sate E_{kin} is realized as gained kinetic energy in that inelastic collision.

energy which, in the case of a spontaneous decay to the ground state, is realized as kinetic energy of the atoms after the collision. Already in the early days of cooling and trapping atoms by optical means this loss process was identified to be a limiting factor [92].
In the following we will separately discuss the two distinct cases of red- and blue-detuned light encountered in the collision.

4.2.1 Red Detuned Collisions

The situation of two atoms colliding in the presence of a red-detuned light field is illustrated in Figure 4.1. The atoms approach each other until the Condon point is reached. At this point the originally free collision can be photoexcited by means of a Landau-Zener transition to a molecular dimer. Note that the excitation to discrete molecular states leads to resonances which need to be taken into account in a proper treatment of this process [93]. Here, we are only interested in its qualitative nature and will therefore ignore the discretized nature of the excited dimer states. After some time $T_{coupled}$ the atoms, after they have traversed the molecular potential, can be thought of as passing the Condon point again and being dissociated. As the coupling processes are happening at the same Condon point and the final state asymptote is the same as for the initial state of the collision, this collision is elastic. On the temperature scales of cold atom experiments $T_{coupled}$ becomes much longer then the decay rate of the excited state and a spontaneous decay with a photon, lower in energy then the previously absorbed one, can lead to a large gain of kinetic energy for both atoms. In the context of the atom trapping, as carried out in this work, this leads to a high probability of both atoms to leave the trap after the collision. In the previous chapter this process was exploited for the parity projection, which limited the loading probability of a single atom to 50%.

In a real alkali atom the level structure is much richer and several other mechanisms like predissociation or interference of multiple Condon points from cooling and repumping light might occure but the qualitative expectation is not altered by that.

4.2.2 Blue Detuned Collisions

On the blue detuned side of the resonance much better control over the collision process can be expected. Because the branch to which the two atoms are excited is repulsive the turning point is close to the Condon point and the constituents stay at distances above the Le Roy radius, which makes the dynamics well predictable. Furthermore, it is possible to experimentally control the upper bound of the kinetic energy gained during the collision. This blue detuned collision can even be exploited in a mechanism called blue shielding to almost eliminate the above described red-detuned light assisted losses [94].

In Figure 4.2 the blue detuned collision process is depicted. Again the atoms in the ground state pass the Condon point and are excited to the repulsive branch in a Landau-Zener like transition. After some time they pass the Condon point again. In doing so they either get deexcited and leave the collision elastically in the $S + S$ asymptote or they stay in the excited branch and decay at some later point. The former case is the desired one in the concept of blue shielding. By placing the Condon point of blue-detuned light before a red-detuned Condon point can be reached, colliding atoms are prevented from ever seeing the red-detuned Condon point. In the later case the collision is inelastic and the atoms gain an amount of kinetic energy which is bounded from above by the detuning to the transition. This allows to control the energy gain of the atoms in the collision and therefore provides a handle for trap losses. The following will focus on this process.

The applicability of a simple Landau-Zener approach depends on three time scales [89]: (1) the spontaneous decay time τ_γ (2) the time it takes a wavepacket to travel from the Condon point to the turning point $\tau_{tp} \approx \mu v/\alpha$, where μ is the effective mass, v the velocity and α the slope of the difference potential at the Condon point. (3) the time it takes the wavepacket to traverse half the Landau-Zener interaction region $\tau_\Omega \approx \hbar\Omega/2\alpha v$, where Ω is the coupling at R_C. When τ_γ is large compared to τ_{tp} and τ_Ω the process is well described by passing a Landau-Zener region twice without modifications. The probability to leave the collision in the $S + P$ asymptote is then given by

$$P_e = (1 - P_D)P_D$$

where P_D is the probability to diabatically cross the Landau-Zener region:

$$P_D = \exp(-4\pi\tau_\Omega\Omega).$$

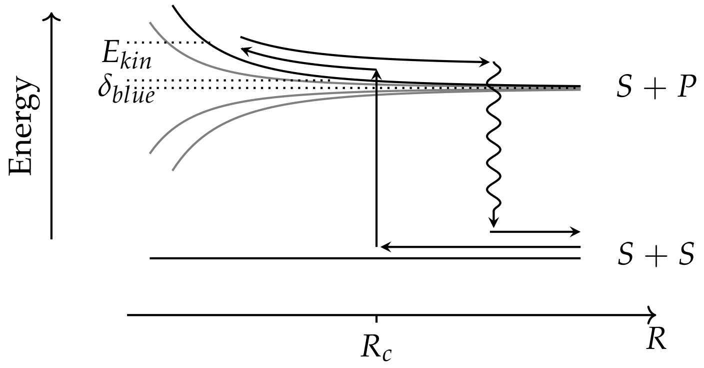

(a) Born-Oppenheimer potential curves

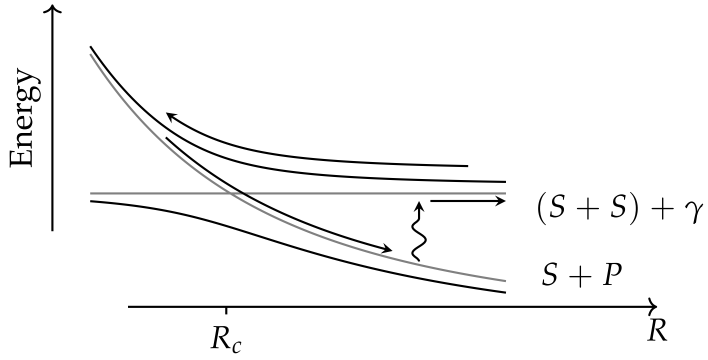

(b) Dressed state picture

Figure 4.2 – Blue-detuned light assisted collisions. (a) Illustrated are the Born-Oppenheimer potential curves of two approaching atoms. In the presence of blue-detuned light two atoms in there respective ground state approaching each other are shifted to resonance to the repulsive collision branch at $R = R_c$ of the asymptotic $S + P$ state.The two atom system is excited to that branch and the travel along this curve until they reach the turning point determined by their relative kinetic energy. Traveling back on this potential curve they pass the Condon point R_c again. There they are either transferred back to the ground state branch in a adiabatic fashion or they are diabatically passing the Condon point and stay in the excited state. After a while they spontaneously decay to the ground state. The former process describes the blue shielding while the later is the process allowing for a controlled maximal kinetic energy of $h \times \delta_{blue}$ which is exploited in the deterministic loading. (b) The same process as in (a) but in a dressed state picture. The gray curves are the Born-Oppenheimer curves with the absorbed photon γ taken into account. In black are the adiabatic curves when both Born-Oppenheimer curves are coupled.

When τ_{tp} becomes comparable to τ_γ potential decays before entering the Landau-Zener region the second time need to be taken into account. This yields

$$P_e = (1 - P_D)\exp(-\tau_{tp}/\tau_\gamma)P_D. \tag{4.1}$$

When τ_γ becomes of the order of τ_Ω the simple Landau-Zener approach is expected to fail. However, in [95] this regime was investigated using quantum Monte-Carlo simulations and the so-called Landau-Zener model with delayed decay was found to reproduce the results. This justifies the following modification of Equation 4.1.

$$P_e = (1 - P_D)\exp(-(\tau_{tp} - \tau_\Omega)/\tau_\gamma)P_D \tag{4.2}$$

4.2.3 Deterministic Trap Loading

The above described control over the inelastic collision of two atoms encountering blue detuned light can be utilized to outperform the 50% limit imposed by red detuned light assisted collisions. The detuning is tuned such that in each collision only kinetic energy on the order of the trap depth can be gained. By that the energy is just enough that one atom can leave the trap while the other one remains trapped. This procedure had proven to increase the atom loading probability in a single trap to up to 91% with Rubidium-85 [96] and in trap arrays to 80% in Rubidium-87 experiments [97].e However, there are some caveats to this simple picture. First note that $P_D > P_e$, meaning that if one uses the blue light assisted collisions for controlled ejection from the trap, one can not fully rely on the same light for blue shielding. The probability to diabatically stay in the S+S asymptotic state and being subject to a red detuned light assisted collision is similar to P_e. This would impose a new upper limit on the loading efficiency clearly below 100% and depending on the red detuned light. Therefore, it is still undesirable to have red-detuned light on while using the above described procedure. Another complexity arises from the fact that the atoms are not in the motional ground state when they collide but are in thermal motion. When the energy of the constituents of a collision is above half the trap depth again both atoms can be lost from the trap. This means that deep traps are favorable, as the ratio of atom temperature to trap depth is to be minimized.

4.3 Enhance Loading Experiment

In this section the application of the above described method is adapted for the present experimental apparatus. The idea is to use the gray molasses for cooling and deterministic loading at the same time as done in [97].

4.3.1 Gray Molasses Cooling in the Traps

To take full advantage of the blue detuned light assisted collisions already in the loading process any red detuned light needs to be eliminated. Therefore the cooling into the tweezers needs to be done with the gray molasses. To test this cooling the following experiment was carried out: After loading the atoms with the sequence introduced in subsection 3.6.1 60 µW resonant light on the D2-line was shown to the atoms for 30 ms. With this the atoms were heated by a well controlled amount. Using the same thermometry as carried out in section 3.6.2 we found the temperature after the heating pulse to be ≈ 85 µK. To deduce the cooling rate a pulse of gray molasses light

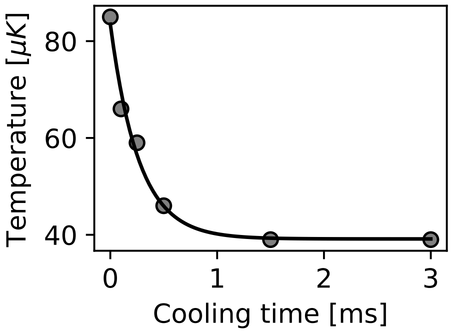

Figure 4.3 – Gray molasses in-trap cooling rate. The temperature after a defined time of cooling with the gray molasses. The atoms in the traps were intentionally heated before the cooling was applied. An exponential decay was fitted which yields a 1/e-time of $\approx$ 0.3 ms and a steady state temperature of $\approx$ 40 µK.

of variable length and tuned to the expected working region with the trap light shift taken into account was applied. While the gray molasses cooling the chopping of the traps was switched off.
The results of this measurement are shown in Figure 4.3. From the fit and the assumption of a cooling rate linearly depending on the temperature one finds $\gamma_{cool}(T) \approx T \cdot 4\,\mathrm{ms}^{-1}$ and a heating rate of $\gamma_{heat} \approx 150\,\mu\mathrm{K\,ms}^{-1}$. Note that all the measurements were again done on a 5×5 trap array with the same powers in the traps as in the measurements of the previous chapter. With this it is shown that the gray molasses indeed cools inside the traps.

4.3.2 Collision Parameter Estimates

To determine in which regime and with which probability one can expect the blue detuned light assisted collisions to happen the parameters introduced in section subsection 4.2.2 are to be estimated. The spontaneous decay lifetime can be assumed to be the same as for the free space decay $\tau_\gamma \approx 26\,\mathrm{ns}$. To calculate τ_{tp}, the mean velocity at which the particles approach each other is to be calculated from the temperature of the particles in the trap. The actual temperature during the loading process is hard to determine experimentally. We therefore assume the lower bound on this temperature given by the steady state temperature measured in the previous section. By using the Viral theorem and the mean velocity of a thermal Boltzmann distribution one finds $v_{th}(40\,\mu\mathrm{K}) = 0.2\,\mathrm{m\,s}^{-1}$. By assuming the detuning of the gray molasses lasers to be the trap depth measured in section 3.6.2 one finds that $\alpha \approx 250\,\mathrm{kHz\,nm}^{-1}$. From this $\tau_{tp} \approx 30\,\mathrm{ns}$. With a Rabi frequency of $\Omega \approx 0.7\,\mathrm{GHz}$ one finds $\tau_\Omega \approx 1\,\mu\mathrm{s}$. With this hierarchy of timescales we are in the regime where Equation 4.2 applies. However, the $P_D \approx 1$ to a very high accuracy, which spoils the above described deterministic loading process. Instead another process is expected to become dominant for the inelastic collisions. The approaching ground state atoms pass R_c region for the first time and decay to the ground state branch afterwards. Then they approach the Condon point

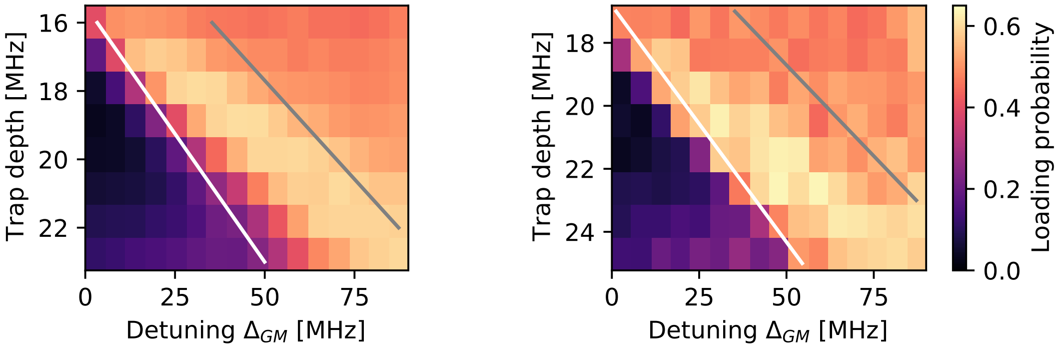

(a) Averaged over traps

(b) Single trap

Figure 4.4 – Gray molasses loading. Loading probability for loading from the gray molasses dependent on the trap depth and the detuning of the gray molasses Δ_{GM}. The white solid line indicates where Δ_{GM} is the sum of trap depth and light shifts of upper and lower states. It therefore indicates where the maximal kinetic energy gain in a collision is the trap depth. The gray solid line indicates were the maximal kinetic energy gain is twice the trap depth. (a) Shows the averaged loading probability over all traps in the 5×5 array. (b) Shows the results of a single trap in the array. The results of all the individual traps are shown in Figure A.4

again coming from $R < R_c$ and get excited again to the repulsive $S + P$-branch. A spontaneous decay then realizes the kinetic energy given by the blue detuning. In this process a similar control over the kinetic energy gain can be expected.

4.3.3 The Experimental Sequence

In order to only have the blue detuned gray molasses light on while the traps are loading the sequence presented in subsection 3.6.1 was changed as follows: After the gray molasses cooling the MOT lasers are switched on again with parameters to realize a red molasses, which helps to keep the atoms in place. While the red molasses is on, the gray molasses beams are switched of and ramped to the detuning desired for the deterministic loading. This takes 25 ms. Subsequently the MOT beams are switched off and the gray molasses beams are switched on again together with the trap array. After 30 ms of loading the tweezer in that configuration, the gray molasses lasers are switched off again. To probe the single atom loading fidelity a pulse of red detuned parity projection is shown to the traps for 20 ms. In case of a properly working single atom loading from the gray molasses, this should not have an effect and the loading probability remains over the parity projection limit.

4.3.4 Results and Discussion

This sequence is used to scan the trap depth and the detuning of the GM beams from the average trap depth of $U_{trap} = h \times 15.5\,\mathrm{MHz}$ to $U_{trap} = 1.5 \cdot h \times 15.5\,\mathrm{MHz}$. The detuning of the GM laser Δ_{GM} is scanned over a range of 90 MHz added to an offset of 90 MHz. The results as an average over all tweezers and of a single selected trap are shown in Figure 4.4.

First one notes that below the detuning corresponding to the limit where a single atom can be ejected, the loading probability is very low. In this region the fast atom from the collision can not escape and thermalizes again with the other atoms in the trap. This leads to a very pronounced heating which results in a loss of almost all atoms. On the other end, where the detuning is chosen such that the gained kinetic energy is enough to kick both atoms from the trap, one recovers the parity projection regime with a loading probability limit of $\approx 50\%$. Inbetween these limits one indeed sees an increase in loading probability exceeding this limit. The maximal average tweezers loading probability is 61% at $U_{trap} = h \times 18\,\mathrm{MHz}$ and $\Delta_{GM} = 42\,\mathrm{MHz}$. For the single tweezers shown in Figure 4.4 the peak loading probability is 64% at $U_{trap} = h \times 22.5\,\mathrm{MHz}$ and $\Delta_{GM} = 48\,\mathrm{MHz}$. The average loading value is expected to be smaller than the one from the single trap, as all the traps are unequal in power as found in the previous chapter. Therefore all the profiles of the mapped out loading probabilities are shifted and the average is subject to a slight blurring.

We attribute the fact that we do not reach the same values as reported previously to the strong light shift of the excited state of the D1-line in 1064 nm laser light. As the atoms thermally move around in the trap they experience different light shifts at different positions, which in the present case, is exaggerated by the strong light shift in the ${}^2P_{1/2}$ state. Consequently the atoms also collide in different positions in the traps and the chosen detuning for the deterministic loading suffers from broadening due to that. Assuming again an in-trap temperature of 40 µK one finds that this shift is about 7 MHz on average. Note however that the in-situ temperature during the process of ejecting atoms might be significantly higher, as the collisions inevitable yield another heating process. That shift smears out the region of proper working deterministic loading. In doing so, it reduces the peak loading probability.

4.4 Alternative: Deterministic Loading via Rydberg Blockade

An alternative approach, which recently came to our knowledge, utilizes the so called Rydberg blockade [23]. After initial loading of many atoms in the $F = 1$ ground state, an adiabatic passage involving a Rydberg state, as described in [83], can be performed. This induces a single $F = 2$ atom in the system. To understand this, we first assume a light field coupling the $F = 1$ ground states to a single Rydberg state. Each atom is then well-described by a two-level atom. Depending on the Rydberg state the interaction between Rydberg states effectively truncates the Hilbert space of the multiple two-level atoms within the so called Blockade radius to that of a single two-level system. The two states of the new system are described by all atoms in the $F = 1$ state and a state where a single Rydberg excitation is shared among all the atoms. This is known as a Rydberg super-atom. The effective coupling between these two states due to the light field is given by $\Omega_{super} = \sqrt{n}\Omega$, where n is the number of atoms in the blockade radius and Ω is the single atom coupling. Introducing now the $F = 2$ ground state and another light field, which couples this to the same Rydberg state, allows for the realization of Raman-π pulses. This has been realized in a similar manner in [98]. However, the $\sqrt{n}$ proportionality of the coupling makes the pulse dependent on the atom number, which is unwanted for a statistical number of loaded atoms. To overcome this, the above mentioned adiabatic passage scheme was proposed.

With the ability to deterministically transfere a single atom in each trap to the $F = 2$ state the only thing left to do is to get rid of all the other atoms. This can be achieved by using a tune-out wavelength or by light on a D-line resonant only to the $F = 1$ ground state.

4.5 Conclusion and Outlook

To overcome the very constraining limit of the party projection, we implemented a deterministic loading scheme which has been utilized in the past. Realizing that the gray molasses works in the same regime as needed for this scheme made the implementation of another beam path superfluous. An outperformance of the previous limit was indeed observed, but the disadvantageous light shifts in the excited states of the D-lines made a significant improvement impossible.

In order to reach higher loading probabilities multiple options exist. The obvious one is to choose another wavelength for the trapping with less severe light shifts. This will be elaborated on in the next chapter. Another option is to use a different transition which is less effected by the light shift. Here the transition to the 5P-state would be an option, as a laser system will soon be available to the setup. A third option is to use an adiabatic passage via a Rydberg state, which will also be investigated in the future.

CHAPTER 5

AOD-based Tweezers Arrays

In this chapter another method to generate tweezers arrays is described, which complements the existing SLM based platform. While the trap arrays generated by the SLM are difficult to be manipulated dynamically during the experimental sequence an AOD approach provides this flexibility. However, a platform solely based on an AOD is limited in other regards like the lack of aberration compensation, the limited realizable geometries and a fundamental limit on the minimal trap separation. How both techniques can be combined to compensate their individual weaknesses will be discussed in this chapter. First the working principle of the used AOD will be introduced. Then the planned extension to the existing experimental apparatus will be presented, followed by a discussion of the possibilities opened by this new setup.

5.1 Acousto-optic Deflector

The interaction between acoustic vibrations in a medium and light traversing this medium is known as the acousto-optic effect. The acoustic vibrations, which are by definition a dynamical strain in the system, modify the local refractive index of the material. These variations of the refractive index lead to reflections inside the crystal, similar to the reflections on the intersection of two materials of different refractive index [42]. In the case of an acousto-optical deflector a well controlled acoustical disturbance is introduced in the crystal by the use of a high frequency piezoelectric transducer. This allows for a controlled deflection of a single beam, traversing the crystal, into potentially multiple beams in an angular range given by the specific AOD used. In the following we will take a closer look at this mechanism.

5.1.1 Bragg Diffraction on Sound Waves

Considering an acoustic plane wave traversing the optical medium, the refractive index n of the medium is altered in a periodic fashion. The exact shape depends on the acoustic frequency f_{ac} and the characteristic speed of sound of the medium v_s. The local change of n is given by the following expression

$$\Delta n(x,t) = -\sqrt{\frac{1}{2}\mathcal{M} I_s} \cdot \cos(2\pi f_{ac}(t - x/v_s))$$

where x is the spatial coordinate parallel to the propagation direction of the sound wave and I_s is the acoustic intensity. M is a figure of merit for the strength of the

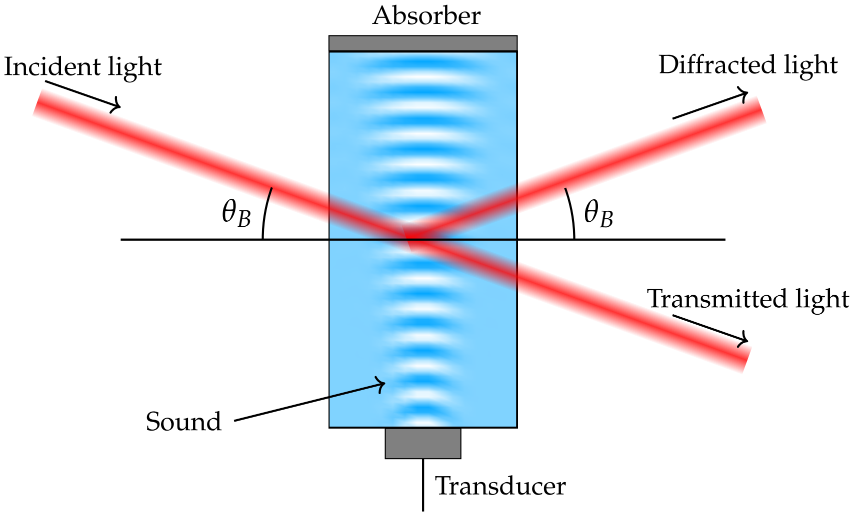

Figure 5.1 – Schematic diagram of an acousto-optic deflector. A transducer implements a traveling sound wave in an optical medium. The local refractive index depends on the strain of the material at that position and an incident light beam sees a periodic modulation of the refractive index induced by the sound wave. This leads to a diffraction under the Bragg angle θ_B. By tuning the frequency of the induced sound wave in the material, this angle can be changed in a limited range.

coupling between acoustic and optic waves in the material given by

$$\mathcal{M} = \frac{p^2 n^6}{\rho v_s^2}$$

with p a coefficient known as photoelastic constant and ρ the mass density of the medium.
This periodic modulation of the refractive index gives raise to the well-known effect of Bragg diffraction. A beam traveling through the medium experiences reflections at the wave fronts of the acoustic wave. When the beam is incident under an angle known as the Bragg angle θ_B all the reflections constructively interfere and give birth to a new diffracted plane wave which exits the crystal again under the angle θ. This is illustrated in Figure 5.1. From the constructive interference condition one finds the Bragg angle to be given by

$$\sin(\theta_B) = \frac{\lambda f_{ac}}{2 v_s}$$

where λ is the wavelength of the optical incident plane wave. For small sound intensities I_s, the diffracted optical intensity is directly proportional to I_s, while for higher I_s the efficiency of the diffraction saturates.

As the acoustic wave moves through the optical medium with v_s the diffraction is accompanied by a Doppler shift and the frequency of the diffracted light is shifted by the acoustic frequency f_{ac}.

5.1.2 Tricking the Bragg Condition

In order to use the acousto-optical effect, described in the previous section, to deflect an incoming beam at different angles the Bragg condition needs to be overcome. It imposes the condition on the incidence angle of the beam to be θ_B. This raises two difficulties. First an incident beam is a superposition of plane waves coming from different angles. In order to have a well-shaped diffracted beam all of these plane wave components must be diffracted, but only one exactly fulfills the Bragg condition. The second difficulty occurs when one wants to deflect the incident beam with an angle chosen by the driving frequency. Changing the driving frequency changes θ_B and the Bragg condition is not satisfied anymore by the beam. To overcome these limitations the transducer does not implement a plane wave in the crystal but an acoustic beam which features a superposition of plane waves as well. With this, each plane wave component of the optical beam finds a plane wave component of the acoustical beam which together fulfill the Bragg condition. The same trick is used to overcome the problem of different modulation frequencies and deflection angles.
This opens a range of frequencies around a central driving frequency f_c, known as the bandwidth of the AOD, where the Bragg condition is satisfied and consequently an angular range which can be addressed, being the well-known scan angle. The bandwidth B and the scan angle $\Delta\theta$ are connected by

$$\Delta\theta = \frac{\lambda}{v_s} B. \tag{5.1}$$

In Figure 5.1 such an acoustical beam is illustrated.

5.1.3 Shear Mode Configuration

In AODs a large scan angle $\Delta\theta$ is desired and from Equation 5.1 it is evident that this can be achieved by minimizing the speed of sound. Two modes of sound waves are typically used for acousto-optical interactions [99]. One is known as the longitudinal mode and the other as the shear mode. While both modes offer their advantages and find application in acousto-optic applications for the AOD the significantly slower velocity of sound in the shear mode makes it the best choice. A major disadvantage of the shear mode is that it effects the light polarization. By a proper choice of the crystal axis and the polarization direction of the transversal acoustic wave the AOD behaves like a half-wave plate with its optical axis oriented 45° to the acoustic propagation direction, but the input beam polarization is fixed by the geometry.

5.1.4 A Two-Dimensional AOD

To be able to address the full trap plane in the experiment a crossed AOD configuration is used. Two AODs right after each other and perpendicular oriented allow to deflect light in a solid angle given by the product of the individual angular ranges of both AODs. The crossed AOD used in the present experiment is the DTSXY-400-800.860 from AA Opto-electronic. The AODs are already aligned and calibrated to

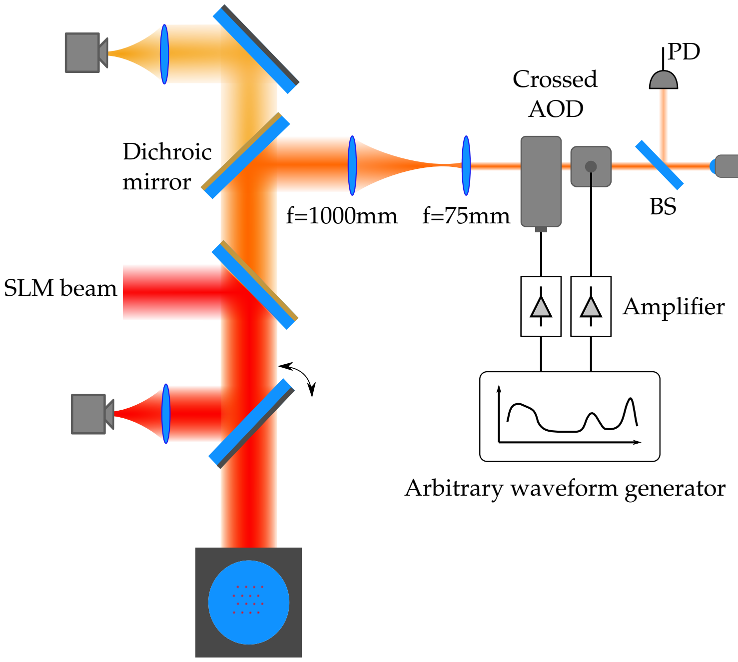

Figure 5.2 – Extension to the setup for the creation of trap arrays with an AOD. The schematic diagram shows the optical setup. The 795 nm beam coming from an optical fiber is sent through a crossed AOD and through a telescope. It is then sampled into the existing path to the objective by a custom coated dichroic mirror. After the fiber collimator a beam sampler (BS) sends about 10% of the light onto a photo diode (PD) which is used for intensity stabilization. to extend the existing setup with an AOD.

each other by the manufacturer. Their properties are listed in Table 5.1. It has an electrical impedance of 50 Ω and is interfaced with an SMA connector on each AOD.

Property	Value
Central drive frequnecy at 795 nm [f_c]	102(4) MHz
Bandwidth [B]	36 MHz
Max optical power density	$5\,\mathrm{W\,mm^{-2}}$
Max RF Power	2 W
Laser Beam Diameter [D]	$500\,\mu\mathrm{m} < D < 6\,\mathrm{mm}$
Material (speed of sound [v_s])	TeO2 ($650\,\mathrm{m\,s^{-1}}$)
Scan angle	$(44\mathrm{mrad}\,)^2$

Table 5.1 – Crossed AOD (AA DTSXY-400-800.860) properties

5.2 Extension to the Apparatus

The setup of the optics to extend the existing beam paths for supporting the movable traps generated by the AOD is shown in Figure 5.2. For this setup a DFB diode from Eagleyard EYP-DFB-0795-00080-1500-BFW01-0005, held in a Thorlabs butter fly diode mount LM14S2, is used as a light source. It provides the setup with up to 80 mW of optical power at a wavelength of 795 nm. This is passed through an acousto-optic modulator for intensity stabilization.

The setup near the experimental chamber starts out with a beam coming from a single mode, polarization maintaining optical fiber. A Schaefter and Kirchhoff fiber collimator 60FC-4-M12-10 is used to attain a $1/e^2$ diameter of 2 mm. The collimator is oriented such that the beam polarization is vertical to the table, matching the requirement of the AOD. A beam sampler after the collimator is placed to direct the light onto a photodiode, used for the intensity stabilization. The majority of the light passing the beam sampler is sent through the crossed AOD introduced before. A telescope with a magnification factor of 15 is used to convert the $1/e^2$ diameter to 30 mm. This diameter is chosen as a compromise between losing power due to the hole in the objective and matching the diffraction limited geometries of the 1064 nm traps with the 795 nm traps. The hole cuts of 44% of the power in this configuration. As there is no possibility to compensate for aberrations with the AOD only a single telescope with a large magnification is used to avoid unneeded optical components in the setup. The telescope is made up by a 1-inch achromatic lens with a focal length of $f = 75\,\mathrm{mm}$ and a 2-inch achromatic lens of $f = 1000\,\mathrm{mm}$ focal length.

The beam will be sampled in into the existing beam path to the objective with a custom coated 3-inch beam sampler between the imaging camera and the beam sampler for the 1064 nm SLM traps.

The crossed AOD is driven by an arbitrary waveform generator, implemented as a PCI express card, from Spectrum Instrumentation, which provides two independent outputs. It has a sampling rate of $1.25\,\mathrm{GS\,s^{-1}}$. This allows to use the AOD directly connected to the arbitrary waveform generator, enabling to directly sample a waveform with multiple frequency components to produce multiple tweezers moving arbitrarily in the two dimensional plane. The arbitrary waveform generator provides up to 14 dBm output power. This is amplified to the 2 W maximal input power of the AOD by an attenuation of -21 dB and a subsequent amplification by 40 dB using an RF Bay MPA-40-40 amplifier for each AOD.

5.2.1 Characterization

The diffraction efficiency of the crossed AOD was measured for the whole frequency and RF power range. The results are shown in Figure 5.3. A peak efficiency of 86% was obtained.

The chosen telescope configuration, introduced in the preceding section, together with the scan angle of the AOD determine the region where the traps can be positioned. This region has a size of $100\,\mu\mathrm{m} \times 100\,\mu\mathrm{m}$. Another important characterizing quantity is the displacement of the trap with the RF frequency. It is found to be

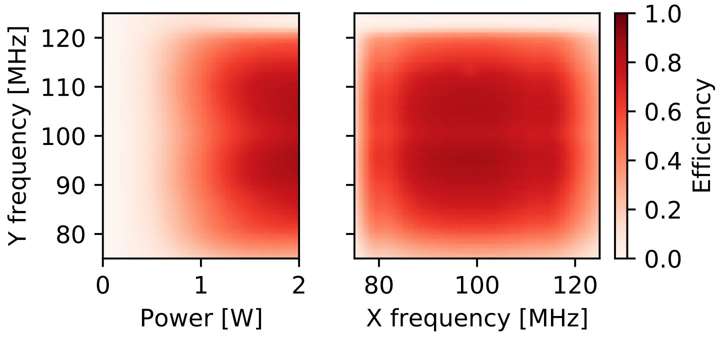

(a) All parameters scanned

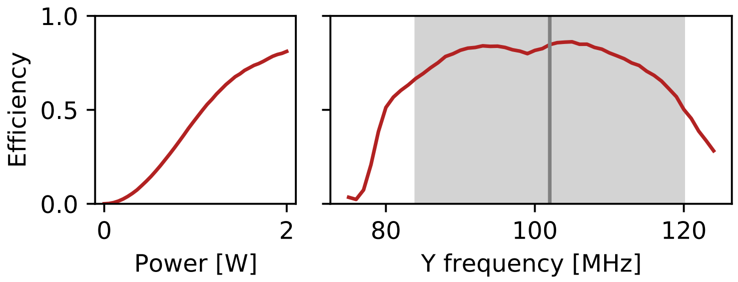

(b) X frequency fixed to 100 MHz

Figure 5.3 – AOD diffraction efficiency measurement. The diffraction efficiency of the AOD, which was measured in the setup as described in the main text is shown. (a) The left panel shows the measured diffraction efficiency for different RF powers. The X frequency was fixed to 100 MHz. The right one shows the efficiency scanned over both axis of the AOD. The RF power was fixed to 2 W. The peak diffraction efficiency was measure to be 86%. (b) The left panel shows the diffraction efficiency with varying power. The frequencies for both axis were 100 MHz. The right panel shows the efficiency for different Y-frequencies. The X-frequency was fixed to 100 MHz. The vertical line (dark gray) indicates the central driving frequency as specified by the manufacturer and the marked region (light gray) illustrates the specified bandwidth.

$2.7\,\mu\mathrm{m\,MHz}^{-1}$. This number is to be compared to the trap frequency and determines the minimal distance between tweezers generated by the AOD. The deflection by the AOD is accompanied by a frequency Doppler shift, as pointed out before, which is exactly the driving frequency. Two closely spaced tweezers overlap slightly and this overlap leads to an interference oscillating with the frequency difference between the light fields of the traps. This oscillation can lead to a strong parametric heating effect when it is close to the trap frequency. Therefore the oscillation needs to be much faster then the trapping frequency and henceforth this limits the tweezers spacing form below. In this setup a minimal spacing of about 2 µm is expected.

5.3 Enabled Improvements

The setup extension introduced in the previous section opens many routes to improve the current experiment. In this section a few concrete applications will be discussed.

5.3.1 Rearranging Atoms Between Traps

As already mentioned in chapter 4, the loading efficiency is a major obstacle to overcome. The AOD enables us to move an atom loaded in one trap into another trap within a few µs [76]. This allows to generate a trap pattern using the SLM which has traps at the positions desired for the experiment to be carried out and additional auxiliary traps around it. After an initial loading of the traps a picture is taken revealing which of the traps is loaded with an atom and which is not. The traps which are needed for the experiment but are not loaded can subsequently be filled by moving an atom from an auxiliary trap into it. As potentially many required traps are not filled this yields an assignment problem which needs to be solved very fast. A typical algorithm to solve this is the Hungarian algorithm. For the relevant problem size, this can be run within a few ms [100].

It needs to be remarked that it is possible to move atoms in a tweezers with an SLM as well, as have been shown in [101]. However, the SLM setup used in the present experiment is not suited for this approach. Approaches for reshuffling atoms, close to the one described, have been implemented in [102]. Similar procedures have been utilized in setups with tweezers exclusively generated by an AOD [97, 103].

5.3.2 Aberration Characterization

Aberrations, as introduced in subsection 3.2.3, are essentially undesired position dependent phase shifts in the Fourier plane. To measure the relative phase between two points of a wave front they need to be brought to interference. This can be done with the aid of an aperture in the Fourier plane which has two holes at the positions to be compared in phase. The light rays passing the holes are brought to interference by placing a lens. The result are interference fringes at the focus of the lens whose positions are determined by the relative light phase between the two holes. By scanning all different positions of the two holes, all the relative phases can be mapped out and

the aberrations can be back calculated. In the present apparatus the aperture in the Fourier plane can be mimicked, using the SLM, by deflecting all except for two spots to hit a beam block. To measure the resulting interference pattern in the experimental chamber an atom trapped in an AOD tweezers can be used as a detector by means of a light shift measurement as done in section 3.6.2. For a total power of 5 W incident on the SLM and mimicked aperture holes of 1 mm diameter a contrast of tens of MHz can be expected in the light shifted D1-line.
A similar method was applied in [104] with a digital mirror device and atoms trapped in an optical lattice.

5.3.3 Optical Addressing

To study the dynamical evolution of a system it is often required that an initial state can be prepared in a reproducible fashion. This can be and has been done by means of magnetic field gradients or apertures or a digital mirror device imaged onto the atomic system. However, a much more versatile approach is to use an addressing beam which can be focussed down to a single atom. With the AOD traps, an AC-stark shift can be applied to shift only a few well-chosen atoms to resonance with globally applied light. This allows to drive only these atoms to a state different from there initial state. This approach has been utilized in [105].

5.3.4 Deterministic Loading

In chapter 4 the light shift in the excited state of the D1-line was identified to spoil the deterministic loading. For 795 nm trapping light the excited state is only shifted by a factor of -0.37 with respect to the trap depth. Therefore the broadening due to the light shift is expected to be significantly less severe and comparable to the sucessfull Rubidium experiments. An experimental sequence to exploit this would involve the loading into tweezers generated by the AOD and a subsequent transfere to the SLM traps.

5.3.5 Eliminating the Talbot-like Effect

The Talbot effect as well as the Talbot-like effect introduced in 3.6.3 base on a fixed phase relation between the traps. In a trap array generated by the AOD each trap has a slightly different frequency due to the Doppler shift. Therefore no time constant and well localized constructive interference between the tweezers outside the trap plane can build up. Hence no trapping outside the plane is expected. This can be used to avoid the observed out of plane trapping for SLM tweezers with the aid of the same experimental sequence described in the preceding section.

5.4 Conclusion and Outlook

To make the full potential of the SLM based tweezers setup available for experiments it will be accompanied by an AOD setup. The working principle of an AOD was discussed in detail and a carefully planned optical system and the surrounding components were presented. The impacts on currently limiting factors of the system was exemplified. The implementation of the AOD setup will be a crucial step to overcome limitations of all kind and ultimately make the quantum many body regime accessible for the apparatus.

CHAPTER 6

Conclusion and Outlook

6.1 Conclusion

This thesis has reported on the planing, construction, characterization and integration of setups related to the generation of freely positionable tweezers for Potassium-39. The theoretical background for trapping atoms by using their dipole moment has been introduced and the found relations where used to estimate the experimental relevant parameters. An overview of the existing experimental apparatus, in which the new tweezers setup is implemented, was provided.

The working principle of a liquid crystal spatial light modulator was discussed and a setup to integrate this into the experiment has been presented. Subsequently the arising phase retrieval problem in the context of diffraction limited spots has been discussed in detail. The so produced arrays of traps were characterized and a loading probability close to the theoretical limit was found. However, the measurements uncovered the presence of inhomogeneities and aberrations in the system. The trapping of atoms outside the desired plane has been observed and identified as the currently limiting factor in the imaging when going to closer spaced tweezers.

The fundamental limit on the loading probability of atoms in the traps was identified as a major obstacle to overcome. To do so, a scheme based on well-tunable blue detuned collisions has been implemented. The results show clear evidence of the success of this technique, but other factors were identified to be limiting.

The extension of the existing apparatus with an AOD based setup to generate movable tweezers has been evaluated and an integration has been planned. This holds the prospect of overcoming several current limitations in the future, enabling new experiments.

6.2 Outlook

The main future application of the setup is to investigate new few- and many-body systems with exotic features. With the parameters reported in this thesis the few-body regime is already accessible and currently under investigation. The limited loading probability currently hinders the setup from exploring many-body physics. Several ideas have been mentioned already to overcome this limitation. With entering the many-body regime a wealth of possibilities opens up and even observables, new to the neutral atom community, will be acquirable , like for instance out-of-time-order correlation functions [106] . Especially the fast cycling times of the experiment, exceeding those of lattice experiments by an order of magnitude, makes new mea-

surements possible. This will allow to directly investigate entanglement spreading and information scrambling [107]. By the freedom in positioning the tweezers new parameters to map out phase diagrams will be accessible. One example is the implementation of a tunable curvature strain potentially yielding landau levels and a emergent supersymmertry [108].
Another setup worth mentioning, which is currently under construction, is a spin selective tweezers setup using the same path as the AOD setup presented here. This will allow to separate spin species from each other. Besides the advantages due to spin selective imaging this will also enable another way of actively introducing entanglement in the system.

APPENDIX A

Measurements on all Individual Traps

This appendix contains all the measurements done on the atoms for characterizing the traps and the deterministic loading procedure. All measurements were done with the same phase pattern on the SLM pattern and under the same experimental conditions. In Figure A.1, Figure A.2, and Figure A.3 the lightshifts, parametric heating, and termometry measurements of all traps in a 5×5 array are shown. The measurements were done as described in the main text.

Figure A.4 shows the individual results of the deterministic loading for all the traps. The measurement procedure is as well described in the main text.

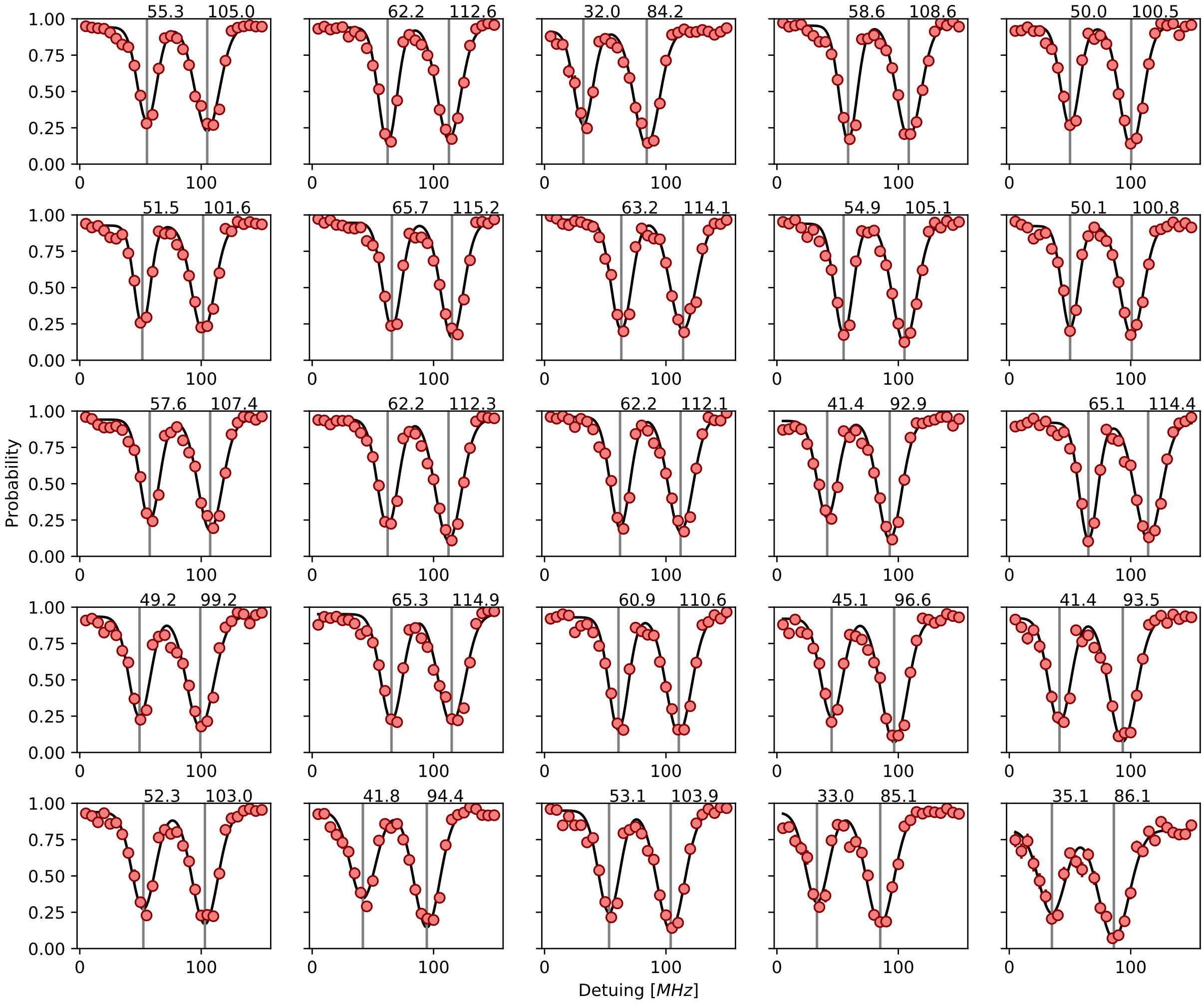

Figure A.1 – Light shift measurements of all traps. Each graph shows the measurement on a single trap on a 5 × 5 tweezers array. See Figure 2.2 for how to read these plots.

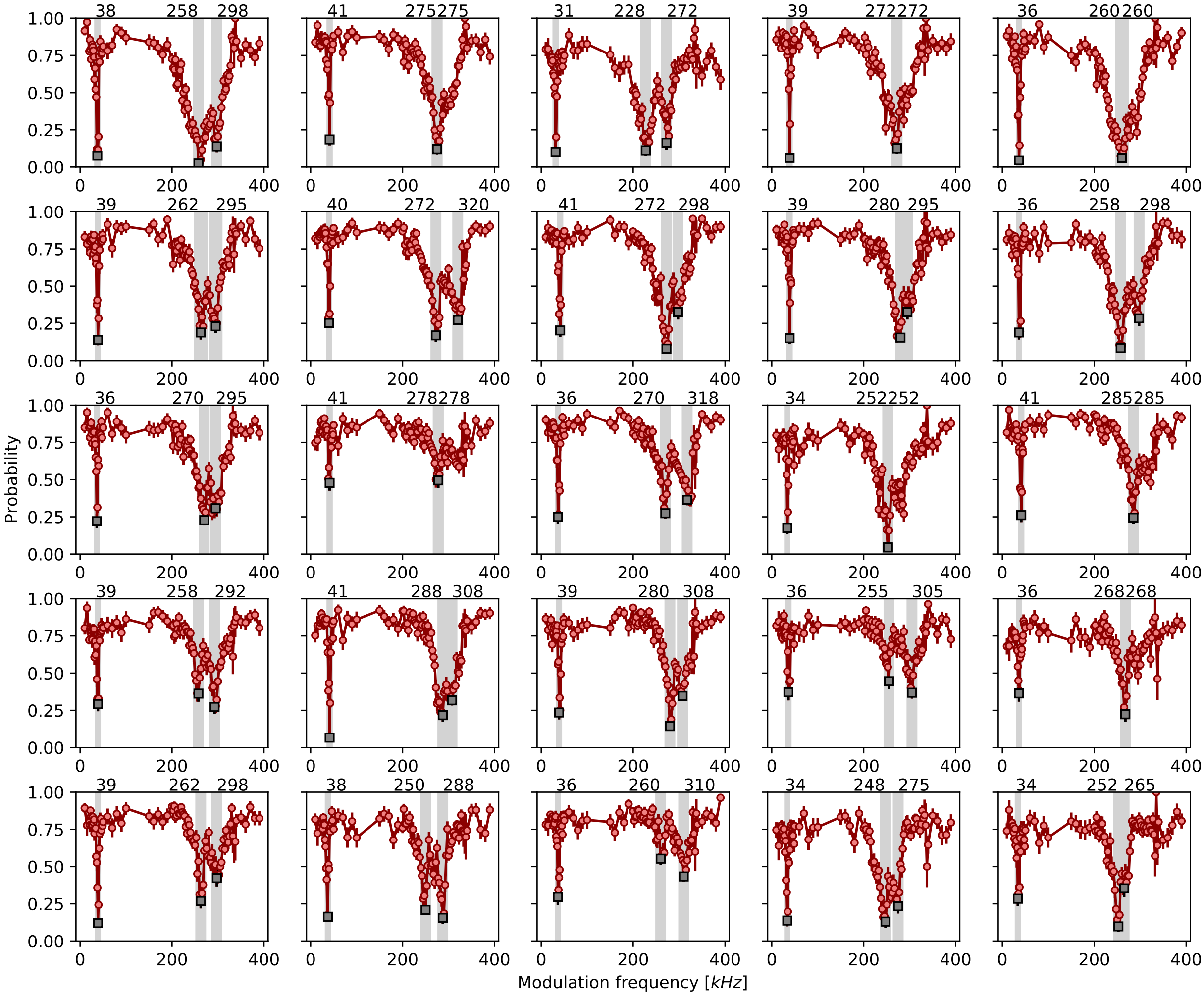

Figure A.2 – Parametric heating measurements of all traps. Each graph shows the measurement on a single trap on a 5 × 5 tweezers array. See Figure 3.13 for how to read these plots.

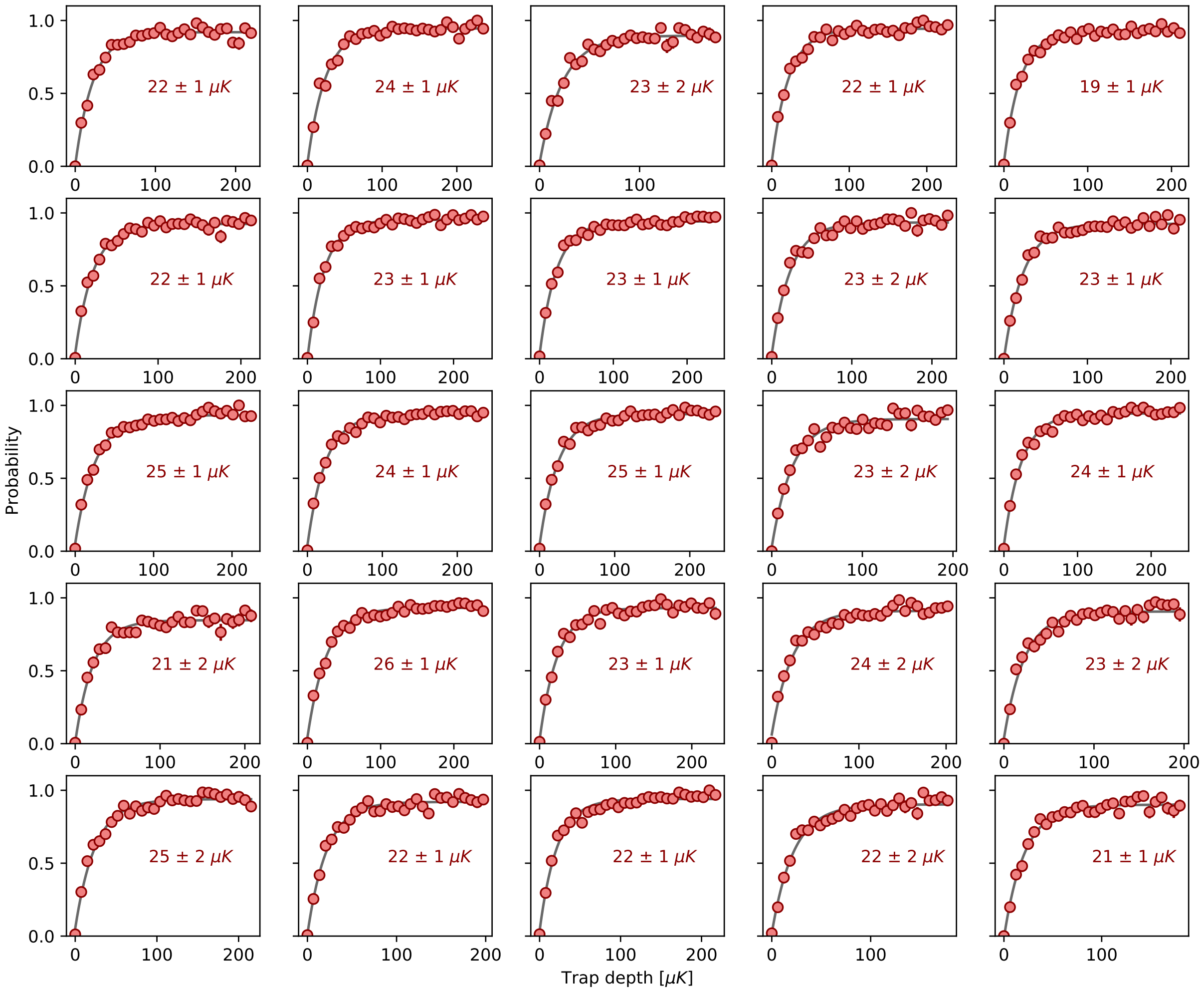

Figure A.3 – In-situ temperature measurements of all traps. Each graph shows the measurement on a single trap on a 5×5 tweezers array. See Figure 3.14 for how to read these plots.

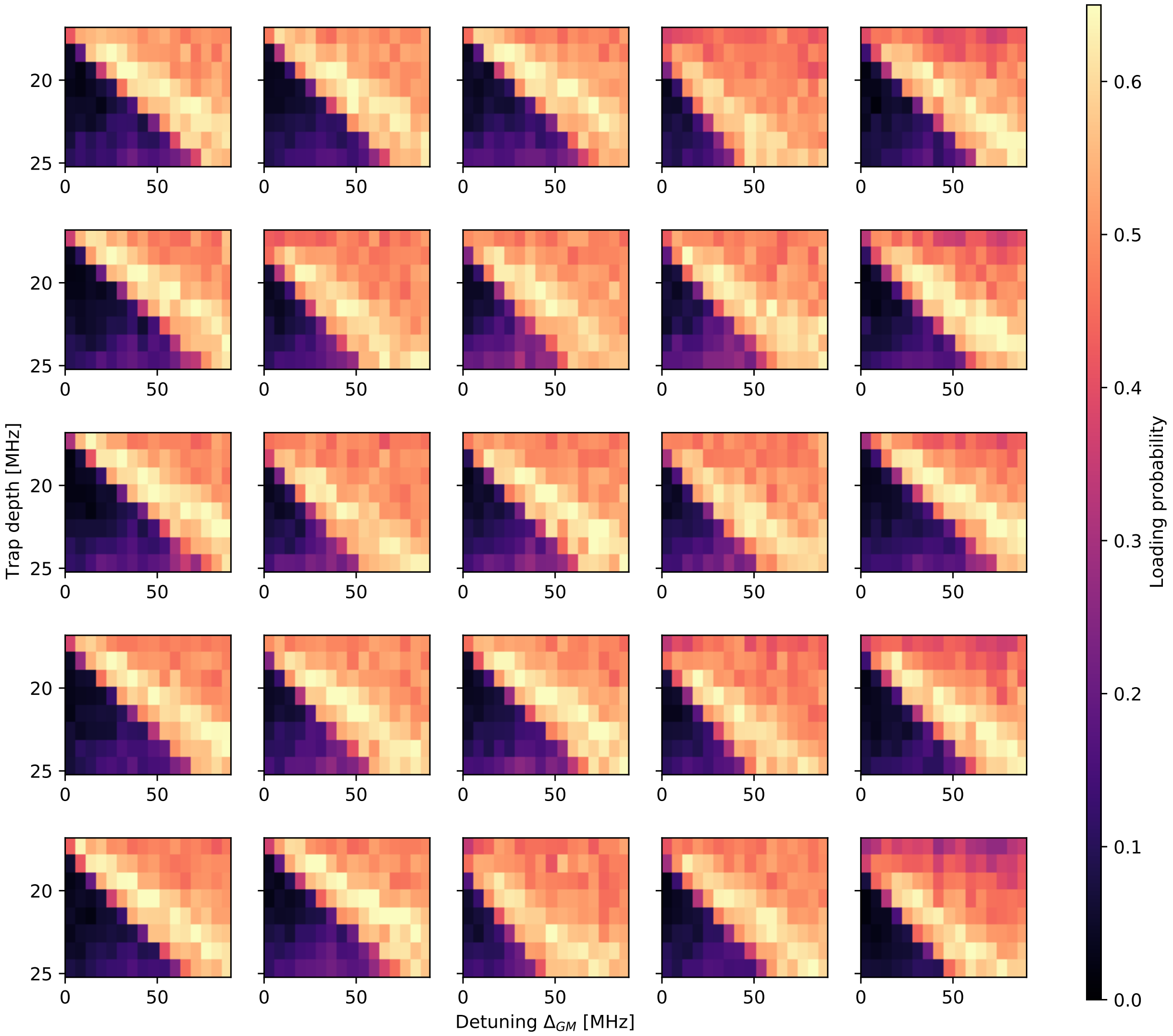

Figure A.4 – Deterministic loading measurement of all traps. Each panel shows the result of the deterministic loading measurement introduced in the main text. For a description of what is shown see Figure 4.4.

Bibliography

1. Schrödinger, E. ARE THERE QUANTUM JUMPS ?: PART II *. *The British Journal for the Philosophy of Science* **III,** 233–242 (1952) (cit. on p. 1).
2. Freedman, S. J. & Clauser, J. F. Experimental Test of Local Hidden-Variable Theories. *Physical Review Letters* **28,** 938–941 (1972) (cit. on p. 1).
3. Hong, C. K., Ou, Z. Y. & Mandel, L. Measurement of subpicosecond time intervals between two photons by interference. *Physical Review Letters* **59,** 2044–2046 (1987) (cit. on p. 1).
4. Boschi, D., Branca, S., De Martini, F., Hardy, L. & Popescu, S. Experimental Realization of Teleporting an Unknown Pure Quantum State via Dual Classical and Einstein-Podolsky-Rosen Channels. *Physical Review Letters* **80,** 1121–1125 (1998) (cit. on p. 1).
5. Anderson, M. H., Ensher, J. R., Matthews, M. R., Wieman, C. E. & Cornell, E. A. Observation of Bose-Einstein Condensation in a Dilute Atomic Vapor. *Science* **269,** 198–201 (1995) (cit. on p. 1).
6. Davis, K. B. *et al.* Bose-Einstein Condensation in a Gas of Sodium Atoms. *Physical Review Letters* **75,** 3969–3973 (1995) (cit. on p. 1).
7. Greiner, M., Mandel, O. & Esslinger, T. Quantum phase transition from a superfluid to a Mott insulator in a gas of ultracold atoms. *Nature* **415,** 39–44 (2002) (cit. on p. 1).
8. Altman, E. *et al.* Quantum Simulators: Architectures and Opportunities. *arXiv: 1912.06938* (2019) (cit. on p. 1).
9. Chomaz, L. & van Bijnen R.M.W., P. D. Observation of roton mode population in a dipolar quantum gas. *Nature Phys* **14,** 442 –446 (2018) (cit. on p. 1).
10. Cheneau, M. *et al.* Light-cone-like spreading of correlations in a quantum many-body system. *Nature* **481,** 484–487 (2012) (cit. on p. 1).
11. Aidelsburger, M. *et al.* Experimental Realization of Strong Effective Magnetic Fields in an Optical Lattice. *Phys. Rev. Lett.* **107,** 255301 (2011) (cit. on p. 1).
12. Jamadi, O. *et al.* Direct observation of photonic Landau levels and helical edge states in strained honeycomb lattices. *arXiv:2001.10395* (2020) (cit. on p. 1).
13. Feynman, R. P. Simulating physics with computers. *Int J Theor Phys* **21,** 467–488 (1982) (cit. on p. 1).
14. Georgescu, I. M., Ashhab, S. & Nori, F. Quantum Simulation. *Reviews of Modern Physics* **86,** 153–185 (2014) (cit. on p. 1).

15. Moll, N. *et al.* Quantum optimization using variational algorithms on near-term quantum devices. *Quantum Science and Technology* **3,** 030503 (2018) (cit. on p. 2).
16. Kaubruegger, R. *et al.* Variational spin-squeezing algorithms on programmable quantum sensors. *Physical Review Letters* **123,** 260505 (2019) (cit. on p. 2).
17. Saffman, M., Walker, T. G. & Mølmer, K. Quantum information with Rydberg atoms. *Reviews of Modern Physics* **82,** 2313–2363 (2010) (cit. on p. 2).
18. Gross, C. & Bloch, I. Quantum simulations with ultracold atoms in optical lattices. *Science* **357,** 995–1001 (2017) (cit. on p. 2).
19. Mourachko, I. *et al.* Many-Body Effects in a Frozen Rydberg Gas. *Physical Review Letters* **80,** 253–256 (1998) (cit. on p. 2).
20. Santos, L., Shlyapnikov, G. V., Zoller, P. & Lewenstein, M. Bose-Einstein Condensation in Trapped Dipolar Gases. *Physical Review Letters* **85,** 1791–1794 (2000) (cit. on p. 2).
21. Jau, Y.-Y., Hankin, A. M., Keating, T., Deutsch, I. H. & Biedermann, G. W. Entangling atomic spins with a Rydberg-dressed spin-flip blockade. *Nature Physics* **12,** 71–74 (2016) (cit. on p. 2).
22. Pupillo, G., Micheli, A., Boninsegni, M., Lesanovsky, I. & Zoller, P. Strongly Correlated Gases of Rydberg-Dressed Atoms: Quantum and Classical Dynamics. *Physical Review Letters* **104,** 223002 (2010) (cit. on p. 2).
23. Zeiher, J. *Realization of Rydberg-dressed quantum magnets* PhD thesis (2017) (cit. on pp. 2, 54).
24. Glaetzle, A. W. *et al.* Designing Frustrated Quantum Magnets with Laser-Dressed Rydberg Atoms. *Phys. Rev. Lett.* **114,** 173002 (2015) (cit. on p. 2).
25. Schauss, P. *et al.* Crystallization in Ising quantum magnets. *Science* **347,** 1455–1458 (2015) (cit. on p. 2).
26. Bijnen, R. M.W. v. *et al.* Patterned Rydberg excitation and ionization with a spatial light modulator. *New Journal of Physics* **17,** 023045 (2015) (cit. on p. 2).
27. Levine, H. *et al.* High-Fidelity Control and Entanglement of Rydberg-Atom Qubits. *Phys. Rev. Lett.* **121,** 123603 (2018) (cit. on p. 2).
28. Nogrette, F. *et al.* Single-Atom Trapping in Holographic 2D Arrays of Microtraps with Arbitrary Geometries. *Phys. Rev. X* **4,** 021034 (2014) (cit. on p. 2).
29. Barredo, D., Lienhard, V., de Léséleuc, S., Lahaye, T. & Browaeys, A. Synthetic three-dimensional atomic structures assembled atom by atom. *Nature* **561,** 79–82 (2018) (cit. on p. 2).
30. Omran, A. *et al.* Generation and manipulation of Schrödinger cat states in Rydberg atom arrays. *Science* **365,** 570–574 (2019) (cit. on p. 2).
31. Lienhard, V. *et al.* Realization of a density-dependent Peierls phase in a synthetic, spin-orbit coupled Rydberg system. *Physical Review X* **10,** 021031 (2020) (cit. on p. 2).

32. Weber, S. *et al.* Topologically protected edge states in small Rydberg systems. *Quantum Science and Technology* **3,** 044001 (2018) (cit. on p. 2).
33. Steck, D. A. Quantum and Atom Optics. eprint: `http://steck.us/teaching` (revision 0.12.6, 23 April 2019) (cit. on p. 5).
34. Doetsch, G. *Introduction to the Theory and Application of the Laplace Transformation* (1974) (cit. on p. 6).
35. Grimm, R., Weidemüller, M. & Ovchinnikov, Y. B. Optical dipole traps for neutral atoms. *arXiv:physics/9902072* (1999) (cit. on p. 6).
36. Agarwal, G. S. *Quantum Optics* (Cambridge University Press, 2012) (cit. on p. 7).
37. Deutsch, I. H. & Jessen, P. S. Quantum-state control in optical lattices. *Physical Review A* **57,** 1972–1986 (1998) (cit. on p. 7).
38. Kaufman, A. *Laser cooling atoms to indistinguishability: Atomic Hong-Ou-Mandel interference and entanglement through spin exchange* PhD thesis (2009) (cit. on p. 7).
39. Thompson, J. D., Tiecke, T. G., Zibrov, A. S. & Lukin, M. D. Coherence and Raman Sideband Cooling of a Single Atom in an Optical Tweezer. *Phys. Rev. Lett.* **110,** 133001 (2013) (cit. on p. 7).
40. curtis.suplee@nist.gov. *Atomic Spectra Database* NIST. Last Modified: 2019-12-11T10:03-05:00 Library Catalog: www.nist.gov. `https://www.nist.gov/pml/atomic-spectra-database` (2020) (cit. on p. 8).
41. Weber, S. *et al.* Calculation of Rydberg interaction potentials. *Journal of Physics B: Atomic, Molecular and Optical Physics* **50,** 133001 (2017) (cit. on pp. 8, 45).
42. Saleh, B. & Teich, M. *Fundamentals of Photonics* (John Wiley Sons, Ltd, 2001) (cit. on pp. 8, 57).
43. Metcalf, H. J. & Van der Straten, P. *Laser cooling and trapping* (Springer, New York, 1999) (cit. on p. 8).
44. Chuu, C.-S. & Zhang, C. Suppression of phase decoherence in a single atomic qubit. *Phys. Rev. A* **80,** 032307 (2009) (cit. on p. 9).
45. Gehm, M. E., O'Hara, K. M., Savard, T. A. & Thomas, J. E. Dynamics of noise-induced heating in atom traps. *Physical Review A* **58,** 3914–3921 (1998) (cit. on pp. 9, 37).
46. Savard, T. A., O'Hara, K. M. & Thomas, J. E. Laser-noise-induced heating in far-off resonance optical traps. *Phys. Rev. A* **56,** R1095–R1098 (1997) (cit. on pp. 9, 37).
47. Tiecke, T. *Feshbach resonances in ultracold mixtures of the fermionic quantum gases 6Li and 40K* PhD thesis (2009) (cit. on p. 10).
48. Gallagher, T. F. *Rydberg Atoms* (Cambridge University Press, 1994) (cit. on p. 10).
49. Duda, M. *A Laser System for Cooling and Trapping Potassium-39* mastersthesis (2017) (cit. on p. 13).
50. Lorenz, N. to be published. PhD thesis (2020) (cit. on p. 13).

51. Festa, L. to be published. PhD thesis (2021) (cit. on p. 13).
52. Schlosser, M., Tichelmann, S., Kruse, J. & Birkl, G. Scalable architecture for quantum information processing with atoms in optical micro-structures. *Quantum Information Processing* **10,** 907–924 (2011) (cit. on p. 15).
53. Norcia, M. A., Young, A. W. & Kaufman, A. M. Microscopic Control and Detection of Ultracold Strontium in Optical-Tweezer Arrays. *Phys. Rev. X* **8,** 041054 (2018) (cit. on p. 15).
54. Stuart, D. & Kuhn, A. Single-atom trapping and transport in DMD-controlled optical tweezers. *New Journal of Physics* **20,** 023013 (2018) (cit. on p. 15).
55. Labuhn, H. *Rydberg excitation dynamics and correlations in arbitrary 2D arrays of single atoms* PhD thesis (Université Paris-Saclay, Feb. 26, 2016) (cit. on pp. 15, 33).
56. Frumker, E. & Silberberg, Y. Femtosecond pulse shaping using a two-dimensional liquid-crystal spatial light modulator. *Optics Letters* **32,** 1384 (2007) (cit. on p. 15).
57. Grier, D. G. A revolution in optical manipulation. *Nature* **424,** 810–816 (2003) (cit. on p. 15).
58. Bozinovic, N. *et al.* Terabit-Scale Orbital Angular Momentum Mode Division Multiplexing in Fibers. *Science* **340,** 1545–1548 (2013) (cit. on p. 15).
59. Liu, R. *et al.* Multi-plane Imaging of Neural Activity From the Mammalian Brain Using a Fast-switching Liquid Crystal Spatial Light Modulator. *bioRxiv* (2018) (cit. on p. 15).
60. Xu, Z. *et al.* Visible light high-resolution imaging system for large aperture telescope by liquid crystal adaptive optics with phase diversity technique. *Scientific Reports* **7,** 10034 (2017) (cit. on p. 15).
61. Boyer, V. *et al.* Dynamic manipulation of Bose-Einstein condensates with a spatial light modulator. *Phys. Rev. A* **73,** 031402 (2006) (cit. on p. 15).
62. Becker, C. *et al.* Oscillations and interactions of dark and dark-bright solitons in Bose-Einstein condensates. *Nature Physics* **4,** 496–501 (2008) (cit. on p. 15).
63. Farré, A. *et al.* Positional stability of holographic optical traps. *Optics Express* **19,** 21370 (2011) (cit. on p. 16).
64. Zhang, Z., You, Z. & Chu, D. Fundamentals of phase-only liquid crystal on silicon (LCOS) devices. *Light: Science & Applications* **3,** e213–e213 (2014) (cit. on p. 16).
65. Jesacher, A. *et al.* Wavefront correction of spatial light modulators using an optical vortex image. *Optics Express* **15,** 5801 (2007) (cit. on p. 20).
66. Gerchberg, R. W. & Saxton, W. O. A Practical Algorithm for the Determination of Phase from Image and Diffraction Plane Pictures. **35,** 6 (1972) (cit. on p. 21).
67. Cooley, J. W. & Tukey, J. W. An Algorithm for the Machine Calculation of Complex Fourier Series. *Math. Comput.* **19,** 297–301 (1965) (cit. on p. 25).

68. Gaunt, A. L. & Hadzibabic, Z. Robust Digital Holography For Ultracold Atom Trapping. *Scientific Reports* **2** (2012) (cit. on pp. 25, 27).
69. Bijnen, R. R. V. *Quantum engineering with ultracold atoms* Publisher: Technische Universiteit Eindhoven. PhD thesis (2013) (cit. on p. 25).
70. Pasienski, M. & DeMarco, B. A high-accuracy algorithm for designing arbitrary holographic atom traps. *Optics Express* **16,** 2176 (2008) (cit. on p. 27).
71. Di Leonardo, R., Ianni, F. & Ruocco, G. Computer generation of optimal holograms for optical trap arrays. *Optics Express* **15,** 1913 (2007) (cit. on p. 27).
72. Kim, D. *et al.* Large-Scale Uniform Optical Focus Array Generation with a Phase Spatial Light Modulator. *Optics Letters* **44,** 3178 (2019) (cit. on p. 28).
73. Matsumoto, N. *et al.* High-quality generation of a multispot pattern using a spatial light modulator with adaptive feedback. *Optics Letters* **37,** 3135 (2012) (cit. on p. 28).
74. Wang, Y. *et al.* Preparation of hundreds of microscopic atomic ensembles in optical tweezer arrays. *arXiv:1912.04200 [cond-mat, physics:physics, physics:quant-ph].* arXiv: `1912.04200` (2019) (cit. on p. 33).
75. Hutzler, N. R., Liu, L. R., Yu, Y. & Ni, K.-K. Eliminating light shifts for single atom trapping. *New Journal of Physics* **19,** 023007 (2017) (cit. on p. 33).
76. Leseleuc de kerouara, S. d. *Quantum simulation of spin models with assembled arrays of Rydberg atoms* These de doctorat (Université Paris-Saclay, 2018) (cit. on pp. 37, 63).
77. Landini. *A tunable Bose-Einstein condensate for quantum interferometry* PhD thesis (2011) (cit. on p. 41).
78. Rayleigh, L. XXV. *On copying diffraction-gratings, and on some phenomena connected therewith. The London, Edinburgh, and Dublin Philosophical Magazine and Journal of Science* **11,** 196–205 (1881) (cit. on p. 41).
79. Zhong, H., Zhang, Y., Belic, M. R. & Zhang, Y. Generating Lieb and superhoneycomb lattices by employing the fractional Talbot effect. *Journal of the Optical Society of America B* **36,** 862 (2019) (cit. on p. 41).
80. Schlosser, M. *et al.* Large-scale multilayer architecture of single-atom arrays with individual addressability. *arXiv:1902.05424* (2019) (cit. on p. 41).
81. Goodman, J. W. *Introduction to Fourier Optics* (Roberts and Company Publishers, 2005) (cit. on p. 41).
82. Carpentier, A. V. *et al.* Preparation of a single atom in an optical microtrap. *Laser Physics Letters* **10,** 125501 (2013) (cit. on p. 45).
83. Fung, Y. H. & Andersen, M. F. Efficient collisional blockade loading of a single atom into a tight microtrap. *New Journal of Physics* **17,** 073011 (2015) (cit. on pp. 45, 54).
84. Lester, B. J., Luick, N., Kaufman, A. M., Reynolds, C. M. & Regal, C. A. Rapid Production of Uniformly Filled Arrays of Neutral Atoms. *Phys. Rev. Lett.* **115,** 073003 (2015) (cit. on p. 45).

85. Derevianko, A., Johnson, W. R., Safronova, M. S. & Babb, J. F. High-Precision Calculations of Dispersion Coefficients, Static Dipole Polarizabilities, and Atom-Wall Interaction Constants for Alkali-Metal Atoms. *Physical Review Letters* **82,** 3589–3592 (1999) (cit. on p. 46).

86. Casimir, H. B. G. & Polder, D. The Influence of Retardation on the London-van der Waals Forces. *Physical Review* **73,** 360–372 (1948) (cit. on p. 46).

87. Jaffe, R. L. The Casimir Effect and the Quantum Vacuum. *Physical Review D* **72,** 021301 (2005) (cit. on p. 46).

88. Jones, K. M., Tiesinga, E., Lett, P. D. & Julienne, P. S. Ultracold photoassociation spectroscopy: Long-range molecules and atomic scattering. *Reviews of Modern Physics* **78,** 483–535 (2006) (cit. on p. 46).

89. Weiner, J., Bagnato, V. S., Zilio, S. & Julienne, P. S. Experiments and theory in cold and ultracold collisions. *Reviews of Modern Physics* **71,** 1–85 (1999) (cit. on pp. 47, 49).

90. Wang, H., Gould, P. L. & Stwalley, W. C. Long-range interaction of the ^{39} K *(4s)*+ ^{39} K *(4p)* asymptote by photoassociative spectroscopy. I. The 0gâĹŠ pure long-range state and the long-range potential constants. *The Journal of Chemical Physics* **106,** 7899–7912 (May 15, 1997) (cit. on p. 47).

91. Falke, S. *et al.* Potassium ground-state scattering parameters and Born-Oppenheimer potentials from molecular spectroscopy. *Physical Review A* **78** (2008) (cit. on p. 47).

92. Sesko, D., Walker, T., Monroe, C., Gallagher, A. & Wieman, C. Collisional losses from a light-force atom trap. *Physical Review Letters* **63,** 961–964 (1989) (cit. on p. 48).

93. Julienne, P. Cold binary atomic collisions in a light field. *Journal of Research of the National Institute of Standards and Technology* **101,** 487 (1996) (cit. on p. 48).

94. Bali, S, Hoffmann, D & Walker, T. Novel Intensity Dependence of Ultracold Collisions Involving Repulsive States. *Europhysics Letters (EPL)* **27,** 273–277 (1994) (cit. on p. 49).

95. Suominen, K.-A., Holland, M. J., Burnett, K. & Julienne, P. Optical shielding of cold collisions. *Physical Review A* **51,** 1446–1457 (1995) (cit. on p. 51).

96. Fung, Y., Carpentier, A., Sompet, P. & Andersen, M. Two-Atom Collisions and the Loading of Atoms in Microtraps. *Entropy* **16,** 582–606 (2014) (cit. on p. 51).

97. Brown, M. O., Thiele, T., Kiehl, C., Hsu, T.-W. & Regal, C. A. Gray-Molasses Optical-Tweezer Loading: Controlling Collisions for Scaling Atom-Array Assembly. *Phys. Rev. X* **9,** 011057 (2019) (cit. on pp. 51, 63).

98. Ebert, M. *et al.* Atomic Fock State Preparation Using Rydberg Blockade. *Phys. Rev. Lett.* **112,** 043602 (2014) (cit. on p. 55).

99. Chang, C.-H., Heilmann, R. K., Schattenburg, M. L. & Glenn, P. Design of a double-pass shear mode acousto-optic modulator. *Review of Scientific Instruments* **79,** 033104 (2008) (cit. on p. 59).

100. Yadav, S. S., Lopes, P. A. C., Ilic, A. & Patra, S. K. Hungarian algorithm for subcarrier assignment problem using GPU and CUDA. *International Journal of Communication Systems* **32,** e3884 (2019) (cit. on p. 63).
101. Kim, H., Kim, M., Lee, W. & Ahn, J. Gerchberg-Saxton algorithm for fast and efficient atom rearrangement in optical tweezer traps. *Optics Express* **27,** 2184 (2019) (cit. on p. 63).
102. Barredo, D., de Léséleuc, S., Lienhard, V., Lahaye, T. & Browaeys, A. An atom-by-atom assembler of defect-free arbitrary two-dimensional atomic arrays. *Science* **354,** 1021–1023 (2016) (cit. on p. 63).
103. Endres, M. *et al.* Atom-by-atom assembly of defect-free one-dimensional cold atom arrays. *Science* **354,** 1024–1027 (2016) (cit. on p. 63).
104. Zupancic, P. *et al.* Ultra-precise holographic beam shaping for microscopic quantum control. *Optics Express* **24,** 13881 (2016) (cit. on p. 64).
105. Labuhn, H. *et al.* Single-atom addressing in microtraps for quantum-state engineering using Rydberg atoms. *Phys. Rev. A* **90,** 023415 (2014) (cit. on p. 64).
106. Swingle, B., Bentsen, G., Schleier-Smith, M. & Hayden, P. Measuring the scrambling of quantum information. *Physical Review A* **94,** 040302 (2016) (cit. on p. 67).
107. Yao, N. Y. *et al.* Interferometric Approach to Probing Fast Scrambling. *arXiv:1607.01801* (2016) (cit. on p. 68).
108. Nayga, M. M., Rachel, S. & Vojta, M. Magnon Landau levels and emergent supersymmetry in strained antiferromagnets. *Physical Review Letters* **123,** 207204 (2019) (cit. on p. 68).

List of Figures

List of Tables

Acknowledgements

Thanks to this thesis project I had the pleasure to spent another year at the Max-Planck-Institut of Quantum Optics. I had a great time, learned so many great things and met great and inspiring people. For this I want to thank

- Immanuel Bloch not only for taking the formal supervision of this thesis, but especially for his fantastic lectures which were all worth attending more then one time and for spreading his enthusiasm for quantum physics.
- Christian Groß for supervising my project, for supporting me from my first day at MPQ, for sharing his incredible knowledge and for offering me a PhD position in the Rydberg tweezers project. It is a joy and an honor to work with him.
- Lorenzo Festa for always taking time to help and advise me and sharing his experience. It was great fun to work with him on many projects.
- Nikolaus Lorenz for sharing his insights and for many enlightening discussions and of course for the great Wednesday morning boulder sessions.
- Lea Steinert for her support. I am excited to share some more years with her in the lab doing great science and I feel very lucky, as she has a great overview over the apparatus and all its details.
- Robin Eberhard for being the best labmate during the Corona-virus crisis and bringing some great technical know-how into the team.
- For proofreading and giving very helpful advice for my thesis I would like to thank Christian Gross, Lorenzo Festa, Lea Steinert and Nikolaus Lorenz.
- And of course the whole Bloch group for another fantastic year.

Finally I want to thank the three best siblings in the world and my always loving and supportive parents.

Erklärung

Hiermit erkläre ich, die vorliegende Arbeit selbständig verfasst zu haben und keine anderen als die in der Arbeit angegebenen Quellen und Hilfsmittel benutzt zu haben.

Ort, Datum

Unterschrift